DESY 14-089 ISSN 0418-9833
June 2014

Measurement of Multijet Production in *ep* Collisions at High Q^2 and Determination of the Strong Coupling α_s

H1 Collaboration

Abstract

Inclusive jet, dijet and trijet differential cross sections are measured in neutral current deep-inelastic scattering for exchanged boson virtualities $150 < Q^2 < 15\,000\,\mathrm{GeV}^2$ using the H1 detector at HERA. The data were taken in the years 2003 to 2007 and correspond to an integrated luminosity of 351 pb^{-1}. Double differential Jet cross sections are obtained using a regularised unfolding procedure. They are presented as a function of Q^2 and the transverse momentum of the jet, $P_{\mathrm{T}}^{\mathrm{jet}}$, and as a function of Q^2 and the proton's longitudinal momentum fraction, ξ, carried by the parton participating in the hard interaction. In addition normalised double differential jet cross sections are measured as the ratio of the jet cross sections to the inclusive neutral current cross sections in the respective Q^2 bins of the jet measurements. Compared to earlier work, the measurements benefit from an improved reconstruction and calibration of the hadronic final state. The cross sections are compared to perturbative QCD calculations in next-to-leading order and are used to determine the running coupling and the value of the strong coupling constant as $\alpha_s(M_Z) = 0.1165\ (8)_{\mathrm{exp}}\ (38)_{\mathrm{pdf,theo}}$.

To be submitted to *Eur. Phys. J.* **C**

V. Andreev[21], A. Baghdasaryan[33], K. Begzsuren[30], A. Belousov[21], P. Belov[10], V. Boudry[24], G. Brandt[45], M. Brinkmann[10], V. Brisson[23], D. Britzger[10], A. Buniatyan[2], A. Bylinkin[20,42], L. Bystritskaya[20], A.J. Campbell[10], K.B. Cantun Avila[19], F. Ceccopieri[3], K. Cerny[27], V. Chekelian[22], J.G. Contreras[19], J.B. Dainton[16], K. Daum[32,37], C. Diaconu[18], M. Dobre[4], V. Dodonov[10], A. Dossanov[11,22], G. Eckerlin[10], S. Egli[31], E. Elsen[10], L. Favart[3], A. Fedotov[20], J. Feltesse[9], J. Ferencei[14], M. Fleischer[10], A. Fomenko[21], E. Gabathuler[16], J. Gayler[10], S. Ghazaryan[10], A. Glazov[10], L. Goerlich[6], N. Gogitidze[21], M. Gouzevitch[10,38], C. Grab[35], A. Grebenyuk[3], T. Greenshaw[16], G. Grindhammer[22], D. Haidt[10], R.C.W. Henderson[15], M. Herbst[13], J. Hladký[26], D. Hoffmann[18], R. Horisberger[31], T. Hreus[3], F. Huber[12], M. Jacquet[23], X. Janssen[3], H. Jung[10,3], M. Kapichine[8], C. Kiesling[22], M. Klein[16], C. Kleinwort[10], R. Kogler[11], P. Kostka[16], J. Kretzschmar[16], K. Krüger[10], M.P.J. Landon[17], W. Lange[34], P. Laycock[16], A. Lebedev[21], S. Levonian[10], K. Lipka[10,41], B. List[10], J. List[10], B. Lobodzinski[10], E. Malinovski[21], H.-U. Martyn[1], S.J. Maxfield[16], A. Mehta[16], A.B. Meyer[10], H. Meyer[32], J. Meyer[10], S. Mikocki[6], A. Morozov[8], K. Müller[36], Th. Naumann[34], P.R. Newman[2], C. Niebuhr[10], G. Nowak[6], J.E. Olsson[10], D. Ozerov[10], P. Pahl[10], C. Pascaud[23], G.D. Patel[16], E. Perez[9,39], A. Petrukhin[10], I. Picuric[25], H. Pirumov[10], D. Pitzl[10], R. Plačakytė[10,41], B. Pokorny[27], R. Polifka[27,43], V. Radescu[10,41], N. Raicevic[25], T. Ravdandorj[30], P. Reimer[26], E. Rizvi[17], P. Robmann[36], R. Roosen[3], A. Rostovtsev[20], M. Rotaru[4], S. Rusakov[21], D. Šálek[27], D.P.C. Sankey[5], M. Sauter[12], E. Sauvan[18,44], S. Schmitt[10], L. Schoeffel[9], A. Schöning[12], H.-C. Schultz-Coulon[13], F. Sefkow[10], S. Shushkevich[10], Y. Soloviev[10,21], P. Sopicki[6], D. South[10], V. Spaskov[8], A. Specka[24], M. Steder[10], B. Stella[28], U. Straumann[36], T. Sykora[3,27], P.D. Thompson[2], D. Traynor[17], P. Truöl[36], I. Tsakov[29], B. Tseepeldorj[30,40], J. Turnau[6], A. Valkárová[27], C. Vallée[18], P. Van Mechelen[3], Y. Vazdik[21], D. Wegener[7], E. Wünsch[10], J. Žáček[27], Z. Zhang[23], R. Žlebčík[27], H. Zohrabyan[33], and F. Zomer[23]

[1] *I. Physikalisches Institut der RWTH, Aachen, Germany*
[2] *School of Physics and Astronomy, University of Birmingham, Birmingham, UK*[b]
[3] *Inter-University Institute for High Energies ULB-VUB, Brussels and Universiteit Antwerpen, Antwerpen, Belgium*[c]
[4] *National Institute for Physics and Nuclear Engineering (NIPNE) , Bucharest, Romania*[j]
[5] *STFC, Rutherford Appleton Laboratory, Didcot, Oxfordshire, UK*[b]
[6] *Institute for Nuclear Physics, Cracow, Poland*[d]
[7] *Institut für Physik, TU Dortmund, Dortmund, Germany*[a]
[8] *Joint Institute for Nuclear Research, Dubna, Russia*
[9] *CEA, DSM/Irfu, CE-Saclay, Gif-sur-Yvette, France*
[10] *DESY, Hamburg, Germany*
[11] *Institut für Experimentalphysik, Universität Hamburg, Hamburg, Germany*[a]
[12] *Physikalisches Institut, Universität Heidelberg, Heidelberg, Germany*[a]
[13] *Kirchhoff-Institut für Physik, Universität Heidelberg, Heidelberg, Germany*[a]
[14] *Institute of Experimental Physics, Slovak Academy of Sciences, Košice, Slovak Republic*[e]
[15] *Department of Physics, University of Lancaster, Lancaster, UK*[b]
[16] *Department of Physics, University of Liverpool, Liverpool, UK*[b]
[17] *School of Physics and Astronomy, Queen Mary, University of London, London, UK*[b]
[18] *CPPM, Aix-Marseille Univ, CNRS/IN2P3, 13288 Marseille, France*
[19] *Departamento de Fisica Aplicada, CINVESTAV, Mérida, Yucatán, México*[h]
[20] *Institute for Theoretical and Experimental Physics, Moscow, Russia*[i]

[21] *Lebedev Physical Institute, Moscow, Russia*
[22] *Max-Planck-Institut für Physik, München, Germany*
[23] *LAL, Université Paris-Sud, CNRS/IN2P3, Orsay, France*
[24] *LLR, Ecole Polytechnique, CNRS/IN2P3, Palaiseau, France*
[25] *Faculty of Science, University of Montenegro, Podgorica, Montenegro*[k]
[26] *Institute of Physics, Academy of Sciences of the Czech Republic, Praha, Czech Republic*[f]
[27] *Faculty of Mathematics and Physics, Charles University, Praha, Czech Republic*[f]
[28] *Dipartimento di Fisica Università di Roma Tre and INFN Roma 3, Roma, Italy*
[29] *Institute for Nuclear Research and Nuclear Energy, Sofia, Bulgaria*
[30] *Institute of Physics and Technology of the Mongolian Academy of Sciences, Ulaanbaatar, Mongolia*
[31] *Paul Scherrer Institut, Villigen, Switzerland*
[32] *Fachbereich C, Universität Wuppertal, Wuppertal, Germany*
[33] *Yerevan Physics Institute, Yerevan, Armenia*
[34] *DESY, Zeuthen, Germany*
[35] *Institut für Teilchenphysik, ETH, Zürich, Switzerland*[g]
[36] *Physik-Institut der Universität Zürich, Zürich, Switzerland*[g]

[37] *Also at Rechenzentrum, Universität Wuppertal, Wuppertal, Germany*
[38] *Also at IPNL, Université Claude Bernard Lyon 1, CNRS/IN2P3, Villeurbanne, France*
[39] *Also at CERN, Geneva, Switzerland*
[40] *Also at Ulaanbaatar University, Ulaanbaatar, Mongolia*
[41] *Supported by the Initiative and Networking Fund of the Helmholtz Association (HGF) under the contract VH-NG-401 and S0-072*
[42] *Also at Moscow Institute of Physics and Technology, Moscow, Russia*
[43] *Also at Department of Physics, University of Toronto, Toronto, Ontario, Canada M5S 1A7*
[44] *Also at LAPP, Université de Savoie, CNRS/IN2P3, Annecy-le-Vieux, France*
[45] *Department of Physics, Oxford University, Oxford, UK*[b]

[a] *Supported by the Bundesministerium für Bildung und Forschung, FRG, under contract numbers 05H09GUF, 05H09VHC, 05H09VHF, 05H16PEA*
[b] *Supported by the UK Science and Technology Facilities Council, and formerly by the UK Particle Physics and Astronomy Research Council*
[c] *Supported by FNRS-FWO-Vlaanderen, IISN-IIKW and IWT and by Interuniversity Attraction Poles Programme, Belgian Science Policy*
[d] *Partially Supported by Polish Ministry of Science and Higher Education, grant DPN/N168/DESY/2009*
[e] *Supported by VEGA SR grant no. 2/7062/ 27*
[f] *Supported by the Ministry of Education of the Czech Republic under the projects LC527, INGO-LA09042 and MSM0021620859*
[g] *Supported by the Swiss National Science Foundation*
[h] *Supported by CONACYT, México, grant 48778-F*
[i] *Russian Foundation for Basic Research (RFBR), grant no 1329.2008.2 and Rosatom*
[j] *Supported by the Romanian National Authority for Scientific Research under the contract PN 09370101*
[k] *Partially Supported by Ministry of Science of Montenegro, no. 05-1/3-3352*

1 Introduction

Jet production in neutral current (NC) deep-inelastic *ep* scattering (DIS) at HERA is an important process to study the strong interaction and its theoretical description by Quantum Chromodynamics (QCD) [1, 2, 3, 4]. Due to the asymptotic freedom of QCD, quarks and gluons participate as quasi-free particles in short distance interactions. At larger distances they hadronise into collimated jets of hadrons, which provide momentum information of the underlying partons. Thus, the jets can be measured and compared to perturbative QCD (pQCD) predictions, corrected for hadronisation effects. This way the theory can be tested, and the value of the strong coupling, $\alpha_s(M_Z)$, as well as its running can be measured with high precision. A comprehensive review of jets in *ep* scattering at HERA is given in [5].

In contrast to inclusive DIS, where the dominant effects of the strong interactions are the scaling violations of the proton structure functions, the production of jets allows for a direct measurement of the strong coupling α_s. If the measurement is performed in the Breit frame of reference [6, 7], where the virtual boson collides head on with a parton from the proton, the Born level contribution to DIS (figure 1a) generates no transverse momentum. Significant transverse momentum P_T in the Breit frame is produced at leading order (LO) in the strong coupling α_s by boson-gluon fusion (figure 1b) and the QCD Compton (figure 1c) processes. In LO the proton's longitudinal momentum fraction carried by the parton participating in the hard interaction is given by $\xi = x(1 + M_{12}^2/Q^2)$. The variables x, M_{12} and Q^2 denote the Bjorken scaling variable, the invariant mass of the two jets and the negative four-momentum transfer squared, respectively. In the kinematic regions of low Q^2, low P_T and low ξ, boson-gluon fusion dominates jet production and provides direct sensitivity to terms proportional to the product of α_s and the gluon component of the proton structure. At high Q^2 and high P_T the QCD Compton processes are dominant, which are sensitive to the valence quark densities and α_s. Calculations in pQCD in LO for inclusive jet and dijet production in the Breit frame are of $\mathcal{O}(\alpha_s)$ and for trijet production (figure 1d) of $\mathcal{O}(\alpha_s^2)$.

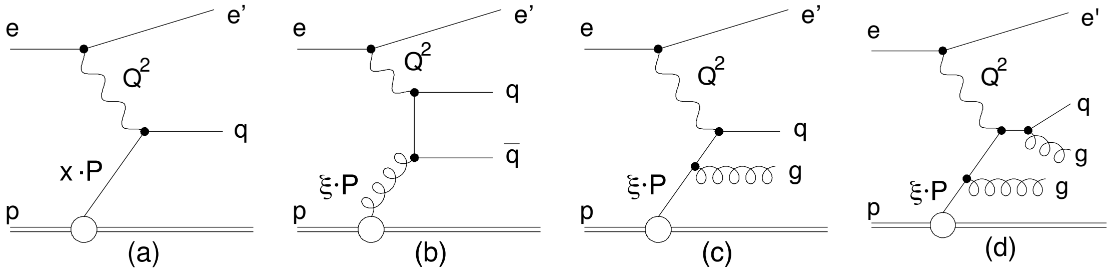

Figure 1: Deep-inelastic *ep* scattering at different orders in α_s: (a) Born contribution $\mathcal{O}(\alpha_{\rm em}^2)$, (b) example of boson-gluon fusion $\mathcal{O}(\alpha_{\rm em}^2\alpha_s)$, (c) example of QCD Compton scattering $\mathcal{O}(\alpha_{\rm em}^2\alpha_s)$ and (d) example of a trijet process $\mathcal{O}(\alpha_{\rm em}^2\alpha_s^2)$.

Recent publications by the ZEUS collaboration concerning jet production in DIS dealt with cross sections of dijet [8] and inclusive jet production [9], whereas recent H1 publications dealt with multijet production and the determination of the strong coupling constant $\alpha_s(M_Z)$ at low Q^2 [10] and at high Q^2 [11].

In this paper double-differential measurements are presented of absolute and normalised inclusive jet, dijet and trijet cross sections in the Breit frame. Two different jet algorithms, the k_T [12] and the anti$-k_T$ [13] algorithm, are explored. The cross sections are measured as a function of Q^2 and the transverse jet momentum P_T^{jet} for the case of inclusive jets. Dijet and trijet cross sections are measured as a function of Q^2 and the average jet transverse momentum. In addition, dijet and trijet cross sections are measured as a function of Q^2 and the proton's longitudinal momentum fraction ξ. The measurements of the ratios of the number of inclusive jets as well as dijet and trijet events to the number of inclusive NC DIS events in the respective bins of Q^2, referred to as normalised multijet cross sections, are also reported. In comparison to absolute jet cross sections these measurements profit from a significant reduction of the systematic experimental uncertainties.

The analysis reported here profits from improvements in the reconstruction of tracks and calorimetric energies, together with a new calibration of the hadronic energy. They lead to a reduction of the jet energy scale uncertainty to 1 % [14] and allow an extension of the pseudorapidity[1] range of the reconstructed jets in the laboratory rest frame from 2.0 to 2.5 in the proton direction and from -0.8 to -1.0 in the photon direction, compared to a previous analysis [11]. The increase in phase space allows the trijet cross section to be measured double-differentially for the first time at HERA. The measurements presented in this paper supersede the previously published normalised multijet cross sections [11], which include in addition to the data used in the present analysis data from the HERA-I running period, yielding an increase in statistics of about 10 %. However, the above mentioned improvements in the present analysis, which uses only data from the HERA-II running period, outweigh the small benefit from the additional HERA-I data and yield an overall better precision of the results.

In order to match the improved experimental precision, the results presented here are extracted using a regularised unfolding procedure which properly takes into account detector effects, like acceptance and migrations, as well as statistical correlations between the different observables.

The measurements are compared to perturbative QCD predictions at NLO corrected for hadronisation effects. Next-to-next-to-leading order (NNLO) jet calculations in DIS or approximations beyond NLO are not available yet. The strong coupling α_s is extracted as a function of the hard scale chosen for jet production in DIS.

2 Experimental Method

The data sample was collected with the H1 detector at HERA in the years 2003 to 2007 when HERA collided electrons or positrons[2] of energy $E_e = 27.6$ GeV with protons of energy $E_p = 920$ GeV, providing a centre-of-mass energy of $\sqrt{s} = 319$ GeV. The data sample used in this analysis corresponds to an integrated luminosity of 351 pb^{-1}, of which 160 pb^{-1} were recorded in $e^- p$ collisions and 191 pb^{-1} in $e^+ p$ collisions.

[1] The pseudorapidity is related to the polar angle θ, defined with respect to the proton beam direction, by $\eta = -\ln\tan(\theta/2)$.

[2] Unless otherwise stated, the term "electron" is used in the following to refer to both electron and positron.

2.1 The H1 detector

A detailed description of the H1 detector can be found elsewhere [15,16,17]. The right-handed coordinate system of H1 is defined such that the positive z-axis is in the direction of the proton beam (forward direction), and the nominal interaction point is located at $z = 0$. The polar angle θ and azimuthal angle ϕ are defined with respect to this axis.

The essential detector components for this analysis are the Liquid Argon (LAr) calorimeter and the central tracking detector (CTD), which are both located inside a 1.16 T solenoidal magnetic field.

Electromagnetic and hadronic energies are measured using the LAr calorimeter in the polar angular range $4^\circ < \theta < 154^\circ$ and with full azimuthal coverage [17]. The LAr calorimeter consists of an electromagnetic section made of lead absorbers between 20 and 30 radiation lengths and a hadronic section with steel absorbers. The total depth of the LAr calorimeter varies between 4.5 and 8 hadronic interaction lengths. The calorimeter is divided into eight wheels along the beam axis, each consisting of eight absorber stacks arranged in an octagonal formation around the beam axis. The electromagnetic and the hadronic sections are highly segmented in the transverse and the longitudinal directions with in total 45000 readout cells. The energy resolution is $\sigma_E/E = 11\,\%/\sqrt{E\,/\mathrm{GeV}} \oplus 1\%$ for electromagnetic energy deposits and $\sigma_E/E \simeq 50\,\%/\sqrt{E\,/\mathrm{GeV}} \oplus 3\,\%$ for pions, as obtained from electron and pion test beam measurements [18,19]. In the backward region ($153^\circ < \theta < 174^\circ$) energy deposits are measured by a lead/scintillating fibre Spaghetti-type Calorimeter (SpaCal), composed of an electromagnetic and an hadronic section [20,21].

The CTD, covering $15^\circ < \theta < 165^\circ$, is located inside the LAr calorimeter and consists of drift and proportional chambers, complemented by a silicon vertex detector covering the range $30^\circ < \theta < 150^\circ$ [22]. The trajectories of charged particles are measured with a transverse momentum resolution of $\sigma_{P_\mathrm{T}}/P_\mathrm{T} \simeq 0.2\,\%\ P_\mathrm{T}/\mathrm{GeV} \oplus 1.5\,\%$.

The luminosity is determined from the rate of the elastic QED Compton process with the electron and the photon detected in the SpaCal calorimeter [23].

2.2 Reconstruction and calibration of the hadronic final state

In order to obtain a high experimental precision in the measurement of jet cross sections and the determination of $\alpha_s(M_Z)$, the hadronic jet energy scale uncertainty needs to be minimised. It has been so far the dominant experimental uncertainty in jet measurements. Details on an improved procedure to achieve a jet energy scale uncertainty of 1 % can be found elsewhere [14] and are briefly summarised here.

After removal of the compact energy deposit (cluster) in the electromagnetic part of the LAr calorimeter and the track associated with the scattered electron, the remaining electromagnetic and hadronic clusters and charged tracks are attributed to the hadronic final state (HFS). It is reconstructed using an energy flow algorithm [24,25,26], combining information from tracking and calorimetric measurements, which avoids double counting of measured energies. This algorithm provides an improved jet resolution compared to a purely calorimetric jet measurement, due to the superior resolution of the tracking detectors for charged hadrons.

For the final re-processing of the H1 data and subsequent analyses using these data, further improvements have been implemented. The track and vertex reconstruction is performed using a double-helix trajectory, thus taking multiple scatterings in the detector material better into account. The calorimetric measurement benefits from a separation of hadronic and electromagnetic showers based on shower shape estimators and neural networks [27, 28] for determining the probability that the measured energy deposit of a cluster in the electromagnetic part of the LAr calorimeter is originating from an electromagnetic or hadronic shower. This improves the calorimetric measurement, since the non-compensating LAr calorimeter has a different response for incident particles leading to hadronic or electromagnetic showers. The neural networks are trained [14] for each calorimeter wheel separately, using a mixture of neutral pions, photons and charged particles for the simulation of electromagnetic and hadronic showers. The most important discriminants are the energy fractions in the calorimeter layers and the longitudinal first and second moments. Additional separation power is gained by the covariance between the longitudinal and radial shower extent and the longitudinal and radial kurtosis. The neural network approach was tested on data using identified electrons and jets and shows an improved efficiency for the identification of purely electromagnetic or hadronic clusters, compared to the previously used algorithm.

neutral pions and photons for the generation of electromagnetic showers and charged pions are used for simulating hadronic showers.

The overconstrained NC DIS kinematics allows for the in situ calibration of the energy scale of the HFS using a single-jet calibration event sample [14], employing the mean value of the P_{T}–balance distribution, defined as $P_{\mathrm{T,bal}} = \langle P_{\mathrm{T}}^{\mathrm{h}}/P_{\mathrm{T}}^{\mathrm{da}} \rangle$. The transverse momentum of the HFS, $P_{\mathrm{T}}^{\mathrm{h}}$, is calculated by summing the momentum components $P_{i,x}$ and $P_{i,y}$ of all HFS objects i,

$$P_{\mathrm{T}}^{\mathrm{h}} = \sqrt{\left(\sum_{i\in\mathrm{h}} P_{i,x}\right)^2 + \left(\sum_{i\in\mathrm{h}} P_{i,y}\right)^2} \,. \tag{1}$$

The expected transverse momentum $P_{\mathrm{T}}^{\mathrm{da}}$ is calculated using the double-angle method, which, to a good approximation, is insensitive to the absolute energy scale of the HFS measurement. It makes use of the angles of the scattered electron θ_{e} and of the inclusive hadronic angle γ_{h} [29, 30], to define $P_{\mathrm{T}}^{\mathrm{da}}$ as

$$P_{\mathrm{T}}^{\mathrm{da}} = \frac{2E_{\mathrm{e}}}{\tan\frac{\gamma_{\mathrm{h}}}{2} + \tan\frac{\theta_{\mathrm{e}}}{2}} \,. \tag{2}$$

Calibration functions for calorimeter clusters are derived, depending on their probability to originate from electromagnetically or hadronically induced showers. They are chosen to be smooth functions depending on the cluster energy and polar angle. The free parameters of the calibration functions are obtained in a global χ^2 minimisation procedure, where χ^2 is calculated from the deviation of the value of $P_{\mathrm{T,bal}}$ from unity in bins of several variables. Since no jets are required at this stage, all calorimeter clusters are calibrated. The uncertainty on the energy measurement of individual clusters is referred to as residual cluster energy scale (RCES). In addition, further calibration functions for clusters associated to jets measured in the laboratory frame are derived. This function depends on the jet pseudorapidity, $\eta^{\mathrm{jet}}_{\mathrm{lab}}$, and transverse momentum, $P^{\mathrm{jet}}_{\mathrm{T,lab}}$. It provides an improved calibration for those clusters which are detected in the dense environment of a jet. The calibration procedure described above is applied both to data and to Monte Carlo (MC) event simulations. Track-based four-vectors of the HFS are not affected by the new calibration procedure.

The double-ratio of the $P_{\mathrm{T,bal}}$-ratio of data to MC simulations, after the application of the new calibration constants, is shown for the one-jet calibration sample and for a statistically independent dijet sample in figure 2 as a function of $P^{\mathrm{da}}_{\mathrm{T}}$. Good agreement between data and simulation is observed over the full detector acceptance. This corresponds to a precision of 1 % on the jet energy scale in the kinematic domain of the measurements.

2.3 Event selection

The NC DIS events are triggered and selected by requiring a cluster in the electromagnetic part of the LAr calorimeter. The scattered electron is identified as the isolated cluster of highest transverse momentum, with a track associated to it. Details of the isolation criteria and the electron finding algorithm can be found elsewhere [31]. The electromagnetic energy calibration and the alignment of the H1 detector are performed following the procedure as in [31]. The reconstructed electron energy E'_{e} is required to exceed 11 GeV, for which the trigger efficiency is close to unity. Only those regions of the calorimeter where the trigger efficiency is greater than 98 % are used for the detection of the scattered electron, which corresponds to about 90 % of the η–ϕ-region covered by the LAr calorimeter. These two requirements, on E'_{e} and η–ϕ, ensure the overall trigger efficiency to be above 99.5 % [32]. In the central region, $30^\circ < \theta_{\mathrm{e}} < 152^\circ$, where θ_{e} denotes the polar angle of the reconstructed scattered electron, the cluster is required to be associated with a track measured in the CTD, matched to the primary event vertex. The requirement of an associated track reduces the amount of wrongly identified scattered leptons to below 0.3 %. The z-coordinate of the primary event vertex is required to be within ± 35 cm of the nominal position of the interaction point.

The total longitudinal energy balance, calculated as the difference of the total energy E and the longitudinal component of the total momentum P_{z}, using all detected particles including the scattered electron, has little sensitivity to losses in the proton beam direction and is thus only weakly affected by the incomplete reconstruction of the proton remnant. Using energy-momentum conservation, the relation $E - P_{\mathrm{z}} \simeq 2E_{\mathrm{e}} = 55.2\,\mathrm{GeV}$ holds for DIS events. The requirement $45 < E - P_{\mathrm{z}} < 65$ GeV thus reduces the contribution of DIS events with hard initial state photon radiation. For the latter events, the undetected photons, propagating predominantly in the negative z-direction, lead to values of $E - P_{\mathrm{z}}$ significantly lower than the expected value of 55.2 GeV. The $E - P_{\mathrm{z}}$ requirement together with the scattered electron selection also reduces background contributions from photoproduction, where no scattered electron is expected to be detected, to less than 0.2 %. Cosmic muon and beam induced backgrounds are reduced to a negligible level after the application of a dedicated cosmic muon finder algorithm. QED Compton processes are reduced to 1 % by requiring the acoplanarity $A = \cos(|\pi - \Delta\phi|)$ to be smaller than 0.95, with $\Delta\phi$ being the azimuthal angle between the scattered lepton and an identified photon with energy larger than 4 GeV. The background from lepton pair production processes is found to be negligible. Also backgrounds from charged current processes and deeply virtual Compton scattering are found to be negligible. The backgrounds originating from the sources discussed above are modelled using a variety of MC event generators as described in [14].

The event selection of the analysis is based on an extended analysis phase space defined by $100 < Q^2 < 40\,000\,\mathrm{GeV}^2$ and $0.08 < y < 0.7$, where $y = Q^2/(sx)$ quantifies the inelasticity of the interaction. Jets are also selected within an extended range in $P_{\mathrm{T}}^{\mathrm{jet}}$ and $\eta_{\mathrm{lab}}^{\mathrm{jet}}$ as described in sect. 2.4. The extended analysis phase space and the measurement phase space are summarised in table 1.

The variables Q^2 and y are reconstructed from the four-momenta of the scattered electron and the hadronic final state particles using the electron-sigma method [33, 34],

$$Q^2 = 4E_{\mathrm{e}}E'_{\mathrm{e}}\cos^2\frac{\theta_{\mathrm{e}}}{2} \quad \text{and} \quad y = y_\Sigma \frac{2E_{\mathrm{e}}}{\Sigma + E'_{\mathrm{e}}(1 - cos\theta_{\mathrm{e}})} \tag{3}$$

$$\text{with} \quad y_\Sigma = \frac{\Sigma}{\Sigma + E'_{\mathrm{e}}(1 - \cos\theta_{\mathrm{e}})} \quad \text{and} \quad \Sigma = \sum_{i\in\mathrm{h}}(E_i - P_{i,z}) \;, \tag{4}$$

where Σ is calculated by summing over all hadronic final state particles i with energy E_i and longitudinal momentum $P_{i,z}$.

2.4 Reconstruction of jet observables

The jet finding is performed in the Breit frame of reference, where the boost from the laboratory system is determined by Q^2, y and the azimuthal angle ϕ_{e} of the scattered electron [35]. Particles of the hadronic final state are clustered into jets using the inclusive k_{T} [12] or alternatively the anti$-k_{\mathrm{T}}$ [13] jet algorithm. The jet finding is implemented in FastJet [36], and the massless P_{T} recombination scheme and the distance parameter $R_0 = 1$ in the η–ϕ plane are used. MC studies of the reconstruction performance and comparisons between jets on detector, hadron and parton level indicate that $R_0 = 1$ is a good choice for the phase space of this analysis. This is also in agreement with the result reported in [37]. The transverse component of the jet four-vector with respect to the z-axis in the Breit frame is referred to as $P_{\mathrm{T}}^{\mathrm{jet}}$. The jets are required to have $P_{\mathrm{T}}^{\mathrm{jet}} > 3$ GeV.

The jet axis is transformed to the laboratory rest frame, and jets with a pseudorapidity in the laboratory frame of $-1.5 < \eta_{\mathrm{lab}}^{\mathrm{jet}} < 2.75$ are selected. Furthermore, the transverse momentum of jets with respect to the beam-axis in the laboratory frame is restricted to $P_{\mathrm{T,lab}}^{\mathrm{jet}} > 2.5\,\mathrm{GeV}$. This requirement removes only a few very soft jets which are not well measured and is not part of the phase space definition.

Inclusive jets are defined by counting all jets in a given event with $P_{\mathrm{T}}^{\mathrm{jet}} > 3\,\mathrm{GeV}$. Dijet and trijet events are selected by requiring at least two or three jets with $3 < P_{\mathrm{T}}^{\mathrm{jet}} < 50\,\mathrm{GeV}$, such that the trijet sample is a subset of the dijet sample. The measurement is performed as a function of the average transverse momentum $\langle P_{\mathrm{T}}\rangle_2 = \frac{1}{2}(P_{\mathrm{T}}^{\mathrm{jet1}} + P_{\mathrm{T}}^{\mathrm{jet2}})$ and $\langle P_{\mathrm{T}}\rangle_3 = \frac{1}{3}(P_{\mathrm{T}}^{\mathrm{jet1}} + P_{\mathrm{T}}^{\mathrm{jet2}} + P_{\mathrm{T}}^{\mathrm{jet3}})$ of the two or three leading jets for the dijet and trijet measurement, respectively. Furthermore, dijet and trijet cross sections are measured as a function of the observables $\xi_2 = x\left(1 + M_{12}^2/Q^2\right)$ and $\xi_3 = x\left(1 + M_{123}^2/Q^2\right)$, respectively, with M_{123} being the invariant mass of the three leading jets.

	Extended analysis phase space	**Measurement phase space for jet cross sections**
NC DIS phase space	$100 < Q^2 < 40\,000\,\mathrm{GeV}^2$ $0.08 < y < 0.7$	$150 < Q^2 < 15\,000\,\mathrm{GeV}^2$ $0.2 < y < 0.7$
Jet polar angular range	$-1.5 < \eta^{\mathrm{jet}}_{\mathrm{lab}} < 2.75$	$-1.0 < \eta^{\mathrm{jet}}_{\mathrm{lab}} < 2.5$
Inclusive jets	$P^{\mathrm{jet}}_{\mathrm{T}} > 3\,\mathrm{GeV}$	$7 < P^{\mathrm{jet}}_{\mathrm{T}} < 50\,\mathrm{GeV}$
Dijets and trijets	$3 < P^{\mathrm{jet}}_{\mathrm{T}} < 50\,\mathrm{GeV}$	$5 < P^{\mathrm{jet}}_{\mathrm{T}} < 50\,\mathrm{GeV}$ $M_{12} > 16\,\mathrm{GeV}$

Table 1: Summary of the extended analysis phase space and the measurement phase space of the jet cross sections.

The observables ξ_2 and ξ_3 provide a good approximation of the proton's longitudinal momentum fraction ξ carried by the parton which participates in the hard interaction.

2.5 Measurement phase space and extended analysis phase space

The NC DIS and the jet phase space described above refers to an extended analysis phase space compared to the measurement phase space for which the results are quoted. Extending the event selection to a larger phase space helps to quantify migrations at the phase space boundaries, thereby improving the precision of the measurement. The actual measurement is performed in the NC DIS phase space given by $150 < Q^2 < 15\,000\,\mathrm{GeV}^2$ and $0.2 < y < 0.7$. Jets are required to have $-1.0 < \eta^{\mathrm{jet}}_{\mathrm{lab}} < 2.5$, which ensures that they are well contained within the acceptance of the LAr calorimeter and well calibrated. For the inclusive jet measurement, each jet has to fulfil the requirement $7 < P^{\mathrm{jet}}_{\mathrm{T}} < 50\,\mathrm{GeV}$. For the dijet and trijet measurements jets are considered with $5 < P^{\mathrm{jet}}_{\mathrm{T}} < 50\,\mathrm{GeV}$, and, in order to avoid regions of phase space where calculations in fixed order perturbation theory are not reliable [38,39], an additional requirement on the invariant mass of $M_{12} > 16\,\mathrm{GeV}$ is imposed. This ensures a better convergence of the perturbative series at NLO , which is essential for the comparison of the NLO calculation with data and the extraction of α_s. The extended analysis and the measurement phase space are summarised in table 1.

2.6 Monte Carlo simulations

The migration matrices needed for the unfolding procedure (see section 3) are determined using simulated NC DIS events. The generated events are passed through a detailed GEANT3 [40] based simulation of the H1 detector and subjected to the same reconstruction and analysis chains as are used for the data. The following two Monte Carlo (MC) event generators are used for this purpose, both implementing LO matrix elements for NC DIS, boson-gluon fusion and QCD Compton events. The CTEQ6L [41] parton density functions (PDFs) are used. Higher order parton emissions are simulated in DJANGOH [42] according to the colour dipole model, as implemented in Ariadne [43,44], and in RAPGAP [45,46] with parton showers in the leading-logarithmic approximation. In both MC programs hadronisation is modelled with the Lund string fragmentation [47, 48] using the ALEPH tune [49]. The effects of QED radiation and electroweak effects are simulated using the HERACLES [50] program, which is interfaced to the RAPGAP, DJANGOH and LEPTO [51] event generators. The latter one is used to correct the e^+p and e^-p data for their different electroweak effects (see section 5.3).

3 Unfolding

The jet data are corrected for detector effects using a regularised unfolding method which is described in the following. The matrix based unfolding method as implemented in the TUnfold package [52] is employed. A detector response matrix is constructed for the unfolding of the neutral current DIS, the inclusive jet, the dijet and the trijet measurements simultaneously [53]. The unfolding takes into account the statistical correlations between these measurements as well as the statistical correlations of several jets originating from a single event. The corrections for QED radiation are included in the unfolding procedure. Jet cross sections and normalised jet cross sections at hadron level are determined using this method. The hadron level refers to all stable particles in an event with a proper lifetime larger than $c\tau > 10\,\text{mm}$. It is obtained from MC event generators by selecting all particles after hadronisation and subsequent particle decays.

3.1 Weighting of MC models to describe data

Both RAPGAP and DJANGOH provide a fair description of the experimental data for the inclusive NC DIS events and the multijet samples. To further improve the agreement between reconstructed Monte Carlo events and the data, weights are applied to selected observables on hadron level. The weights are obtained iteratively from the ratio of data to the reconstructed MC distributions and are applied to events on hadron level. The observables of the inclusive NC DIS events are in general well described and are not weighted. An exception is the inelasticity y. The slope of this distribution is not described satisfactorily, where at low values of y the disagreement amounts to about 5 % between the data and the LO MC prediction. Since this quantity is important, as it enters in the calculation of the boost to the Breit frame, it was weighted to provide a good description of the data.

The MC models, simulating LO matrix elements and parton showers, do not provide a good description of higher jet multiplicities. Event weights are applied for the jet multiplicity as a function of Q^2. The MC models are also not able to reproduce well the observed $P_{\mathrm{T}}^{\mathrm{jet}}$ spectra at high $P_{\mathrm{T}}^{\mathrm{jet}}$ and the pseudorapidity distribution of the jets. Thus, weights are applied depending on the transverse momentum and pseudorapidity of the jet with the highest (most forward) pseudorapidity in the event as well as for the jet with the smallest (most backward) pseudorapidity in the event. Additional weights are applied for trijet events as a function of the sum of $P_{\mathrm{T}}^{\mathrm{jet}}$ of the three leading jets. The weights are typically determined as two-dimensional 2$^{\text{nd}}$ degree polynomials with either $P_{\mathrm{T,fwd}}^{\mathrm{jet}}$, $P_{\mathrm{T,bwd}}^{\mathrm{jet}}$ or Q^2 as the second observable to ensure that no discontinuities are introduced [14]. These weights are derived and applied in the extended analysis phase space (see section 2.3 and table 1) in order to control migrations in the unfolding from outside into the measurement phase space. After application of the weights, the simulations provide a good description of the shapes of all data distributions, some of which are shown in figures 3, 4, 5 and 6.

3.2 Regularised unfolding

The events are counted in bins, where the bins on hadron level are arranged in a vector $\vec{x}$ with dimension 1370, and the bins on detector level are arranged in a vector $\vec{y}$ with dimension 4562. The vectors $\vec{x}$ and $\vec{y}$ are connected by a folding equation $\vec{y} = \boldsymbol{A}\vec{x}$, where $\boldsymbol{A}$ is a matrix of probabilities, the detector response matrix. It accounts for migration effects and efficiencies. The element A_{ij} of $\boldsymbol{A}$ quantifies the probability to detect an event in bin i of $\vec{y}$, given that it was produced in bin j of $\vec{x}$. Given a vector of measurements $\vec{y}$, the unknown hadron level distribution $\vec{x}$ is estimated [52] in a linear fit, by determining the minimum of

$$\chi^2 = \chi^2_{\mathrm{A}} + \chi^2_{\mathrm{L}} := (\vec{y} - \boldsymbol{A}\vec{x})^{\mathrm{T}} \boldsymbol{V}_y^{-1} (\vec{y} - \boldsymbol{A}\vec{x}) + \tau^2 (\vec{x} - \vec{x}_0)^{\mathrm{T}} (\mathbf{L}^{\mathrm{T}}\mathbf{L}) (\vec{x} - \vec{x}_0) , \tag{5}$$

where $\boldsymbol{V}_y$ is the covariance matrix on detector level, and χ^2_{L} is a regularisation term to suppress fluctuations of the result. The regularisation parameter τ is a free parameter. The matrix $\mathbf{L}$ contains the regularisation condition and is set to unity. The bias vector $\vec{x}_0$ represents the hadron level distribution of the MC model. The detector response matrix $\boldsymbol{A}$ is constructed from another matrix $\boldsymbol{M}$ [52], called migration matrix throughout this paper. The migration matrix is obtained by counting MC jets or events in bins of $\vec{x}$ and $\vec{y}$. It is determined by averaging the matrices obtained from two independent samples of simulated events by the DJANGOH and RAPGAP generators. It also contains an extra row, $\vec{\varepsilon}$, to account for inefficiencies, i.e. for events which are not reconstructed in any bin of $\vec{y}$.

QED radiative corrections are included in the unfolding as efficiency corrections [53]. The running of the electromagnetic coupling $\alpha_{\mathrm{em}}(\mu_r)$ is not corrected for. The size of the radiative corrections is of order 10 % for absolute jet cross sections and of order 5 % for normalised jet cross sections.

Prior to solving the folding equation, the remaining small backgrounds in the data from the QED Compton process and from photoproduction after the event selection are subtracted from the input data [52] using simulated MC jets or events. Also MC simulated DIS events with inelasticity $y > 0.7$ on hadron level, and thus from outside the accepted phase space, are considered as background and are subtracted from data. These contributions cannot be determined reliably from data, since the cut on E'_{e} results in a low reconstruction efficiency for events with $y > 0.7$ on detector level. The contribution from such events is less than 1 % in any bin of the cross section measurement.

A given event with jets may produce entries in several bins of $\vec{y}$. This introduces correlations between bins of $\vec{y}$ which lead to off-diagonal entries in the covariance matrix $\boldsymbol{V}_y$.

3.3 Definition of the migration matrix

The migration matrix is composed of a 4×4 structure of submatrices representing the four different data samples (NC DIS, inclusive jet, dijet and trijet), thus enabling a simultaneous unfolding of NC DIS and jet cross sections. It is schematically illustrated in figure 7. The four submatrices $\boldsymbol{E}$, $\boldsymbol{J}_1$, $\boldsymbol{J}_2$ and $\boldsymbol{J}_3$ represent the migration matrices for the NC DIS, the inclusive jet, the dijet and the trijet measurements, respectively. Hadron-level jets or events which do not fulfil the reconstruction cuts are filled into the additional vector $\vec{\varepsilon}$. The three submatrices $\boldsymbol{B}_1$, $\boldsymbol{B}_2$ and $\boldsymbol{B}_3$ connect the jet measurements on detector level with the hadron level of the NC DIS measurement. They are introduced to account for cases where a jet or an event is reconstructed, although it is absent on hadron level. Such detector-level-only contributions are present due to different jet multiplicities on detector and on hadron level, caused by limited detector resolution and by acceptance effects. The unfolding procedure determines the normalisation of these detector-level-only contributions from data. Each entry in one of the submatrices $\boldsymbol{B}_i$ is compensated by a negative entry in the efficiency bin (denoted as β_i in figure 7), in order to preserve the normalisation of the NC DIS measurement. The four submatrices, $\boldsymbol{E}$, $\boldsymbol{J}_1$, $\boldsymbol{J}_2$ and $\boldsymbol{J}_3$, are explained in the following. More details can be found in [53].

- **NC DIS ($\boldsymbol{E}$):** For the measurement of the NC DIS cross sections a two-dimensional unfolding considering migrations in Q^2 and y is used. On detector level 14 bins in Q^2 times 3 bins in y ($0.08 < y < 0.7$) are used to determine 8 bins in Q^2 times 2 bins in y on hadron level. Out of these 16 bins, only 6 bins are used for the determination of the normalised cross sections.

- **Inclusive jets ($\boldsymbol{J}_1$):** The unfolding of the inclusive jet measurement is performed as a four-dimensional unfolding, where migrations in the observables Q^2, y, $P_{\mathrm{T}}^{\mathrm{jet}}$ and $\eta_{\mathrm{lab}}^{\mathrm{jet}}$ are considered. To model the migrations, jets found on hadron level are matched to detector-level jets, employing a closest-pair algorithm with the distance parameter $R = \sqrt{\Delta\phi^2 + \Delta\eta^2}$ and a requirement of $R < 0.9$. Here $\Delta\phi$ and $\Delta\eta$ are the distances between detector level and hadron level jets in ϕ and η in the laboratory rest frame, respectively. Detector-level-only jets which are not matched on hadron level are filled into the submatrix $\boldsymbol{B}_1$ and are therefore determined from data. Hadron-level jets which are not matched on detector level are filled into the vector $\vec{\varepsilon_1}$. The bin grid in Q^2 and y is defined in the same way as for the NC DIS case. Migrations in $P_{\mathrm{T}}^{\mathrm{jet}}$ are described using 16 bins on detector level and 8 bins on hadron level. Migrations in $\eta_{\mathrm{lab}}^{\mathrm{jet}}$ within $-1.0 < \eta_{\mathrm{lab}}^{\mathrm{jet}} < 2.5$ are described by a 3 times 2 structure. Additional bins (differential in $P_{\mathrm{T}}^{\mathrm{jet}}$, Q^2 and y) are used to describe migrations of jets in $\eta_{\mathrm{lab}}^{\mathrm{jet}}$ with $\eta_{\mathrm{lab}}^{\mathrm{jet}} < -1.0$ or $\eta_{\mathrm{lab}}^{\mathrm{jet}} > 2.5$. The results of the 7 times 2 bins within the measurement phase space in $P_{\mathrm{T}}^{\mathrm{jet}}$ and $\eta_{\mathrm{lab}}^{\mathrm{jet}}$ are finally combined to obtain the 4 bins for the cross section measurement for each Q^2 bin.

- **Dijet ($\boldsymbol{J}_2$):** Dijet events are unfolded using a three-dimensional unfolding, where migrations in Q^2, y and $\langle P_{\mathrm{T}}\rangle_2$ are considered. Also taken into account are migrations at the phase space boundaries in M_{12}, $P_{\mathrm{T}}^{\mathrm{jet2}}$ and $\eta_{\mathrm{lab}}^{\mathrm{jet}}$. The bin grid in Q^2 and y is identical to the one used for the NC DIS unfolding. Migrations in $\langle P_{\mathrm{T}}\rangle_2$ are described using 18 bins on detector level and 11 bins on hadron level, out of which 8 bins are combined to obtain the 4 data points of interest. Migrations in M_{12}, $P_{\mathrm{T}}^{\mathrm{jet2}}$ and $\eta_{\mathrm{lab}}^{\mathrm{jet}}$ are described by additional bins, which are each further binned in $\langle P_{\mathrm{T}}\rangle_2$ and y.

- **Trijet ($\boldsymbol{J}_3$):** The unfolding of the trijet measurement is performed similarly to the dijet unfolding, using a three-dimensional submatrix in Q^2, y and $\langle P_{\mathrm{T}}\rangle_3$. Migrations in M_{12}, $P_{\mathrm{T}}^{\mathrm{jet3}}$ and $\eta_{\mathrm{lab}}^{\mathrm{jet}}$ are also considered. Due to the limited number of trijet events, the number of bins is slightly reduced compared to the dijet measurement.

Unfolding in the extended analysis phase space increases the stability of the measurement in the measurement phase space to a large extent, in particular for the dijet and trijet data points with $\langle P_{\mathrm{T}} \rangle < 11\,\mathrm{GeV}$. The resulting detector response matrix $\boldsymbol{M}$ has an overall size of 4562×1370 bins, of which about 3 % have a non-zero content. A finer bin grid than the actual measurement bin grid ensures a reduced model dependence in the unfolding procedure. 148 bins on hadron level, located in the measurement phase space, and additional adjacent bins, mostly at low transverse momenta, are combined to arrive at the final 64 cross section bins [53].

For the dijet and trijet measurements as a function of ξ_2 and ξ_3 dedicated new submatrices $\boldsymbol{J}_2$ and $\boldsymbol{J}_3$ are set up.

- The unfolding of the dijet measurement as a function of ξ_2 is performed as a four-dimensional unfolding in the variables Q^2, y, ξ_2 and M_{12}. Including M_{12} in the unfolding reduces the model dependence considerably. Additional bins are further used to account for migrations at the phase space boundaries in M_{12}, $P_{\mathrm{T}}^{\mathrm{jet2}}$ and $\eta_{\mathrm{lab}}^{\mathrm{jet}}$.
- A four-dimensional unfolding is employed in the variables Q^2, y, ξ_3 and M_{123}. Additional bins are considered to describe migrations at the phase space boundaries in M_{12}, $P_{\mathrm{T}}^{\mathrm{jet3}}$ and $\eta_{\mathrm{lab}}^{\mathrm{jet}}$.

3.4 Regularisation strength and condition

The regularisation parameter τ in equation 5 is set to $\tau = 10^{-6}$. In this region no dependence of the results on the value of τ is observed [53]. When alternatively applying the method of the L-curve scan [52] for the choice of τ, a value of $\tau = 7.8 \cdot 10^{-5}$ is obtained with consistent results for the cross sections. Studies of different regularisation conditions L have been performed by approximating first or second derivatives instead of setting L to the unity matrix. Only small dependencies of the measured cross sections and their uncertainties on the choice of L or τ are observed [53].

3.5 Bias tests

The definition of the migration matrix has been optimised using bias tests on simulated events. For this purpose unfolding matrices have been constructed using simulations based on RAPGAP and DJANGOH. When testing the unfolding procedure with independent pseudo-data of the respective Monte Carlo generator, the unfolded distributions match the generated ones within statistical uncertainties and the uncertainties determined in the unfolding have the desired 68% coverage. When using pseudo-data of the Monte Carlo generator different from that used to construct the unfolding matrix instead, only small differences of about $0.3 - 0.4\,\sigma$ are observed between the unfolded and the generated distributions. These small differences are treated as systematic uncertainties, as described in section 4.2.

In addition two different data correction methods have been tested. A matrix inversion method ($\tau = 0$ in equation 5) gives results consistent with those obtained by the unfolding procedure.

A bin-by-bin correction method yields results with a significant bias towards the underlying MC distributions [53] and with improper statistical uncertainties as the correlations among the measurement bins are not accounted for.

4 Jet cross section measurement

4.1 Observables and phase space

The jet cross sections presented are hadron level cross sections. For bin i, the cross section σ_i is defined as

$$\sigma_i = \frac{x_i^{\text{unfolded}}}{\mathcal{L}^+ + \mathcal{L}^-}\,, \tag{6}$$

where x_i^{unfolded} is the unfolded number of jets or events in bin i, including QED radiative corrections. The integrated luminosities are $\mathcal{L}^+ = 191\ \text{pb}^{-1}$ and $\mathcal{L}^- = 160\ \text{pb}^{-1}$for e^+p and e^-p scattering,respectively. The observed cross sections correspond to luminosity weighted averages of e^+p and e^-p processes (see section 5.3). Double-differential jet cross sections are presented for the measurement phase space given in table 1. Inclusive jet, dijet and trijet cross sections are measured as a function of Q^2 and $P_{\text{T}}^{\text{jet}}$ or $\langle P_{\text{T}}\rangle_2$ or $\langle P_{\text{T}}\rangle_3$. Dijets and trijets are also measured as a function of Q^2 and ξ_2 or ξ_3. The phase space in $P_{\text{T}}^{\text{jet}}$ allows measuring the range $0.006 < \xi_2 < 0.316$ for dijets and $0.01 < \xi_3 < 0.50$ for trijets. The trijet phase space is a subset of the dijet phase space, but the observables $\langle P_{\text{T}}\rangle_3$ and ξ_3 are calculated using the three leading jets. The phase space boundaries of the measurements are summarised in table 2.

<table>
<tr><th>Measurement</th><th>NC DIS phase space</th><th colspan="2">Phase space for jet cross sections</th></tr>
<tr><td>$\sigma_{\text{jet}}(Q^2, P_{\text{T}}^{\text{jet}})$</td><td rowspan="5">$150 < Q^2 < 15\,000\ \text{GeV}^2$
$0.2 < y < 0.7$</td><td>$7 < P_{\text{T}}^{\text{jet}} < 50\ \text{GeV}$
$-1.0 < \eta_{\text{lab}}^{\text{jet}} < 2.5$</td><td>$N_{\text{jet}} \geq 1$</td></tr>
<tr><td>$\sigma_{\text{dijet}}(Q^2, \langle P_{\text{T}}\rangle_2)$</td><td rowspan="4">$5 < P_{\text{T}}^{\text{jet}} < 50\ \text{GeV}$
$-1.0 < \eta_{\text{lab}}^{\text{jet}} < 2.5$
$M_{12} > 16\ \text{GeV}$</td><td>$N_{\text{jet}} \geq 2$
$7 < \langle P_{\text{T}}\rangle_2 < 50\ \text{GeV}$</td></tr>
<tr><td>$\sigma_{\text{trijet}}(Q^2, \langle P_{\text{T}}\rangle_3)$</td><td>$N_{\text{jet}} \geq 3$
$7 < \langle P_{\text{T}}\rangle_3 < 30\ \text{GeV}$</td></tr>
<tr><td>$\sigma_{\text{dijet}}(Q^2, \xi_2)$</td><td>$N_{\text{jet}} \geq 2$
$0.006 < \xi_2 < 0.316$</td></tr>
<tr><td>$\sigma_{\text{trijet}}(Q^2, \xi_3)$</td><td>$N_{\text{jet}} \geq 3$
$0.01 < \xi_3 < 0.50$</td></tr>
</table>

Table 2: Summary of the phase space boundaries of the measurements.

The simultaneous unfolding of the NC DIS and the jet measurements allows also the determination of jet cross sections normalised to the NC DIS cross sections. Normalised jet cross sections are defined as the ratio of the double-differential absolute jet cross sections to the NC DIS cross sections σ_{NC} in the respective Q^2-bin, where σ_{NC} is calculated using equation 6. The phase space for the normalised inclusive jet $\sigma_{\text{jet}}/\sigma_{\text{NC}}$, normalised dijet $\sigma_{\text{dijet}}/\sigma_{\text{NC}}$ and normalised trijet $\sigma_{\text{trijet}}/\sigma_{\text{NC}}$ cross sections is identical to the one of the corresponding absolute jet cross sections. The covariance matrix of the statistical uncertainties is determined taking the statistical correlations between the NC DIS and the jet measurements into account. The systematic experimental uncertainties are correlated between the NC DIS and the jet measurements. Consequently, all normalisation uncertainties cancel, and many other systematic uncertainties are reduced signficantly.

4.2 Experimental uncertainties

Statistical and other experimental uncertainties are propagated by analytical linear error propagation through the unfolding process [52].

Systematic uncertainties are estimated by varying the measurement of a given quantity within the experimental uncertainties in simulated events. For each 'up' and 'down' variation, for each source of uncertainty, a new migration matrix is obtained. The difference of these matrices with respect to the nominal unfolding matrix is propagated through the unfolding process [52] to obtain the size of the uncertainty on the cross sections. To avoid fluctuations of the systematic uncertainties caused by limited number of data events, in most cases uncertainties are obtained by unfolding simulated data.

The following sources of systematic uncertainties are taken into account:

- The uncertainty of the energy scale of the HFS is subdivided into two components related to the two-stage calibration procedure described in section 2.2.

  The uncertainties on the cross sections due to the jet energy scale, δ^{JES}, are determined by varying the energy of all HFS objects clustered into jets with $P_{\mathrm{T,lab}}^{\mathrm{jet}} > 7\,\mathrm{GeV}$ by $\pm 1\,\%$. This results in δ^{JES} ranging from 2 to 6 %, with the larger values for high values of $P_{\mathrm{T}}^{\mathrm{jet}}$.

  The energy of HFS objects which are not part of a jet in the laboratory system with $P_{\mathrm{T,lab}}^{\mathrm{jet}} > 7\,\mathrm{GeV}$ is varied separately by $\pm 1\,\%$. This uncertainty is determined using a dijet calibration sample, requiring jets with $P_{\mathrm{T,lab}}^{\mathrm{jet}} > 3\,\mathrm{GeV}$. The resulting uncertainty on the jet cross section is referred to as remaining cluster energy scale uncertainty, δ^{RCES}. The effect of this uncertainty plays a larger rôle at low transverse momenta, where jets in the Breit frame include a larger fraction of HFS objects which are not part of a calibrated jet in the laboratory rest frame. The resulting uncertainty on the jet cross sections is about 1 % for the inclusive jet and the dijet cross sections, and up to 4 % for the trijet cross sections at low transverse momenta.

- The uncertainty $\delta^{\mathrm{LArNoise}}$, due to subtraction of the electronic noise from the LAr electronics, is determined by adding randomly 20 % of all rejected noise clusters to the signal. This increases the jet cross sections by 0.5 % for the inclusive jet data, 0.6 % for the dijet and 0.9 % for the trijet data.

- The energy of the scattered lepton is measured with a precision of 0.5 % in the central and backward region ($z_{\mathrm{impact}} < 100\,\mathrm{cm}$) and with 1 % precision in the forward region of the detector, where z_{impact} is the z-coordinate of the electron's impact position at the LAr calorimeter. The corresponding uncertainty on the jet cross sections, $\delta^{E'_e}$, lies between 0.5 and 2 %, with the larger value at high $P_{\mathrm{T}}^{\mathrm{jet}}$ or high Q^2.

- The position of the LAr calorimeter with respect to the CTD is aligned with a precision of 1 mrad [32], resulting in a corresponding uncertainty of the electron polar angle measurement θ_e. The uncertainty on the jet cross sections, denoted as δ^{θ_e}, is around 0.5 %. Only in the highest Q^2 bin it is up to 1.5 %.

- The uncertainty on the electron identification is 0.5 % in the central region ($z_{\mathrm{impact}} <$ 100 cm) and 2 % in the forward direction [14] ($z_{\mathrm{impact}} >$ 100 cm). This leads to a Q^2 dependent uncertainty on the jet cross sections, $\delta^{\mathrm{ID(e)}}$, of around 0.5 % for smaller values of Q^2 and up to 2 % in the highest Q^2 bin.

- The model uncertainty is estimated from the difference between the nominal result of the unfolding matrix and results obtained based on the migration matrices of either RAPGAP or DJANGOH. These differences are calculated using data, denoted as $\delta^{\mathrm{Model}}_{\mathrm{d,R}}$ and $\delta^{\mathrm{Model}}_{\mathrm{d,D}}$, as well as using pseudodata, denoted as $\delta^{\mathrm{Model}}_{\mathrm{p,R}}$ and $\delta^{\mathrm{Model}}_{\mathrm{p,D}}$. The model uncertainty on the cross sections is then calculated for each bin using

$$\delta^{\mathrm{Model}} = \pm\sqrt{\frac{1}{2}\left(\max\left(\delta^{\mathrm{Model}}_{\mathrm{d,R}}, \delta^{\mathrm{Model}}_{\mathrm{p,R}}\right)^2 + \max\left(\delta^{\mathrm{Model}}_{\mathrm{d,D}}, \delta^{\mathrm{Model}}_{\mathrm{p,D}}\right)^2\right)}\,. \tag{7}$$

  The sign is given by the difference with the largest modulus. The uncertainty due to the reweighting of the MC models is found to be negligible compared to the model uncertainty obtained in this way.

- The uncertainty due to the requirement on the z-coordinate of the primary event vertex is found to be negligible. This is achieved by a detailed simulation of the time dependent longitudinal and lateral profiles of the HERA beams.

- The uncertainty of the efficiency of the NC DIS trigger results in an overall uncertainty of the jet cross sections of $\delta^{\mathrm{Trig}} = 1.0\,\%$.

- The efficiency of the requirement of a link between the primary vertex, the electron track and the electron cluster in the LAr calorimeter is described by the simulation within 1 %, which is assigned as an overall track-cluster-link uncertainty, δ^{TrkCl}, on the jet cross sections [14].

- The overall normalisation uncertainty due to the luminosity measurement is $\delta^{\mathrm{Lumi}} = 2.5\,\%$ [23].

In case of the normalised jet cross sections all systematic uncertainties are varied simultaneously in the numerator and denominator. Consequently, all normalisation uncertainties, δ^{Lumi}, δ^{TrkCl} and δ^{Trig}, cancel fully. Uncertainties due to the electron reconstruction, such as $\delta^{E'_e}$, $\delta^{\mathrm{ID(e)}}$ and δ^{θ_e} cancel to a large extent, and uncertainties due to the reconstruction of the HFS cancel partially.

The relative size of the dominant experimental uncertainties δ^{stat}, δ^{JES} and δ^{Model} are displayed in figure 8 for the absolute jet cross sections. The jet energy scale δ^{JES} becomes relevant for the high-$P_{\mathrm{T}}^{\mathrm{jet}}$ region, since these jets tend to go more in the direction of the incoming proton and are thus mostly made up from calorimetric information. The model uncertainty is sizeable mostly in the high-$P_{\mathrm{T}}^{\mathrm{jet}}$ region.

5 Theoretical predictions

Theoretical pQCD predictions in NLO accuracy are compared to the measured cross sections. Hadronisation effects and effects of Z-exchange are not part of the pQCD predictions, and are therefore taken into account by correction factors.

5.1 NLO calculations

The parton level cross section σ_i^{parton} in each bin i is predicted in pQCD as a power-series in $\alpha_s(\mu_r)$, where μ_r is the renormalisation scale. The perturbative coefficients $c_{i,a,n}$ for a parton of flavour a in order n are convoluted in x with the parton density functions f_a of the proton,

$$\sigma_i^{\text{parton}} = \sum_{a,n} \alpha_s^n(\mu_r, \alpha_s(M_Z))\, c_{i,a,n}\left(x, \mu_r, \mu_f\right) \otimes f_a(x, \mu_f)\,. \tag{8}$$

The variable μ_f denotes the factorisation scale, and $\alpha_s(M_Z)$ is the value of the strong coupling constant at the mass of the Z-boson. The first non-vanishing contribution to σ_i^{parton} is of order α_s for inclusive jet and dijet cross sections and of order α_s^2 for trijet cross sections. The perturbative coefficients are currently known only to NLO.

The predictions σ_i^{parton} are obtained using the fastNLO framework [54, 55, 56] with perturbative coefficients calculated by the NLOJet++ program [57, 58]. The calculations are performed in NLO in the strong coupling and use the $\overline{\text{MS}}$-scheme with five massless quark flavours. The PDFs are accessed via the LHAPDF routines [59]. The MSTW2008 PDF set [60,61] is used, determined with a value of the strong coupling constant of $\alpha_s(M_Z) = 0.118$ [62]. The α_s-evolution is performed using the evolution routines as provided together with the PDF sets in LHAPDF. The running of the electromagnetic coupling $\alpha_{\text{em}}(Q)$ is calculated using a recent determination of the hadronic contribution $\Delta\alpha_{\text{had}}(M_Z^2) = 275.7(0.8) \times 10^{-4}$ [63]. The renormalisation and factorisation scales are chosen to be

$$\mu_r^2 = (Q^2 + P_{\text{T}}^2)/2 \;\text{ and }\; \mu_f^2 = Q^2\,. \tag{9}$$

The choice of μ_r is motivated by the presence of two hard scales in the process, whereas μ_f is chosen such that the same factorisation scale can be used in the calculation of jet and NC DIS cross sections. When choosing $\mu_r^2 = Q^2$ or $\mu_r^2 = P_T^2$ for the jet observables, the resulting changes in the cross section predictions are well covered by the theoretical uncertainty obtained from scale variations.

The calculation of the NC DIS cross sections, σ_i^{NC}, for the prediction of the normalised jet cross sections is performed using the QCDNUM program [64] in NLO in the zero mass variable flavour number scheme (ZM-VFNS). No contribution from Z-exchange is included, and both μ_f and μ_r are set to Q.

5.2 Hadronisation corrections

The NLO calculations at parton level have to be corrected for non-perturbative hadronisation effects. The hadronisation corrections c^{had} account for long-range effects in the cross section calculation such as the fragmentation of partons into hadrons. It is given by the ratio of the jet cross section on hadron level to the jet cross section on parton level, i.e. for each bin i $c_i^{\mathrm{had}} = \sigma_i^{\mathrm{hadron}}/\sigma_i^{\mathrm{parton}}$.

The jet cross sections on parton and hadron level are calculated using DJANGOH and RAPGAP. The parton level is obtained for MC event generators by selecting all partons before they are subjected to the fragmentation process. Reweighting the MC distributions of jet observables on parton level to those obtained from the NLO calculation has negligible impact on the hadronisation corrections. Hadronisation corrections are computed for both the k_{T} and the anti$-k_{\mathrm{T}}$ jet algorithm. They are very similar for inclusive jets and dijets, for trijets the corrections for anti$-k_{\mathrm{T}}$ tend to be somewhat smaller than for k_{T}.

The arithmetic average of c^{had} is used, obtained from the weighted DJANGOH and RAPGAP predictions (see section 3.1). Small differences of the correction factors between RAPGAP and DJANGOH, which both use the Lund string fragmentation model, are observed, due to the different modelling of the partonic final state. The values of c^{had} range from 0.8 to 1 and are given in the jet cross sections tables 8–27.

5.3 Electroweak corrections

Only virtual corrections for γ-exchange via the running of $\alpha_{\mathrm{em}}(\mu_r)$ are included in the pQCD calculations. The electroweak corrections c^{ew} account for the contributions from γZ-interference and Z-exchange. They are estimated using the LEPTO event generator, where cross sections can be calculated including these effects ($\sigma^{\gamma,Z}$) and excluding them (σ^{γ}). The electroweak correction factor c^{ew} is defined for each bin i by $c_i^{\mathrm{ew}} = \sigma_i^{\gamma,Z}/\sigma_i^{\gamma}$. It is close to unity at low Q^2 and becomes relevant for $Q^2 \to M_Z^2$, i.e. mainly in the highest Q^2 bin from $5000 < Q^2 < 15\,000\,\mathrm{GeV}^2$. In this bin the value of c^{ew} is around 1.1 for the luminosity-weighted sum of e^+p and e^-p data corresponding to the full HERA-II dataset. The electroweak correction has some P_{T}-dependence, which, however, turns out to be negligible for the recorded mixture of e^+p and e^-p data. In case of normalised jet cross sections, the electroweak corrections cancel almost completely such that they can be neglected. The electroweak corrections are well-known compared to the statistical precision of those data points where the corrections deviate from unity, and therefore no uncertainty on c^{ew} is assigned. The values of c^{ew} are given in the jet cross sections tables 8–17.

5.4 QCD predictions on hadron level

Given the parton level cross sections, $\sigma_i^{\mathrm{parton}}$, and the correction factors c_i^{had} and c_i^{ew} in bin i, the hadron level jet cross sections are calculated as

$$\sigma_i^{\mathrm{hadron}} = \sigma_i^{\mathrm{parton}}\, c_i^{\mathrm{had}}\, c_i^{\mathrm{ew}}\,, \tag{10}$$

while the predictions for the normalised jet cross sections are given by

$$\left(\frac{\sigma}{\sigma_{\mathrm{NC}}}\right)_i^{\mathrm{hadron}} = \frac{\sigma_i^{\mathrm{parton}}\, c_i^{\mathrm{had}}}{\sigma_i^{\mathrm{NC}}}\,. \tag{11}$$

5.5 Theoretical uncertainties

The following uncertainties on the NLO predictions are considered:

- The dominant theoretical uncertainty is attributed to the contribution from missing higher orders in the truncated perturbative expansion beyond NLO. These contributions are estimated by a simultaneous variation of the chosen scales for μ_r and μ_f by the conventional factors of 0.5 and 2. Typically, the resulting cross section varies monotonically in this interval. In a few cases when this does not hold, the minimum and maximum of the cross section in the interval is chosen to define the scale uncertainty. In case of normalised jet cross sections, the scales are varied simultaneously in the calculation of the numerator and denominator.
- The uncertainty on the hadronisation correction $\delta^{\rm had}$ is estimated using the SHERPA event generator [65,66]. Processes including parton scattering of $2 \to 5$ configurations are generated on tree level, providing a good description of jet production up to trijets, while NC DIS cross sections are not well described. Also the parton level distributions are in reasonable agreement with the NLO calculation. The partons are hadronised once with the Lund string fragmentation model and once with the cluster fragmentation model [67]. Half the difference between the two correction factors, derived from the two different fragmentation models, is taken as uncertainty on the hadronisation correction $\delta^{\rm had}$. It is between 1 to 2 % for the inclusive jet and dijet measurements and between 0.5 and 5 % for the trijet measurements. These uncertainties are included in the cross section tables. The absolute predictions from SHERPA, however, are considered to be unreliable due to mismatches between the parton shower algorithm and the PDFs [68]. Therefore, only ratios of SHERPA predictions are used for determining the uncertainty on the hadronisation corrections. The uncertainties obtained in this way are typically between 30 to 100 % larger than half the difference between the correction factors obtained using RAPGAP and DJANGOH.
- The uncertainty on the predictions due to the limited knowledge of the PDFs is determined at a confidence level of 68 % from the MSTW2008 eigenvectors, following the formula for asymmetric PDF uncertainties [69]. The PDF uncertainty is found to be almost symmetric with a size of about 1 % for all data points. Predictions using other PDF sets do not deviate by more than two standard deviations of the PDF uncertainty.

6 Experimental results

In the following the absolute and normalised double-differential jet cross sections are presented for inclusive jet, dijet, and trijet production using the $k_{\rm T}$ and the anti$-k_{\rm T}$ jet algorithms. The labelling of the bins in the tables of cross sections is explained in table 7.

An overview of the tables of jet cross sections is summarised in table 3 and of the tables of correlation coefficients, i.e. point-to-point statistical correlations, is provided in table 4. Figure 9 shows the correlation matrix of the inclusive, dijet and trijet cross sections, corresponding to tables 28–33. When looking at the inclusive jet, dijet or trijet cross sections alone, negative

Observable	k_T	anti−k_T	k_T (normalised)	anti−k_T (normalised)
$\sigma_{\text{jet}}(Q^2, P_T^{\text{jet}})$	table 8	table 13	table 18	table 23
$\sigma_{\text{dijet}}(Q^2, \langle P_T \rangle_2)$	table 9	table 14	table 19	table 24
$\sigma_{\text{dijet}}(Q^2, \xi_2)$	table 10	table 15	table 20	table 25
$\sigma_{\text{trijet}}(Q^2, \langle P_T \rangle_3)$	table 11	table 16	table 21	table 26
$\sigma_{\text{trijet}}(Q^2, \xi_3)$	table 12	table 17	table 22	table 27

Table 3: Overview of the tables of cross sections.

Observable	$\sigma_{\text{jet}}(Q^2, P_T^{\text{jet}})$	$\sigma_{\text{dijet}}(Q^2, \langle P_T \rangle_2)$	$\sigma_{\text{trijet}}(Q^2, \langle P_T \rangle_3)$	$\sigma_{\text{dijet}}(Q^2, \xi_2)$	$\sigma_{\text{trijet}}(Q^2, \xi_3)$
$\sigma_{\text{jet}}(Q^2, P_T^{\text{jet}})$	table 28	table 31	table 32	table 36	table 37
$\sigma_{\text{dijet}}(Q^2, \langle P_T \rangle_2)$	table 31	table 29	table 33	–	–
$\sigma_{\text{trijet}}(Q^2, \langle P_T \rangle_3)$	table 32	table 33	table 30	–	–
$\sigma_{\text{dijet}}(Q^2, \xi_2)$	table 36	–	–	table 34	table 38
$\sigma_{\text{trijet}}(Q^2, \xi_3)$	table 37	–	–	table 38	table 35

Table 4: Overview of the tables of correlation coefficients. The correlation coefficients between the $\langle P_T \rangle$ and ξ measurements are not available.

correlations down to −0.5 are observed between adjacent bins in P_T, which reflects the moderate jet resolution in P_T. In adjacent Q^2 bins, the negative correlations of about −0.1 are close to zero, due to the better resolution in Q^2. Sizeable positive correlations are observed between inclusive jet and dijet cross sections with the same Q^2 and similar P_T. Positive correlations between the trijet and the inclusive jet and dijet measurements are smaller than those between the dijet and inclusive jet, because of the smaller statistical overlap. Within the accuracy of this measurement, the correlation coefficients are very similar no matter whether the k_T or anti−k_T jet algorithm are used. Similarly, the statistical correlations of the normalised and the absolute cross sections are almost identical.

The measured cross sections for the k_T jet algorithm as a function of P_T (tables 8–10) are displayed in different Q^2 bins in figure 10, together with the NLO predictions described in section 5.4. A detailed comparison of the predictions to the measured cross sections is provided by the ratio of data to NLO in figure 11. The theory uncertainties from scale variations dominate over the sum of the experimental uncertainties in most bins.

The data are in general well described by the theoretical predictions. The predictions are slightly above the measured cross sections for inclusive jet and dijet production, at medium Q^2 and at high P_T. A detailed comparison of NLO predictions using different PDF sets with the measured jet cross sections is shown in figure 12. Only small differences are observed between predictions for different choices of PDF sets compared to the theory uncertainty from scale variations shown in figure 11. Predictions using the CT10 PDF set [70] are approximately 1 to 2 % below those using the MSTW2008 PDF set, and predictions using the NNPDF2.3 set [71] are about 2 % above the latter. The calculation using the HERAPDF1.5 set [72, 73, 74] is 2 % above the calculation using MSTW2008 at low P_T, while at the highest P_T values it is around 5 % below. The reason for this behaviour is the softer valence quark density at high x of the HERAPDF1.5 set compared to the other PDF sets. Predictions using the ABM11 PDF set [75] show larger differences compared to the other PDF sets.

The normalised cross sections using the k_T jet algorithm are displayed in figure 13 as a function of P_T in different Q^2 bins together with the NLO calculations. The ratio of data to the predictions is shown in figure 14. The comparison is qualitatively similar to the results from the absolute jet cross sections. Similar to the case of absolute cross sections, the theory uncertainty from scale variations is significantly larger than the total experimental uncertainty in almost all bins. For the normalised jet cross sections PDF dependencies do not cancel. This is due to the different x-dependencies and parton contributions to NC DIS compared to jet production. The systematic uncertainties are reduced for normalised cross sections compared to absolute jet cross section, since all normalisation uncertainties cancel fully, and uncertainties on the electron reconstruction and the HFS cancel partly. The experimental uncertainty is dominated by the statistical, the model and the jet energy scale uncertainties. Given the high experimental precision, in comparison to the absolute jet cross sections, one observes that the normalised dijet cross sections are below the theory predictions for many data points.

The measurements of absolute dijet and trijet cross sections are displayed in figure 15 as a function of ξ_2 and ξ_3 in different Q^2 bins, together with NLO predictions. The normalised jet cross sections are shown in figure 16. The ratio of absolute jet cross sections to NLO predictions as a function of ξ in bins of Q^2 is shown in figure 17. Good overall agreement between predictions and the data is observed. A similar level of agreement is obtained by using other PDF sets than the employed MSTW2008 set.

Also the anti$-k_T$ cross sections agree well with the theory predictions. For inclusive jets and dijets the NLO predictions using the anti$-k_T$ or the k_T jet algorithm are identical, for trijets they are not. The hadronisation corrections between anti$-k_T$ and k_T jets differ slightly. The anti$-k_T$ trijet cross sections have a tendency of being slightly lower than the k_T measurement.

Of the results presented here, those which can be compared to previous H1 measurements are found to be well compatible.

7 Determination of the strong coupling constant $\alpha_s(M_Z)$

The jet cross sections presented are used to determine the value of the strong coupling constant[3] α_s at the scale of the mass of the Z-boson, M_Z, in the framework of perturbative QCD. The value of the strong coupling constant α_s is determined in an iterative χ^2-minimisation procedure using NLO calculations, corrected for hadronisation effects and, if applicable, for electroweak effects. The sensitivity of the theory prediction to α_s arises from the perturbative expansion of the matrix elements in powers of $\alpha_s(\mu_r) = \alpha_s(\mu_r, \alpha_s(M_Z))$. For the α_s-fit, the evolution of $\alpha_s(\mu_r)$ is performed solving this equation numerically, using the renormalisation group equation in two-loop precision with five massless flavours.

[3] In this section, the strong coupling constant $\alpha_s(M_Z)$ is always quoted at the mass of the Z-boson, $M_Z = 91.1876\,\mathrm{GeV}$ [62]. For better readability the scale dependence is dropped in the notation and henceforth α_s is written for $\alpha_s(M_Z)$; '$\alpha_s(M_Z)$' is only used for explicit highlighting.

7.1 Fit strategy

The value of α_s is determined using a χ^2-minimisation, where α_s is a free parameter of the theory calculation. The agreement between theory and data is estimated using the χ^2definition [62,76]

$$\chi^2 = \vec{p}^{\mathrm{T}} \boldsymbol{V}^{-1} \vec{p} + \sum_k^{N_{\mathrm{sys}}} \varepsilon_k^2 \,, \tag{12}$$

where $\boldsymbol{V}^{-1}$ is the inverse of the covariance matrix with relative uncertainties. The element i of the vector $\vec{p}$ stands for the difference between the logarithm of the measurement m_i and the logarithm of the theory prediction $t_i = t_i(\alpha_s(M_Z))$:

$$p_i = \log m_i - \log t_i - \sum_k^{N_{\mathrm{sys}}} E_{i,k} \,. \tag{13}$$

This ansatz is equivalent to assuming that the m_i are log-normal distributed, with $E_{i,k}$ being defined as

$$E_{i,k} = \sqrt{f_k^{\mathrm{C}}} \left(\frac{\delta_{m,i}^{k,+} - \delta_{m,i}^{k,-}}{2} \varepsilon_k + \frac{\delta_{m,i}^{k,+} + \delta_{m,i}^{k,-}}{2} \varepsilon_k^2 \right) \,. \tag{14}$$

The nuisance parameters ε_k for each source of systematic uncertainty k are free parameters in the χ^2-minimisation. Sources indicated as uncorrelated between Q^2 bins in table 5 have several nuisance parameters, one for each Q^2 bin.

The parameters $\delta_{m,i}^{k,+}$ and $\delta_{m,i}^{k,-}$ denote the relative uncertainty on the measurement m_i, due to the 'up' and 'down' variation of the systematic uncertainty k. Systematic experimental uncertainties are treated in the fit as either relative correlated or uncorrelated uncertainties or as a mixture of both. The parameter f^{C} expresses the fraction of the uncertainty k which is considered as relative correlated uncertainty, and f^{U} expresses the fraction which is treated as uncorrelated uncertainty with $f^{\mathrm{C}} + f^{\mathrm{U}} = 1$. The symmetrised uncorrelated uncertainties squared $f_k^{\mathrm{U}}(\delta_{m,i}^{k,+} - \delta_{m,i}^{k,-})^2$ are added to the diagonal elements of the covariance matrix $\boldsymbol{V}$. The covariance matrix $\boldsymbol{V}$ thus consists of relative statistical uncertainties, including correlations between the data points of the measurements, correlated background uncertainties and the uncorrelated part of the systematic uncertainties.

7.2 Experimental uncertainties on α_s

The experimental uncertainties are treated in the fit as described in the following.

- The statistical uncertainties are accounted for by using the covariance matrix obtained from the unfolding process. It includes all point-to-point correlations due to statistical correlations and detector resolutions.
- The uncertainties due to the reconstruction of the hadronic final state, i.e. δ^{JES} and δ^{RCES}, are treated as 50 % correlated and uncorrelated, respectively.
- The uncertainty $\delta^{\mathrm{LArNoise}}$, due to the LAr noise suppression algorithm, is considered to be fully correlated.

Source of uncertainties k	Correlated fraction f^{C}	Uncorrelated fraction f^{U}	Uncorrelated between Q^2 bins
Jet energy scale δ^{JES}	0.5	0.5	
Rem. cluster energy scale δ^{RCES}	0.5	0.5	
LAr Noise $\delta^{\mathrm{LArNoise}}$	1	0	
Electron energy $\delta^{E'_e}$	1	0	✓
Electron polar angle δ^{θ_e}	1	0	✓
Electron ID $\delta^{\mathrm{ID(e)}}$	1	0	✓
Normalisation δ^{Norm}	1	0	
Model δ^{Model}	0.25	0.75	✓

Table 5: Split-up of systematic uncertainties in the fit of the strong coupling constant α_s.

- All uncertainties due to the reconstruction of the scattered electron ($\delta^{E'_e}$, δ^{θ_e} and $\delta^{\mathrm{ID(e)}}$) are treated as fully correlated for data points belonging to the same Q^2-bin and uncorrelated between different Q^2-bins.
- The uncertainties on the normalisation (δ^{Lumi}, δ^{Trig} and δ^{TrkCl}) are summed in quadrature to form the normalisation uncertainty $\delta^{\mathrm{Norm}} = 2.9\,\%$ which is treated as fully correlated.
- The model uncertainties are treated as 75 % uncorrelated, whereby the correlated fraction is treated as uncorrelated between different Q^2-bins.

The uncorrelated parts of the systematic uncertainties are expected to account for local variations, while the correlated parts are introduced to account for procedural uncertainties. A summary is given in table 5, showing the treatment of each experimental uncertainty in the fit.

Table 6 lists the size of the most relevant contributions to the experimental uncertainty on the α_s-value obtained. They are determined using linear error propagation applying an analogous formula as for the theoretical uncertainties (see equation 15). For α_s-values determined from the absolute jet cross sections, the dominant uncertainty is the normalisation uncertainty, since it is highly correlated with the value of $\alpha_s(M_Z)$ in the fit. The errors on the fit parameters, α_s and ε_k, are determined as the square root of the diagonal elements of the inverse of the Hessian matrix.

7.3 Theoretical uncertainties on α_s

Uncertainties on α_s from uncertainties on the theory predictions are often determined using the offset method [4]. In this analysis a different approach is taken. The theory uncertainties are determined for each source separately using linear error propagation [53]. Uncertainties on α_s originating from a specific source of theory uncertainty are calculated as:

$$\left(\Delta^{\mathrm{t}}_{\alpha_s}\right)^2 = f^{\mathrm{C}}\left(\sum_i^{N_{\mathrm{bins}}} \left.\frac{\partial\alpha_s}{\partial t_i}\right|_{\alpha_0} \Delta_{t_i}\right)^2 + f^{\mathrm{U}}\sum_i^{N_{\mathrm{bins}}}\left(\left.\frac{\partial\alpha_s}{\partial t_i}\right|_{\alpha_0} \Delta_{t_i}\right)^2 , \tag{15}$$

[4] In this procedure, parameters are changed one at a time, the fit is repeated and the difference with respect to the central fit result is calculated.

Measurement	$\Delta_{\alpha_s}^{\text{exp}}$	$\Delta_{\alpha_s}^{\text{Norm}}$	$\Delta_{\alpha_s}^{\text{RCES}}$	$\Delta_{\alpha_s}^{\text{JES}}$	$\Delta_{\alpha_s}^{\text{Model}}$
Experimental uncertainties on $\alpha_s \times 10^4$					
σ_{jet}	22.2	18.5	4.8	5.5	4.5
σ_{dijet}	23.4	19.4	4.4	4.3	6.4
σ_{trijet}	16.7	11.2	5.4	4.3	4.6
$\frac{\sigma_{\text{jet}}}{\sigma_{\text{NC}}}$	8.9	–	1.7	4.4	2.2
$\frac{\sigma_{\text{dijet}}}{\sigma_{\text{NC}}}$	9.9	–	1.6	3.3	3.6
$\frac{\sigma_{\text{trijet}}}{\sigma_{\text{NC}}}$	11.3	–	4.0	3.5	4.2
$[\sigma_{\text{jet}}, \sigma_{\text{dijet}}, \sigma_{\text{trijet}}]$	16.0	9.6	5.9	3.2	5.0
$\left[\frac{\sigma_{\text{jet}}}{\sigma_{\text{NC}}}, \frac{\sigma_{\text{dijet}}}{\sigma_{\text{NC}}}, \frac{\sigma_{\text{trijet}}}{\sigma_{\text{NC}}}\right]$	7.6	–	2.4	2.8	1.8

Table 6: The total experimental uncertainty on α_s from fits to different jet cross sections, and the contributions from the most relevant sources of uncertainties. These are the normalisation uncertainty, the uncertainties on the reconstruction of the HFS ($\Delta_{\alpha_s}^{\text{RCES}}$ and $\Delta_{\alpha_s}^{\text{JES}}$) and the model uncertainty.

where t_i is the prediction in bin i, Δ_{t_i} is the uncertainty of the theory in bin i and f^{C} (f^{U}) are the correlated (uncorrelated) fractions of the uncertainty source under investigation. The partial derivatives are calculated numerically at the α_s-value, α_0, obtained from the fit. The uncertainties on α_s obtained this way are found to be of comparable size as the uncertainties obtained with other methods, like the offset method [11, 77]. Because equation 15 is linear, the theory uncertainties are symmetric and can be interpreted as one standard deviation confidence intervals.

Theoretical uncertainties in the determination of α_s arise from unknown higher order corrections beyond NLO, from uncertainties on the hadronisation corrections and from uncertainties on the PDFs. Three distinct sources of uncertainties from the PDFs are considered. These are uncertainties due to the limited precision of the input data in the determination of the PDFs, the uncertainty of the value of $\alpha_s(M_Z)$, which was used for obtaining the PDFs, and procedural uncertainties in the PDF fit. Details for all theoretical uncertainties considered are given below.

- **Uncertainties resulting from truncation of the perturbative series:** The uncertainty due to missing higher orders is conventionally determined by a variation of μ_r and μ_f. In order to obtain conservative estimates from equation 15, the uncertainty from scale variations on the theory predictions is defined by [78]

$$\Delta_{t_i}^{\mu} := \max\left(\left|t_i(\mu = c_\mu \mu_0) - t_i(\mu = \mu_0)\right|\right)_{0.5 \le c_\mu \le 2}, \tag{16}$$

using a continuous variation of the scale in the interval $0.5 \le c_\mu \le 2$. The uncertainty from scale variations on α_s, $\Delta_{\alpha_s}^{\mu}$, is then given by equation 15 using $\Delta_{t_i}^{\mu}$. Possible higher order contributions may change both the normalisation and the shape of the cross section predictions. While the former effect has to be taken as correlated uncertainty, the latter will result in uncorrelated uncertainties. Since the size of the effect of these two kinds of uncertainties cannot be estimated the correlated und uncorrelated fractions of $\Delta^{\mu}_{t_i}$ are assumed to be 0.5 each. In case of normalised jet cross sections, the uncertainty $\Delta^{\mu}_{t_i}$ is determined by a simultaneous variation of the scales in the numerator and denominator. The scale dependence of the inclusive NC DIS calculation is small compared to the scale dependence of the jet cross sections, since it is in LO of $O(\alpha_s^0(\mu_r))$. Changing the renormalisation scale for the jet cross sections to $\mu_r = Q$ or $\mu_r = P_T$ results in changes in $\alpha_s(M_Z)$ which are typically of similar size as the experimental uncertainty and always smaller than the renormalisation scale uncertainty. The uncertainty from the variation of the renormalisation scale is by far the largest uncertainty of all theoretical and experimental uncertainties considered. Calculations beyond NLO are therefore mandatory for a more precise determination of α_s from jet cross sections in DIS.

- **Hadronisation uncertainties:** The uncertainties of the hadronisation correction $\Delta^{\rm had}_t$ on the theory predictions are obtained using half the difference of the hadronisation corrections calculated with the Lund string model and the cluster fragmentation model (see section 5.5). The resulting uncertainties on α_s are determined using the linear error propagation described above. The uncertainty is taken to be half correlated and half uncorrelated.

- **PDF uncertainty:** PDF uncertainties on α_s, $\Delta^{\rm PDF}_{\alpha_s}$ are estimated by propagating the uncertainty eigenvectors of the MSTW2008 PDF set. Details are described in [53].

- **Uncertainty due to the limited precision of $\alpha_s(M_Z)$ in the PDF fit:** The PDFs depend on the $\alpha_s(M_Z)$ value used for their determination. This leads to an additional uncertainty on the PDFs and thus to an additional uncertainty on the α_s-value extracted from the jet cross sections. This uncertainty, $\Delta^{\rm PDF(\alpha_s)}_{\alpha_s}$, is conventionally defined as a variation of ± 0.002 around the nominal value of $\alpha_s(M_Z) = 0.118$ (see e.g. [79]). For the full range of available MSTW2008 PDF sets with different fixed values of $\alpha_s(M_Z)$, the resulting values of α_s from fits to jet data are displayed in figure 18. While some dependence on the value of $\alpha_s(M_Z)$ used in the PDF fit is observed for the α_s values obtained from inclusive jet and dijet cross sections, the α_s-value obtained from the trijet cross sections shows only a very weak dependence on $\alpha_s(M_Z)$. This is due to the high sensitivity of the trijet cross sections to α_s, where the calculation is of $O(\alpha_s^2)$ already at LO. Consequently, due to the inclusion of the trijet cross sections, the dependence on $\alpha_s(M_Z)$ as used in the PDF fit is reduced for the fit to the multijet dataset.

- **Procedural and theory uncertainties on the PDFs:** In order to estimate the uncertainty due to the procedure used to extract PDFs, all α_s fits are repeated using PDF sets from different groups. The α_s-values obtained are displayed in figure 19 and are listed in table 39. Half the difference between the α_s-values obtained using the NNPDF2.3 and CT10 PDF sets is assigned as PDF set uncertainty, $\Delta^{\rm PDFset}_{\alpha_s}$. The values for $\Delta^{\rm PDFset}_{\alpha_s}$ are in the range from 0.0007 to 0.0012.

7.4 Results of the α_s-fit

The strong coupling constant is determined from each of the jet measurements, i.e. from the absolute and normalised inclusive jet, dijet and trijet cross sections as a function of Q^2 and

P_{T}, as well as from the three absolute and three normalised jet cross sections simultaneously. The statistical correlations (tables 28–33) are taken into account. The α_s-values obtained from measurements using the k_{T} jet algorithm are compared to those using the anti$-k_{\mathrm{T}}$ jet algorithm with the corresponding NLO calculations.

The NLO correction to the LO cross section is below 50 % for all of the data points and below 30 % for 64 % of the data points. It is assumed that the perturbative series is converging sufficiently fast, such that NLO calculations are applicable, and that the uncertainty from the variation of the renormalisation and factorisation scales accounts for the not yet calculated contributions beyond NLO.

The α_s results, determined from fits to the individual absolute and normalised jet cross sections as well as to the absolute and normalised multijet cross sections using either the k_{T} or the anti$-k_{\mathrm{T}}$ jet algorithms, are summarised in table 40, together with the split-up of the contributions to the theoretical uncertainty. The largest contribution is due to the variation of the renormalisation scale. The fits yield, for the k_{T}-jets taken as an example, the following values of χ^2/n_{dof} for the absolute (normalised) inclusive jet, dijet and trijet measurements, 24.8/23 (26.8/23), 25.1/23 (31.0/23) and 13.6/15 (11.8/15), respectively. For the absolute (normalised) multijet measurements the value of 75.2/63 (89.8/63) is obtained. Note that the theoretical uncertainties on α_s are not considered in the calculation of χ^2/n_{dof}. The fact that χ^2/n_{dof} degrades as more data are included (multijets as compared to individual data sets) or as the experimental precision is improved (normalised as compared to absolute cross sections) indicates a problem with the theory, possibly related to higher order corrections. Similarly, the fact that α_s extracted from the dijet data is below the values obtained from inclusive jet or trijet data may be due to unknown higher order effects.

All α_s-values extracted are compatible within the theoretical uncertainty obtained by the scale variations. The values of α_s extracted using k_{T} or anti$-k_{\mathrm{T}}$ jet cross sections are quite consistent. Among the absolute cross sections, not considering the multijet fit, the trijet data yield values of α_s with the highest experimental precision, because the LO trijet cross section is proportional to α_s^2, whereas the inclusive or dijet cross section at LO are proportional to α_s only.

The best experimental precision on α_s is achieved for normalised jet cross sections, due to the full cancellation of all normalisation uncertainties, which are highly correlated with the value of $\alpha_s(M_Z)$ in the fit. A breakdown of the individual uncertainties contributing to the total experimental uncertainty is given in table 6. For the α_s extraction using absolute cross sections, the normalisation uncertainty is the dominant uncertainty. The jet energy scale, the remaining cluster energy scale and the model uncertainty contribute with similar size to the experimental uncertainty. All other experimental uncertainties are negligible with respect to these uncertainties. The uncertainties from scale variations are somewhat reduced for normalised jet cross sections, due to the simultaneous variation of the scales in the numerator and the denominator. The uncertainties from PDFs are of similar size when comparing absolute and normalised jet cross sections. The residual differences are well understood [53].

The absolute and normalised dijet cross sections yield a significantly smaller value of α_s than the corresponding values from inclusive jet cross sections, considering the experimental uncertainty only. This is attributed to missing higher order contributions in the calculations, which may be different in the inclusive jet phase space region which is not part of the dijet phase space.

These are, for instance, the dijet topologies with $M_{12} < 16\,\mathrm{GeV}$, or events where one jet is outside the acceptance in $\eta^{\mathrm{jet}}_{\mathrm{lab}}$. In order to test the influence of the phase space, an inclusive jet measurement is performed in the phase space of the dijet measurement, i.e. with the requirement of two jets, $M_{12} > 16\,\mathrm{GeV}$ and $7 < \langle P_{\mathrm{T}}\rangle_2 < 50\,\mathrm{GeV}$. When using the identical scale $\mu_r^2 = Q^2$ for the α_s-fit to this inclusive jet and the dijet measurement, the difference in α_s is only 0.0003. With the nominal scales, $\mu_r^2 = (Q^2 + (P_{\mathrm{T}}^{\mathrm{jet}})^2)/2$ for this inclusive jet measurement and $\mu_r^2 = (Q^2 + (\langle P_{\mathrm{T}}\rangle_2)^2)/2$ for the dijet measurement, the difference in α_s increases to 0.0007. Since the α_s values obtained are rather similar, this lends some support to the argument given above.

The best experimental precision on α_s is obtained from a fit to normalised multijet cross sections, yielding:

$$\begin{aligned} \alpha_s(M_Z)|_{k_{\mathrm{T}}} &= 0.1165\ (8)_{\mathrm{exp}}\ (5)_{\mathrm{PDF}}\ (7)_{\mathrm{PDFset}}\ (3)_{\mathrm{PDF}(\alpha_s)}\ (8)_{\mathrm{had}}\ (36)_{\mu_r}\ (5)_{\mu_f} \\ &= 0.1165\ (8)_{\mathrm{exp}}\ (38)_{\mathrm{pdf,theo}}\ . \end{aligned} \tag{17}$$

Here, we quote the value obtained for jets reconstructed with the k_{T} algorithm. As can be seen in table 40, it is fully consistent with the α_s-value found for jets using the anti$-k_{\mathrm{T}}$ algorithm.

The uncertainties on $\alpha_s(M_Z)$ are dominated by theory uncertainties from missing higher orders and allow a determination of $\alpha_s(M_Z)$ with a precision of 3.4 % only, while an experimental precision of 0.7 % is reached. When assuming the theory uncertainties on the cross section predictions to be fully correlated or when using the offset method to estimate these uncertainties, the resulting uncertainty on $\alpha_s(M_Z)$ is about 30% larger. Complete next-to-next-to-leading order calculations of jet production in DIS are required to reduce this mismatch in precision between experiment and theory.

The α_s-values determined are compatible with the world average [62, 80] value of $\alpha_s(M_Z) = 0.1185\ (6)$ within the experimental and particularly the theoretical uncertainties. The α_s-values extracted from the k_{T}-jet cross sections are compared to the world average value in figure 20.

The value of $\alpha_s(M_Z)$ with the highest overall precision is obtained from fits to a reduced phase space region, in which the dominant theoretical uncertainty, estimated from variations of the renormalisation and factorisation scales, are reduced at the expense of an increased experimental uncertainty. For photon virtualities of $Q^2 > 400\,\mathrm{GeV}^2$ a total uncertainty of 2.9 % on the α_s-value is obtained, with a value of

$$\alpha_s(M_Z)|_{k_{\mathrm{T}}} = 0.1160\ (11)_{\mathrm{exp}}\ (32)_{\mathrm{pdf,theo}}\ .$$

The value of $\alpha_s(M_Z)$ is the most precise value ever derived at NLO from jet data recorded in a single experiment.

The running of $\alpha_s(\mu_r)$ is determined from five fits using the normalised multijet cross sections, each based on a set of measurements with comparable values of the renormalisation scale μ_r. The values of $\alpha_s(M_Z)$ and $\alpha_s(\mu_r)$ extracted are listed in table 41 together with the cross section weighted average values of μ_r. The values of $\alpha_s(\mu_r)$ are obtained from the values of $\alpha_s(M_Z)$ by applying the 2-loop solution for the evolution equation of $\alpha_s(\mu_r)$. The values of $\alpha_s(M_Z)$ and $\alpha_s(\mu_r)$ obtained from the k_{T}-jets are displayed in figure 21 together with results from other recent and precise jet data[5] [10, 82, 83, 84, 85, 86]. Within the small experimental uncertainties the

[5]The values $\alpha_s(\mu_r)$ given in [82, 83, 84, 86] are evolved to $\alpha_s(M_Z)$ for this comparison, whereas the values of both $\alpha_s(\mu_r)$ and $\alpha_s(M_Z)$ are given in [85].

values of $\alpha_s(M_Z)$ of the present analysis are consistent and independent of μ_r. Good agreement is found with H1 data [10] at low scales and other jet data [82,83,84,85,86] at medium and high scales. The prediction for the running of $\alpha_s(\mu_r)$ using $\alpha_s(M_Z) = 0.1165\ (8)_{\rm exp}\ (38)_{\rm pdf,theo}$, as extracted from the normalised multijet cross sections, is also shown in figure 21, together with its experimental and total uncertainty. The prediction is in good agreement with the measured values of $\alpha_s(\mu_r)$.

8 Summary

Measurements of inclusive jet, dijet and trijet cross sections in the Breit frame in deep-inelastic electron-proton scattering in the kinematical range $150 < Q^2 < 15\,000\,\mathrm{GeV}^2$ and $0.2 < y < 0.7$ are presented, using H1 data corresponding to an integrated luminosity of $351\,\mathrm{pb}^{-1}$. The measurements consist of absolute jet cross sections as well as jet cross sections normalised to the neutral current DIS cross sections. Jets are determined using the $k_{\rm T}$ and the anti$-k_{\rm T}$ jet algorithm. Compared to previous jet measurements by H1, this analysis makes use of an improved electron calibration and further development of the energy flow algorithm, which combines information from tracking and calorimetric measurements, by including a better separation of electromagnetic and hadronic components of showers. The sum of these improvements, together with a new method to calibrate the hadronic final state, reduces the hadronic energy scale uncertainty by a factor of two to 1 % for $P_{\rm T,lab}^{\rm jet}$ down to 5 GeV.

The jet cross section measurements are performed using a regularised unfolding procedure to correct the neutral current DIS, the inclusive jet, the dijet and the trijet measurements simultaneously for detector effects. It considers up to seven different observables per measurement for the description of kinematical migrations due to the limited detector resolution. This approach provides a reliable treatment of migration effects and enables the determination of the statistical correlations between the three jet measurements and the neutral current DIS measurement.

Theoretical QCD calculations at NLO, corrected for hadronisation and electroweak effects, provide a good description of the measured double-differential jet cross sections as a function of the exchanged boson virtuality Q^2, the jet transverse momentum $P_{\rm T}^{\rm jet}$, the mean transverse momentum $\langle P_{\rm T}\rangle_2$ and $\langle P_{\rm T}\rangle_3$ in case of dijets and trijets, as well as of the longitudinal proton momentum fractions ξ_2 and ξ_3. In general, the precision of the data is considerably better than that of the NLO calculations.

The measurements of the inclusive, the dijet and the trijet cross section are used separately and also simultaneously to extract values for the strong coupling constant $\alpha_s(M_Z)$. The best experimental precision of 0.7 % is obtained when using the normalised multijet cross sections. The simultaneous extraction of the strong coupling constant $\alpha_s(M_Z)$ from the normalised inclusive jet, the dijet and the trijet samples using the $k_{\rm T}$ jet algorithm yields:

$$\begin{aligned} \alpha_s(M_Z)|_{k_{\rm T}} &= 0.1165\ (8)_{\rm exp}\ (5)_{\rm PDF}\ (7)_{\rm PDFset}\ (3)_{\rm PDF(\alpha_s)}\ (8)_{\rm had}\ (36)_{\mu_r}\ (5)_{\mu_f} \\ &= 0.1165\ (8)_{\rm exp}\ (38)_{\rm pdf,theo}\ . \end{aligned} \tag{18}$$

A very similar result is obtained when using the anti$-k_{\rm T}$ jet algorithm. The values and uncertainties of $\alpha_s(M_Z)$ obtained using absolute jet cross sections are consistent with the results from the corresponding normalised jet cross sections, albeit with larger experimental uncertainties. A tension is observed between the value of $\alpha_s(M_Z)$ extracted from the dijet sample and the similar values obtained from the inclusive jet and the trijet samples. This may be caused by missing higher orders in the calculations, which can be different in the inclusive jet phase space region which is not part of the dijet phase space.

When restricting the measurement to regions of higher Q^2, where the scale uncertainties are reduced, the smallest total uncertainty on the extracted $\alpha_s(M_Z)$ is found for $Q^2 > 400\,\mathrm{GeV}^2$. For this region the loss in experimental precision is compensated by the reduced theory uncertainty, yielding

$$\alpha_s(M_Z)|_{k_\mathrm{T}} = 0.1160\ (11)_{\mathrm{exp}}\ (32)_{\mathrm{pdf,theo}}\ .$$

The extracted $\alpha_s(M_Z)$-values are compatible within uncertainties with the world average value of $\alpha_s(M_Z) = 0.1185\ (6)$ and with α_s-values from other jet data. Calculations in NNLO are needed to benefit from the superior experimental precision of the DIS jet data.

The running of $\alpha_s(\mu_r)$, determined from the normalised multijet cross sections, is shown to be consistent with the expectation from the renormalisation group equation and with values of $\alpha_s(\mu_r)$ from other jet measurements.

Acknowledgements

We are grateful to the HERA machine group whose outstanding efforts have made this experiment possible. We thank the engineers and technicians for their work in constructing and maintaining the H1 detector, our funding agencies for financial support, the DESY technical staff for continual assistance and the DESY directorate for support and for the hospitality which they extend to the non DESY members of the collaboration. We would like to give credit to all partners contributing to the EGI computing infrastructure for their support for the H1 Collaboration. Furthermore, we thank Zoltán Nagy and Stefan Höche for fruitful discussions and for help with their computer programs.

References

[1] H. Fritzsch and M. Gell-Mann, Proceedings of "16th Int. Conference on High-Energy Physics", Batavia IL, 1972, 135, [arXiv:hep-ph/0208010].

[2] D. Gross and F. Wilczek, Phys. Rev. Lett. **30** (1973) 1343.

[3] H. Politzer, Phys. Rev. Lett. **30** (1973) 1346.

[4] A. Ali and G. Kramer, Eur. Phys. J. **H 36** (2011) 245, [arXiv:1012.2288], and references therein.

[5] T. Schörner-Sadenius, Eur. Phys. J. C **72** (2012) 2060, Erratum ibid, 72 (2012) 2133.

[6] R. Feynman, *Photon – Hadron Interactions*. Benjamin, New York, 1972.

[7] K. Streng, T. Walsh, and P. Zerwas, Z. Phys. **C 2** (1979) 237.

[8] ZEUS Collaboration, H. Abramowicz *et al.*, Eur. Phys. J. C **70** (2010) 965, [arXiv:1010.6167].

[9] ZEUS Collaboration, H. Abramowicz *et al.*, Phys. Lett. B **691** (2010) 127, [arXiv:1003.2923].

[10] H1 Collaboration, F. D. Aaron *et al.*, Eur. Phys. J. C **67** (2010) 1, [arXiv:0911.5678].

[11] H1 Collaboration, F. D. Aaron *et al.*, Eur. Phys. J. C **65** (2010) 363, [arXiv:0904.3870].

[12] S. Ellis and D. Soper, Phys. Rev. D **48** (1993) 3160, [hep-ph/9305266].

[13] M. Cacciari, G. P. Salam, and G. Soyez, JHEP **0804** (2008) 063, [arXiv:0802.1189].

[14] R. Kogler, *Measurement of jet production in deep-inelastic ep scattering at HERA*. Dissertation, Universität Hamburg, DESY-THESIS-2011-003, MPP-2010-175, 2010. Available at `http://www-h1.desy.de/publications/theses_list.html`.

[15] H1 Collaboration, I. Abt *et al.*, Nucl. Instr. and Meth. A **386** (1997) 310.

[16] H1 Collaboration, I. Abt *et al.*, Nucl. Instr. and Meth. A **386** (1997) 348.

[17] Calorimeter Group of H1, B. Andrieu *et al.*, Nucl. Instr. and Meth. A **336** (1993) 460.

[18] Calorimeter Group of H1, B. Andrieu *et al.*, Nucl. Instr. and Meth. A **350** (1994) 57.

[19] Calorimeter Group of H1, B. Andrieu *et al.*, Nucl. Instr. and Meth. A **336** (1993) 499.

[20] SPACAL Group of H1, R. Appuhn *et al.*, Nucl. Instr. and Meth. A **386** (1997) 397.

[21] SPACAL Group of H1, R. Appuhn *et al.*, Nucl. Instr. and Meth. A **382** (1996) 395.

[22] D. Pitzl *et al.*, Nucl. Instr. and Meth. A **454** (2000) 334, [hep-ex/0002044].

[23] H1 Collaboration, F. D. Aaron *et al.*, Eur. Phys. J. C **72** (2012) 2163, [arXiv:1205.2448] Erratum ibid, 74 (2014) 2733.

[24] M. Peez, *Search for deviations from the standard model in high transverse energy processes at the electron proton collider HERA (in French)*. Dissertation, Univ. Claude Bernard, Lyon, DESY-THESIS-2003-023, CPPM-T-2003-04, 2003. Available at `http://www-h1.desy.de/publications/theses_list.html`.

[25] S. Hellwig, *Investigation of the $D^* - \pi_{slow}$ double tagging method for the analysis of charm (in German*. Diploma thesis, Hamburg University, 2004. Available at `http://www-h1.desy.de/publications/theses_list.html`.

[26] B. Portheault, *First measurement of charged and neutral current cross sections with the polarized positron beam at HERA II and QCD-electroweak analyses (in French)*. Dissertation, Univ. Paris XI Orsay, LAL-05-05, 2005. Available at `http://www-h1.desy.de/publications/theses_list.html`.

[27] M. Feindt, physics/0402093.

[28] M. Feindt and U. Kerzel, Nucl. Instr. and Meth. A **559** (2006) 190.

[29] S. Bentvelsen, J. Engelen, and P. Kooijman, Proceedings of "Physics at HERA", eds. Buchmüller and G. Ingelman, DESY, Hamburg, vol. 1, 1992, 23 NIKHEF-H-92-02.

[30] K. C. Hoeger, Proceedings of "Physics at HERA", eds. Buchmüller and G. Ingelman, DESY, Hamburg, vol. 1, 1992, 43.

[31] H1 Collaboration, C. Adloff *et al.*, Eur. Phys. J. C **30** (2003) 1, [hep-ex/0304003].

[32] H1 Collaboration, F. D. Aaron *et al.*, JHEP **1209** (2012) 061, [arXiv:1206.7007].

[33] U. Bassler and G. Bernardi, Nucl. Instr. and Meth. A **361** (1995) 197, [hep-ex/9412004].

[34] U. Bassler and G. Bernardi, Nucl. Instr. and Meth. A **426** (1999) 583, [hep-ex/9801017].

[35] M. Wobisch, *Measurement and QCD Analysis of Jet Cross Sections in Deep-Inelastic Positron-Proton Collisions at* $\sqrt{s} = 300\ GeV$. Dissertation, RWTH Aachen, DESY-THESIS-2000-049, 2000. Available at `http://www-h1.desy.de/publications/theses_list.html`.

[36] M. Cacciari and G. P. Salam, Phys. Lett. B **641** (2006) 57, [hep-ph/0512210].

[37] ZEUS Collaboration, S. Chekanov *et al.*, Phys. Lett. B **649** (2007) 12, [hep-ex/0701039].

[38] S. Frixione and G. Ridolfi, Nucl. Phys. B **507** (1997) 315.

[39] M. Gouzevitch, *Measurement of the strong coupling constant* α_s *with jets in deep-inelastic scattering (in French)*. Dissertation, Ecole Polytechnique Palaiseau, DESY-THESIS-2008-047, 2008. Available at `http://www-h1.desy.de/publications/theses_list.html`.

[40] R. Brun *et al.*, CERN-DD/EE 84-1(1987) .

[41] J. Pumplin, D. Stump, J. Huston, H. Lai, P. M. Nadolsky, *et al.*, JHEP **0207** (2002) 012, [hep-ph/0201195].

[42] K. Charchula, G. A. Schuler, and H. Spiesberger, DJANGOH 1.4. Comput. Phys. Commun. **81** (1994) 381.

[43] L. Lönnblad, ARIADNE 4.10, Comput. Phys. Commun. **71** (1992) 15.

[44] L. Lönnblad, Manual, Oct. 2001, available at `http://home.thep.lu.se/~leif/ariadne/ariadne.pdf`.

[45] H. Jung, RAPGAP 3.1, Comput. Phys. Commun. **86** (1995) 147.

[46] H. Jung, Manual, Aug. 2006, available at `http://www.desy.de/~jung/rapgap/rapgap-desy.html` .

[47] B. Andersson *et al.*, Physics Reports **97** (1983) 31.

[48] T. Sjöstrand, arXiv:hep-ph/9508391.

[49] ALEPH Collaboration, S. Schael *et al.*, Phys. Lett. B **606** (2005) 265.

[50] A. Kwiatkowski, H. J. Spiesberger, and H. J. Möhring, Comput. Phys. Commun. **69** (1992) 155.

[51] G. Ingelman, A. Edin, and J. Rathsman, Comput. Phys. Commun. **101** (1997) 108, [arXiv:hep-ph/9605286].

[52] S. Schmitt, JINST **7** (2012) T10003, [arXiv:1205.6201].

[53] D. Britzger, *Regularized unfolding of jet cross sections in deep-inelastic ep scattering at HERA and determination of the strong coupling constant*. Dissertation, Universität Hamburg, DESY-THESIS-2013-045, 2013. Available at `http://www-h1.desy.de/publications/theses_list.html`.

[54] H1 Collaboration, C. Adloff *et al.* Eur. Phys. J. C **19** (2001) 289, [hep-ex/0010054]

[55] T. Kluge, K. Rabbertz, and M. Wobisch, Proceedings of "14th International Workshop on Deep Inelastic Scattering (DIS 2006)", eds. M. Kuze, K. Nagano and K. Tokushuku, Tsukuba, Japan, 2007, 483, [hep-ph/0609285].

[56] D. Britzger, K. Rabbertz, F. Stober, and M. Wobisch, Proceedings of "20th International Workshop on Deep-Inelastic Scattering and Related Subjects (DIS 2012)", ed. I. Brock, Bonn, Germany, 2013, 217, [arXiv:1208.3641].

[57] Z. Nagy and Z. Trocsanyi, Phys. Rev. D **59** (1999) 014020, [hep-ph/9806317] Erratum ibid, 62 (2000) 099902.

[58] Z. Nagy and Z. Trocsanyi, Phys. Rev. Lett. **87** (2001) 082001, [hep-ph/0104315].

[59] M. Whalley, D. Bourilkov, and R. Group, Proceedings for "HERA and the LHC", eds. A. De Roeck and H. Jung, Hamburg, Germany, 2005, 575, [hep-ph/0508110].

[60] A. Martin, W. Stirling, R. Thorne, and G. Watt, Eur. Phys. J. C **63** (2009) 189, [arXiv:0901.0002].

[61] A. Martin, W. Stirling, R. Thorne, and G. Watt, Eur. Phys. J. C **64** (2009) 653, [arXiv:0905.3531].

[62] Particle Data Group, J. Beringer *et al.*, Phys. Rev. D **86** (2012) 010001 and 2013 partial update for the 2014 edition.

[63] S. Bodenstein, C. A. Dominguez, K. Schilcher, and H. Spiesberger, Phys. Rev. D **86** (2012) 093013, [arXiv:1209.4802].

[64] M. Botje, Comput. Phys. Commun. **182** (2011) 490, [arXiv:1005.1481].

[65] T. Gleisberg *et al.*, SHERPA 1.3.1, JHEP **0902** (2009) 007, [arXiv:0811.4622].

[66] T. Carli, T. Gehrmann, S. Hoeche, Eur. Phys. J. C **67** (2010) 73,[arXiv:0912.3715]

[67] B. Webber, Nucl. Phys. B **238** (1984) 492.

[68] J. C. Collins and X.-M. Zu, JHEP **0206** (2002) 018, [hep-ph/0204127].

[69] J. M. Campbell, J. W. Huston, and W. J. Stirling, Rept. Prog. Phys. **70** (2007) 89, [arXiv:hep-ph/0611148].

[70] H.-L. Lai *et al.*, Phys. Rev. D **82** (2010) 074024, [arXiv:1007.2241].

[71] R. D. Ball *et al.*, Nucl. Phys. B **867** (2013) 244, [arXiv:1207.1303].

[72] H1 and ZEUS Collaborations, F. D. Aaron *et al.*, JHEP **1001** (2010) 109, [arXiv:0911.0884].

[73] H1 and ZEUS Collaborations, *PDF fits including HERA-II high Q^2 data (HERAPDF1.5)*, Preliminary result, H1prelim-10-142, ZEUS-prel-10-018, 2010. See http://www-h1.desy.de/publications/H1preliminary.short_list.html.

[74] H1 and ZEUS Collaborations, V. Radescu, Proceedings of "35th International Conference on High Energy Physics (ICHEP 2010)", eds. B. Pire *et al.*, Paris, France, 2010, 168, [arXiv:1308.0374].

[75] S. Alekhin, J. Blümlein, and S. Moch, Phys. Rev. D **86** (2012) 054009, [arXiv:1202.2281].

[76] V. Barone, C. Pascaud, and F. Zomer, Eur. Phys. J. C **12** (2000) 243, [hep-ph/9907512].

[77] H1 Collaboration, A. Aktas *et al.*, Phys. Lett. B **653** (2007) 134, [arXiv:0706.3722].

[78] D. E. Soper, hep-ph/9702203.

[79] H1 and ZEUS Collaborations, H. Abramowicz *et al.*, Eur. Phys. J. C **73** (2013) 2311, [arXiv:1211.1182].

[80] S. Bethke, Nucl. Phys. Proc. Suppl. **234** (2013) 229, [arXiv:1210.0325].

[81] ZEUS Collaboration, H. Abramowicz *et al.*, Nucl. Phys. B **864** (2012) 1, [arXiv:1205.6153].

[82] G. Dissertori, A. Gehrmann-De Ridder, T. Gehrmann, E. W. N. Glover, G. Heinrich and H. Stenzel, JHEP **0802** (2008) 040, [arXiv:0712.0327].

[83] JADE Collaboration, J. Schieck *et al.*, , Eur. Phys. J. C **48** (2006) 3 [Erratum-ibid. C **50** (2007) 769] [arXiv:0707.0392].

[84] OPAL Collaboration, G. Abbiendi *et al.*, Eur. Phys. J. C **71** (2011) 1733 [arXiv:1101.1470].

[85] CMS Collaboration, S. Chatrchyan *et al.*, Eur. Phys. J. C **73** (2013) 2604, [arXiv:1304.7498].

[86] D0 Collaboration, V. Abazov *et al.*, Phys. Lett. B **718** (2012) 56, [arXiv:1207.4957].

Bin labels P_T

Label	P_T range in GeV
α	$7 \leq P_T < 11$
β	$11 \leq P_T < 18$
γ	$18 \leq P_T < 30$
δ	$30 \leq P_T < 50$

Bin labels Q^2

Bin number q	Q^2 range in GeV^2
1	$150 \leq Q^2 < 200$
2	$200 \leq Q^2 < 270$
3	$270 \leq Q^2 < 400$
4	$400 \leq Q^2 < 700$
5	$700 \leq Q^2 < 5000$
6	$5000 \leq Q^2 < 15\,000$

Bin labels ξ_2 dijet

Label	ξ_2 range
a	$0.006 \leq \xi_2 < 0.02$
b	$0.02 \leq \xi_2 < 0.04$
c	$0.04 \leq \xi_2 < 0.08$
d	$0.08 \leq \xi_2 < 0.316$

Bin labels ξ_3 trijet

Label	ξ_3 range
A	$0.01 \leq \xi_3 < 0.04$
B	$0.04 \leq \xi_3 < 0.08$
C	$0.08 \leq \xi_3 < 0.5$

Table 7: Bin numbering scheme for Q^2, P_T, and ξ-bins. Bins of the double-differential measurements are for instance referred to as 3γ for the bin in the range $270 < Q^2 < 400\,\mathrm{GeV}^2$ and $18 < P_T^{\mathrm{jet}} < 30\,\mathrm{GeV}$.

Inclusive jet cross sections in bins of Q^2 and P_T^{jet} using the k_T jet algorithm

Bin label	σ [pb]	δ^{stat} [%]	δ^{sys} [%]	δ^{Model} [%]	δ^{JES} [%]	δ^{RCES} [%]	$\delta^{E'_e}$ [%]	δ^{θ_e} [%]	$\delta^{\text{ID(e)}}$ [%]	c^{had}	δ^{had} [%]	c^{ew}
1α	$7.06 \cdot 10^{1}$	2.7	2.9	+1.0	${}^{+0.9}_{-1.1}$	${}^{+0.9}_{-1.0}$	${}^{-0.4}_{+0.3}$	${}^{-0.4}_{+0.3}$	${}^{+0.5}_{-0.5}$	0.93	2.2	1.00
1β	$3.10 \cdot 10^{1}$	4.1	4.4	+2.8	${}^{+2.4}_{-2.5}$	${}^{+0.6}_{-0.5}$	${}^{-0.7}_{+0.5}$	${}^{-0.3}_{+0.2}$	${}^{+0.5}_{-0.5}$	0.97	1.7	1.00
1γ	$8.07 \cdot 10^{0}$	6.4	5.3	+3.5	${}^{+3.4}_{-3.4}$	${}^{+0.3}_{-0.1}$	${}^{-0.4}_{+0.5}$	${}^{-0.1}_{+0.1}$	${}^{+0.5}_{-0.5}$	0.96	1.1	1.00
1δ	$9.18 \cdot 10^{-1}$	15.3	12.9	+11.7	${}^{+4.9}_{-5.3}$	${}^{+0.2}_{-0.1}$	${}^{-0.1}_{-0.5}$	${}^{-0.2}_{-0.1}$	${}^{+0.5}_{-0.5}$	0.95	0.7	1.00
2α	$5.48 \cdot 10^{1}$	3.0	2.9	−0.6	${}^{+0.9}_{-1.0}$	${}^{+1.2}_{-1.0}$	${}^{-0.6}_{+0.9}$	${}^{-0.3}_{+0.4}$	${}^{+0.5}_{-0.5}$	0.93	2.1	1.00
2β	$2.68 \cdot 10^{1}$	4.1	4.8	+3.4	${}^{+2.4}_{-2.4}$	${}^{+0.4}_{-0.4}$	${}^{-0.6}_{+0.6}$	${}^{-0.3}_{+0.3}$	${}^{+0.5}_{-0.5}$	0.97	1.7	1.00
2γ	$7.01 \cdot 10^{0}$	6.6	6.4	+4.8	${}^{+3.7}_{-3.4}$	${}^{+0.2}_{-0.2}$	${}^{-0.6}_{+0.5}$	${}^{-0.4}_{+0.3}$	${}^{+0.5}_{-0.5}$	0.97	1.3	1.00
2δ	$8.52 \cdot 10^{-1}$	15.2	7.4	+4.6	${}^{+5.7}_{-4.8}$	${}^{-0.2}_{-0.1}$	${}^{+0.0}_{+0.1}$	${}^{-0.3}_{+0.3}$	${}^{+0.5}_{-0.5}$	0.96	1.2	1.00
3α	$5.22 \cdot 10^{1}$	3.0	3.2	+1.5	${}^{+0.9}_{-1.0}$	${}^{+1.0}_{-1.0}$	${}^{-1.0}_{+0.7}$	${}^{-0.3}_{+0.3}$	${}^{+0.5}_{-0.5}$	0.93	1.5	1.00
3β	$2.78 \cdot 10^{1}$	4.0	4.5	+3.1	${}^{+2.3}_{-2.2}$	${}^{+0.4}_{-0.4}$	${}^{-0.7}_{+0.9}$	${}^{-0.2}_{+0.3}$	${}^{+0.4}_{-0.4}$	0.97	1.1	1.00
3γ	$6.99 \cdot 10^{0}$	6.8	4.7	+1.9	${}^{+3.5}_{-3.7}$	${}^{+0.2}_{-0.1}$	${}^{-1.0}_{+0.6}$	${}^{-0.0}_{-0.3}$	${}^{+0.4}_{-0.4}$	0.97	0.9	1.00
3δ	$8.69 \cdot 10^{-1}$	15.1	6.7	−3.0	${}^{+5.4}_{-5.7}$	${}^{-0.0}_{-0.2}$	${}^{+0.8}_{-0.3}$	${}^{-0.1}_{+0.4}$	${}^{+0.4}_{-0.4}$	0.95	0.5	1.00
4α	$4.88 \cdot 10^{1}$	3.2	3.3	+1.5	${}^{+1.2}_{-1.4}$	${}^{+0.7}_{-0.7}$	${}^{-1.1}_{+1.2}$	${}^{-0.2}_{+0.2}$	${}^{+0.4}_{-0.4}$	0.93	1.2	1.00
4β	$2.69 \cdot 10^{1}$	4.1	3.3	+1.2	${}^{+2.0}_{-2.0}$	${}^{+0.4}_{-0.4}$	${}^{-0.7}_{+0.7}$	${}^{-0.1}_{+0.1}$	${}^{+0.4}_{-0.4}$	0.97	1.0	1.00
4γ	$7.95 \cdot 10^{0}$	6.1	5.6	+3.5	${}^{+3.8}_{-3.6}$	${}^{+0.2}_{-0.4}$	${}^{-0.8}_{+0.8}$	${}^{-0.1}_{+0.1}$	${}^{+0.3}_{-0.3}$	0.97	0.5	1.00
4δ	$8.57 \cdot 10^{-1}$	16.5	10.8	−8.9	${}^{+5.7}_{-5.5}$	${}^{-0.1}_{-0.1}$	${}^{-0.1}_{-0.1}$	${}^{+0.1}_{-0.1}$	${}^{+0.2}_{-0.2}$	0.96	0.4	1.00
5α	$4.33 \cdot 10^{1}$	3.5	3.5	+2.2	${}^{+1.0}_{-1.2}$	${}^{+0.5}_{-0.4}$	${}^{-0.4}_{+0.5}$	${}^{-0.5}_{+0.5}$	${}^{+1.1}_{-1.1}$	0.92	0.9	1.02
5β	$2.85 \cdot 10^{1}$	4.0	3.3	+1.4	${}^{+1.6}_{-1.5}$	${}^{+0.1}_{-0.1}$	${}^{-0.5}_{+0.6}$	${}^{-0.6}_{+0.6}$	${}^{+1.1}_{-1.1}$	0.97	0.5	1.02
5γ	$1.07 \cdot 10^{1}$	4.9	4.6	+2.7	${}^{+2.7}_{-2.8}$	${}^{+0.1}_{-0.1}$	${}^{-0.5}_{+0.6}$	${}^{-0.4}_{+0.4}$	${}^{+1.1}_{-1.1}$	0.97	0.4	1.03
5δ	$2.04 \cdot 10^{0}$	8.5	5.7	+2.1	${}^{+4.8}_{-4.5}$	${}^{+0.1}_{-0.0}$	${}^{-0.3}_{+0.3}$	${}^{-0.2}_{+0.2}$	${}^{+1.0}_{-1.0}$	0.96	0.3	1.02
6α	$2.60 \cdot 10^{0}$	14.7	4.4	−3.0	${}^{+0.8}_{-0.9}$	${}^{+0.3}_{-0.5}$	${}^{-0.6}_{-1.6}$	${}^{-0.3}_{+0.6}$	${}^{+1.9}_{-1.9}$	0.91	0.6	1.11
6β	$1.74 \cdot 10^{0}$	16.4	3.5	+1.1	${}^{+1.6}_{-1.2}$	${}^{+0.1}_{+0.0}$	${}^{+0.2}_{+1.2}$	${}^{-0.4}_{+0.9}$	${}^{+1.8}_{-1.8}$	0.96	0.6	1.11
6γ	$6.71 \cdot 10^{-1}$	21.6	13.4	−12.9	${}^{+2.2}_{-2.0}$	${}^{+0.2}_{-0.3}$	${}^{-0.2}_{-0.0}$	${}^{-0.5}_{+0.6}$	${}^{+1.8}_{-1.8}$	0.99	1.1	1.11
6δ	$3.09 \cdot 10^{-1}$	19.7	20.0	−19.5	${}^{+2.9}_{-2.8}$	${}^{+0.1}_{+0.0}$	${}^{+0.3}_{-0.9}$	${}^{+0.0}_{+0.1}$	${}^{+1.8}_{-1.8}$	0.98	0.8	1.11

Table 8: Double-differential inclusive jet cross sections measured as a function of Q^2 and P_T^{jet} using the k_T jet algorithm. The bin labels are defined in table 7. The data points are statistically correlated, and the bin-to-bin correlations are given in the correlation matrix in table 28. The correlation with the dijet measurements as a function of $\langle P_T \rangle_2$ and ξ_2 are given in tables 31 and 36, respectively. The correlations with the trijet measurements as a function of $\langle P_T \rangle_3$ and ξ_3 are shown in tables 32 and 37, respectively. The experimental uncertaintes quoted are defined in section 4.2. The total systematic uncertainty, δ^{sys}, sums all systematic uncertainties in quadrature, including the uncertainty due to the LAr noise of $\delta^{\text{LArNoise}} = 0.5\,\%$ and the total normalisation uncertainty of $\delta^{\text{Norm}} = 2.9\,\%$. The contributions to the correlated systematic uncertainty from a positive variation of one standard deviation of the model variation (δ^{Model}), of the jet energy scale (δ^{JES}), of the remaining cluster energy scale (δ^{RCES}), of the scattered electron energy ($\delta^{E'_e}$), of the polar electron angle (δ^{θ_e}) and of the Electron ID ($\delta^{\text{ID(e)}}$) are also given. In case of asymmetric uncertainties, the effect due to the positive variation of the underlying error source is given by the upper value for the corresponding table entry. The correction factors on the theoretical cross sections c^{had} and c^{ew} are listed in the rightmost columns together with the uncertainties δ^{had}.

Dijet cross sections in bins of Q^2 and $\langle P_T \rangle_2$ using the k_T jet algorithm

Bin label	σ [pb]	$\delta^{\rm stat}$ [%]	$\delta^{\rm sys}$ [%]	$\delta^{\rm Model}$ [%]	$\delta^{\rm JES}$ [%]	$\delta^{\rm RCES}$ [%]	$\delta^{E_e'}$ [%]	δ^{θ_e} [%]	$\delta^{\rm ID(e)}$ [%]	$c^{\rm had}$	$\delta^{\rm had}$ [%]	$c^{\rm ew}$
1α	$2.34 \cdot 10^{1}$	3.6	3.4	+2.1	$^{+0.1}_{-0.3}$	$^{+1.3}_{-1.3}$	$^{-0.5}_{+0.2}$	$^{-0.4}_{+0.3}$	$^{+0.5}_{-0.5}$	0.94	2.0	1.00
1β	$1.36 \cdot 10^{1}$	5.8	4.5	+3.5	$^{+1.8}_{-1.9}$	$^{+0.2}_{-0.3}$	$^{-0.2}_{+0.2}$	$^{-0.2}_{+0.4}$	$^{+0.5}_{-0.5}$	0.97	1.4	1.00
1γ	$3.57 \cdot 10^{0}$	6.7	6.1	+4.0	$^{+4.0}_{-3.9}$	$^{+0.2}_{-0.0}$	$^{-0.4}_{+0.2}$	$^{-0.2}_{+0.1}$	$^{+0.5}_{-0.5}$	0.96	1.0	1.00
1δ	$4.20 \cdot 10^{-1}$	16.4	9.6	+7.8	$^{+5.4}_{-4.9}$	$^{+0.1}_{+0.1}$	$^{-0.6}_{-0.4}$	$^{-0.2}_{-0.1}$	$^{+0.5}_{-0.5}$	0.96	1.2	1.00
2α	$1.81 \cdot 10^{1}$	4.1	3.3	+2.0	$^{+0.1}_{-0.0}$	$^{+1.4}_{-1.2}$	$^{-0.4}_{+0.6}$	$^{-0.4}_{+0.5}$	$^{+0.5}_{-0.5}$	0.94	1.7	1.00
2β	$1.24 \cdot 10^{1}$	5.6	3.9	+2.2	$^{+2.0}_{-2.4}$	$^{+0.4}_{-0.4}$	$^{-0.6}_{+0.7}$	$^{-0.3}_{+0.3}$	$^{+0.5}_{-0.5}$	0.98	1.6	1.00
2γ	$2.95 \cdot 10^{0}$	7.4	5.8	+4.0	$^{+3.7}_{-3.4}$	$^{+0.1}_{-0.2}$	$^{-0.1}_{+0.1}$	$^{-0.3}_{+0.2}$	$^{+0.5}_{-0.5}$	0.97	1.0	1.00
2δ	$3.82 \cdot 10^{-1}$	18.1	13.7	+12.4	$^{+6.2}_{-4.3}$	$^{-0.2}_{-0.1}$	$^{-0.0}_{+0.1}$	$^{-0.4}_{+0.2}$	$^{+0.5}_{-0.5}$	0.95	1.9	1.00
3α	$1.83 \cdot 10^{1}$	3.9	2.8	+1.0	$^{-0.0}_{-0.0}$	$^{+1.1}_{-1.1}$	$^{-0.5}_{+0.5}$	$^{-0.3}_{+0.2}$	$^{+0.4}_{-0.4}$	0.93	1.2	1.00
3β	$1.13 \cdot 10^{1}$	6.1	4.9	+3.7	$^{+2.2}_{-2.2}$	$^{+0.3}_{-0.3}$	$^{-0.6}_{+0.5}$	$^{-0.3}_{+0.3}$	$^{+0.4}_{-0.4}$	0.98	0.9	1.00
3γ	$3.80 \cdot 10^{0}$	6.0	4.3	+1.2	$^{+3.3}_{-3.6}$	$^{+0.1}_{-0.1}$	$^{-0.4}_{+0.1}$	$^{-0.1}_{-0.1}$	$^{+0.4}_{-0.4}$	0.97	0.8	1.00
3δ	$3.44 \cdot 10^{-1}$	20.5	9.3	−7.0	$^{+4.9}_{-6.4}$	$^{+0.0}_{-0.3}$	$^{-0.2}_{-0.6}$	$^{-0.2}_{-0.2}$	$^{+0.4}_{-0.4}$	0.96	0.4	1.00
4α	$1.67 \cdot 10^{1}$	4.1	2.5	+0.7	$^{+0.1}_{+0.1}$	$^{+0.9}_{-0.8}$	$^{-0.3}_{+0.4}$	$^{-0.2}_{+0.2}$	$^{+0.4}_{-0.4}$	0.92	1.1	1.00
4β	$1.08 \cdot 10^{1}$	6.3	4.7	+3.5	$^{+1.9}_{-2.2}$	$^{+0.3}_{-0.4}$	$^{-0.5}_{+0.6}$	$^{-0.1}_{+0.1}$	$^{+0.4}_{-0.4}$	0.97	0.9	1.00
4γ	$3.65 \cdot 10^{0}$	6.2	4.5	+2.2	$^{+3.2}_{-3.3}$	$^{+0.1}_{-0.1}$	$^{-0.3}_{+0.4}$	$^{-0.1}_{+0.2}$	$^{+0.3}_{-0.3}$	0.98	0.5	1.00
4δ	$3.79 \cdot 10^{-1}$	20.4	7.1	−3.7	$^{+5.5}_{-5.8}$	$^{+0.0}_{-0.1}$	$^{-0.3}_{+0.3}$	$^{+0.0}_{-0.1}$	$^{+0.2}_{-0.2}$	0.96	0.3	1.00
5α	$1.49 \cdot 10^{1}$	4.4	2.9	+1.0	$^{-0.4}_{+0.5}$	$^{+0.6}_{-0.5}$	$^{+0.8}_{-0.6}$	$^{-0.4}_{+0.4}$	$^{+1.2}_{-1.2}$	0.92	0.6	1.02
5β	$1.32 \cdot 10^{1}$	5.1	3.6	+2.1	$^{+1.5}_{-1.5}$	$^{+0.2}_{-0.1}$	$^{-0.3}_{+0.3}$	$^{-0.5}_{+0.5}$	$^{+1.1}_{-1.1}$	0.96	0.3	1.02
5γ	$4.77 \cdot 10^{0}$	5.4	6.1	+5.0	$^{+2.5}_{-2.6}$	$^{+0.2}_{-0.1}$	$^{-0.2}_{+0.3}$	$^{-0.4}_{+0.3}$	$^{+1.1}_{-1.1}$	0.98	0.4	1.03
5δ	$9.57 \cdot 10^{-1}$	10.3	5.6	+2.0	$^{+4.7}_{-4.5}$	$^{+0.0}_{+0.2}$	$^{-0.4}_{+0.1}$	$^{-0.1}_{+0.1}$	$^{+1.0}_{-1.0}$	0.96	0.7	1.01
6α	$7.29 \cdot 10^{-1}$	23.0	4.0	−2.2	$^{-0.3}_{+0.8}$	$^{+0.1}_{-0.5}$	$^{+1.1}_{-1.4}$	$^{-0.1}_{+0.7}$	$^{+2.1}_{-2.1}$	0.89	0.2	1.11
6β	$8.45 \cdot 10^{-1}$	20.1	10.2	+9.5	$^{+2.8}_{-0.6}$	$^{+0.2}_{-0.1}$	$^{-0.1}_{+2.4}$	$^{-0.4}_{+1.8}$	$^{+1.8}_{-1.8}$	0.95	0.5	1.11
6γ	$3.49 \cdot 10^{-1}$	19.3	6.0	−4.8	$^{+1.4}_{-2.6}$	$^{+0.2}_{-0.4}$	$^{+0.1}_{-1.1}$	$^{-1.2}_{+0.3}$	$^{+1.9}_{-1.9}$	0.97	0.8	1.11
6δ	$1.47 \cdot 10^{-1}$	26.9	8.5	−7.5	$^{+3.1}_{-1.7}$	$^{-0.0}_{+0.2}$	$^{+1.7}_{-0.4}$	$^{+1.0}_{-0.3}$	$^{+1.8}_{-1.8}$	0.98	1.0	1.11

Table 9: Double-differential dijet cross sections measured as a function of Q^2 and $\langle P_T \rangle_2$ using the k_T jet algorithm. The total systematic uncertainty, $\delta^{\rm sys}$, sums all systematic uncertainties in quadrature, including the uncertainty due to the LAr noise of $\delta^{\rm LArNoise} = 0.6\,\%$ and the total normalisation uncertainty of $\delta^{\rm Norm} = 2.9\,\%$. The correlations between the data points are listed in table 29. The statistical correlations with the trijet measurement as a function of $\langle P_T \rangle$ are listed in table 33. Further details are given in the caption of table 8.

Dijet cross sections in bins of Q^2 and ξ_2 using the k_T jet algorithm

Bin label	σ [pb]	$\delta^{\rm stat}$ [%]	$\delta^{\rm sys}$ [%]	$\delta^{\rm Model}$ [%]	$\delta^{\rm JES}$ [%]	$\delta^{\rm RCES}$ [%]	$\delta^{E'_e}$ [%]	δ^{θ_e} [%]	$\delta^{\rm ID(e)}$ [%]	$c^{\rm had}$	$\delta^{\rm had}$ [%]	$c^{\rm ew}$
1a	$2.04 \cdot 10^1$	4.2	7.7	+7.2	$^{+1.0}_{-1.1}$	$^{+1.4}_{-1.4}$	$^{+0.3}_{-0.5}$	$^{-0.4}_{+0.3}$	$^{+0.5}_{-0.5}$	0.94	2.1	1.00
1b	$1.82 \cdot 10^1$	3.4	4.4	+3.4	$^{+1.2}_{-1.5}$	$^{+1.0}_{-1.0}$	$^{+0.2}_{-0.2}$	$^{-0.2}_{+0.2}$	$^{+0.5}_{-0.5}$	0.94	1.7	1.00
1c	$6.01 \cdot 10^0$	7.0	4.0	+2.3	$^{+2.5}_{-2.2}$	$^{+0.1}_{-0.1}$	$^{+0.2}_{-0.2}$	$^{-0.4}_{+0.3}$	$^{+0.5}_{-0.5}$	0.94	1.3	1.00
1d	$1.98 \cdot 10^0$	8.8	7.9	+6.7	$^{+3.4}_{-3.1}$	$^{-0.2}_{+0.1}$	$^{-1.7}_{+1.3}$	$^{-0.2}_{+0.2}$	$^{+0.5}_{-0.5}$	0.92	0.7	1.00
2a	$1.45 \cdot 10^1$	5.0	4.9	+4.1	$^{+0.8}_{-0.9}$	$^{+1.2}_{-1.2}$	$^{+0.0}_{+0.2}$	$^{-0.3}_{+0.4}$	$^{+0.5}_{-0.5}$	0.94	1.8	1.00
2b	$1.58 \cdot 10^1$	3.6	3.9	+2.7	$^{+1.1}_{-1.3}$	$^{+1.0}_{-1.0}$	$^{+0.6}_{-0.7}$	$^{-0.3}_{+0.4}$	$^{+0.5}_{-0.5}$	0.94	1.7	1.00
2c	$6.19 \cdot 10^0$	6.3	3.4	+0.7	$^{+2.4}_{-2.5}$	$^{+0.1}_{-0.1}$	$^{+0.3}_{-0.1}$	$^{-0.2}_{+0.3}$	$^{+0.5}_{-0.5}$	0.94	1.1	1.00
2d	$1.71 \cdot 10^0$	9.4	7.0	+5.8	$^{+3.2}_{-2.8}$	$^{-0.3}_{+0.3}$	$^{-1.1}_{+1.2}$	$^{-0.3}_{+0.5}$	$^{+0.5}_{-0.5}$	0.93	0.6	1.00
3a	$1.13 \cdot 10^1$	4.2	5.5	+4.9	$^{+0.7}_{-0.8}$	$^{+1.0}_{-1.1}$	$^{-0.2}_{+0.1}$	$^{-0.2}_{+0.2}$	$^{+0.4}_{-0.4}$	0.93	1.4	1.00
3b	$1.76 \cdot 10^1$	3.0	3.9	+2.8	$^{+1.0}_{-1.1}$	$^{+0.9}_{-0.9}$	$^{+0.5}_{-0.6}$	$^{-0.3}_{+0.2}$	$^{+0.5}_{-0.5}$	0.94	1.2	1.00
3c	$8.32 \cdot 10^0$	4.6	3.4	+1.4	$^{+2.0}_{-2.1}$	$^{+0.3}_{-0.2}$	$^{+0.3}_{-0.3}$	$^{-0.2}_{+0.3}$	$^{+0.4}_{-0.4}$	0.94	0.9	1.00
3d	$1.99 \cdot 10^0$	8.3	5.3	+3.4	$^{+3.4}_{-3.3}$	$^{-0.2}_{+0.1}$	$^{-0.6}_{+0.3}$	$^{-0.4}_{+0.1}$	$^{+0.5}_{-0.5}$	0.94	0.4	1.00
4a	$5.12 \cdot 10^0$	7.7	8.6	+8.2	$^{+0.3}_{-0.8}$	$^{+0.8}_{-0.9}$	$^{+0.4}_{-0.5}$	$^{-0.2}_{+0.2}$	$^{+0.2}_{-0.2}$	0.92	1.4	1.00
4b	$1.78 \cdot 10^1$	3.2	5.2	+4.6	$^{+0.8}_{-1.0}$	$^{+0.7}_{-0.8}$	$^{+0.1}_{-0.3}$	$^{-0.1}_{+0.1}$	$^{+0.4}_{-0.4}$	0.93	1.2	1.00
4c	$1.12 \cdot 10^1$	3.8	3.1	+1.3	$^{+1.5}_{-1.4}$	$^{+0.5}_{-0.5}$	$^{+0.7}_{-0.8}$	$^{-0.1}_{+0.1}$	$^{+0.4}_{-0.4}$	0.94	0.8	1.00
4d	$2.37 \cdot 10^0$	8.2	6.8	+5.6	$^{+3.3}_{-3.2}$	$^{+0.0}_{-0.0}$	$^{-0.0}_{+0.3}$	$^{+0.1}_{+0.1}$	$^{+0.3}_{-0.3}$	0.95	0.5	1.00
5b	$8.89 \cdot 10^0$	3.7	4.5	+3.6	$^{+0.7}_{-0.9}$	$^{+0.5}_{-0.6}$	$^{-0.0}_{-0.1}$	$^{-0.5}_{+0.4}$	$^{+1.2}_{-1.2}$	0.92	0.5	1.01
5c	$1.71 \cdot 10^1$	2.9	3.5	+2.1	$^{+0.9}_{-0.9}$	$^{+0.6}_{-0.6}$	$^{+0.5}_{-0.5}$	$^{-0.4}_{+0.3}$	$^{+1.0}_{-1.0}$	0.93	0.5	1.02
5d	$1.12 \cdot 10^1$	3.0	4.2	+3.1	$^{+1.3}_{-1.3}$	$^{+0.3}_{-0.3}$	$^{-0.0}_{-0.2}$	$^{-0.4}_{+0.3}$	$^{+1.1}_{-1.1}$	0.94	0.4	1.03
6d	$1.86 \cdot 10^0$	7.2	5.5	+4.6	$^{+0.6}_{-0.6}$	$^{+0.2}_{-0.3}$	$^{+0.5}_{-0.8}$	$^{-0.3}_{+0.4}$	$^{+1.9}_{-1.9}$	0.93	0.8	1.11

Table 10: Double-differential dijet cross sections measured as a function of Q^2 and ξ_2 using the k_T jet algorithm. The total systematic uncertainty, $\delta^{\rm sys}$, sums all systematic uncertainties in quadrature, including the uncertainty due to the LAr noise of $\delta^{\rm LArNoise} = 0.6\,\%$ and the total normalisation uncertainty of $\delta^{\rm Norm} = 2.9\,\%$. The correlations between the data points are listed in table 34. The statistical correlations with the trijet measurement as a function of ξ_3 are listed in table 38. Further details are given in the caption of table 8.

Trijet cross sections in bins of Q^2 and $\langle P_{\mathrm{T}}\rangle_3$ using the k_{T} jet algorithm

Bin label	σ [pb]	δ^{stat} [%]	δ^{sys} [%]	δ^{Model} [%]	δ^{JES} [%]	δ^{RCES} [%]	$\delta^{E'_e}$ [%]	δ^{θ_e} [%]	$\delta^{\mathrm{ID(e)}}$ [%]	c^{had}	δ^{had} [%]	c^{ew}
1α	$4.86\cdot10^{0}$	8.9	5.1	+2.9	$^{-0.9}_{+1.2}$	$^{+3.5}_{-3.3}$	$^{-0.2}_{+0.3}$	$^{-0.2}_{+0.3}$	$^{+0.5}_{-0.5}$	0.79	5.3	1.00
1β	$2.65\cdot10^{0}$	8.6	4.5	+1.8	$^{+3.0}_{-3.3}$	$^{+1.0}_{-1.2}$	$^{+0.2}_{+0.0}$	$^{-0.4}_{+0.3}$	$^{+0.5}_{-0.5}$	0.85	4.3	1.00
1γ	$4.37\cdot10^{-1}$	18.0	8.4	+6.7	$^{+4.4}_{-4.8}$	$^{+0.4}_{-0.1}$	$^{-1.0}_{-0.0}$	$^{+0.3}_{-0.1}$	$^{+0.5}_{-0.5}$	0.89	3.6	1.00
2α	$3.28\cdot10^{0}$	11.1	4.9	−2.0	$^{-1.5}_{+1.0}$	$^{+3.3}_{-3.8}$	$^{-0.2}_{+0.3}$	$^{-0.4}_{+0.4}$	$^{+0.5}_{-0.5}$	0.78	5.0	1.00
2β	$2.06\cdot10^{0}$	9.2	5.7	+4.0	$^{+2.9}_{-3.0}$	$^{+1.4}_{-1.4}$	$^{-0.3}_{+0.1}$	$^{-0.2}_{+0.2}$	$^{+0.5}_{-0.5}$	0.84	4.4	1.00
2γ	$4.28\cdot10^{-1}$	17.5	5.5	−1.2	$^{+4.8}_{-4.5}$	$^{+0.7}_{-0.6}$	$^{+1.1}_{-0.3}$	$^{-0.7}_{+0.5}$	$^{+0.5}_{-0.5}$	0.89	2.7	1.00
3α	$3.46\cdot10^{0}$	10.5	5.1	−2.5	$^{-1.2}_{+1.2}$	$^{+3.5}_{-3.6}$	$^{-0.2}_{+0.5}$	$^{-0.2}_{+0.2}$	$^{+0.4}_{-0.4}$	0.78	4.6	1.00
3β	$2.65\cdot10^{0}$	8.0	6.5	+5.3	$^{+2.5}_{-2.8}$	$^{+1.3}_{-1.4}$	$^{-0.7}_{+0.5}$	$^{-0.0}_{+0.1}$	$^{+0.4}_{-0.4}$	0.85	3.7	1.00
3γ	$5.07\cdot10^{-1}$	16.8	7.2	−3.8	$^{+5.9}_{-5.4}$	$^{+0.7}_{-0.6}$	$^{-1.0}_{+0.1}$	$^{+0.1}_{-0.6}$	$^{+0.4}_{-0.4}$	0.87	2.3	1.00
4α	$3.06\cdot10^{0}$	11.2	7.6	−6.5	$^{-0.9}_{+0.8}$	$^{+3.3}_{-3.0}$	$^{-0.4}_{+0.3}$	$^{-0.1}_{+0.0}$	$^{+0.3}_{-0.3}$	0.77	4.1	1.00
4β	$2.83\cdot10^{0}$	7.4	7.3	+6.4	$^{+2.4}_{-2.4}$	$^{+1.2}_{-1.3}$	$^{-0.8}_{+0.9}$	$^{-0.1}_{+0.1}$	$^{+0.3}_{-0.3}$	0.85	3.6	1.00
4γ	$6.86\cdot10^{-1}$	13.8	7.5	+3.8	$^{+6.0}_{-6.0}$	$^{+0.9}_{-0.4}$	$^{-0.3}_{+0.5}$	$^{+0.1}_{+0.1}$	$^{+0.1}_{-0.1}$	0.87	2.3	1.00
5α	$3.23\cdot10^{0}$	9.8	7.1	−5.9	$^{-1.6}_{+1.6}$	$^{+2.0}_{-2.0}$	$^{+1.3}_{-1.1}$	$^{-0.3}_{+0.4}$	$^{+1.4}_{-1.4}$	0.77	3.5	1.03
5β	$2.91\cdot10^{0}$	7.4	6.2	+5.3	$^{+1.5}_{-1.6}$	$^{+1.0}_{-0.9}$	$^{-0.2}_{+0.5}$	$^{-0.4}_{+0.3}$	$^{+1.3}_{-1.3}$	0.83	2.9	1.03
5γ	$6.61\cdot10^{-1}$	14.5	14.5	+13.5	$^{+4.8}_{-4.6}$	$^{+0.5}_{-0.6}$	$^{-1.0}_{+0.6}$	$^{-0.0}_{+0.0}$	$^{+1.1}_{-1.1}$	0.86	2.2	1.03
6β	$1.21\cdot10^{-1}$	37.9	5.5	+4.2	$^{+0.0}_{+0.0}$	$^{+1.1}_{-0.9}$	$^{+1.4}_{-0.5}$	$^{-0.2}_{+0.8}$	$^{+2.2}_{-2.2}$	0.82	0.8	1.12

Table 11: Double-differential trijet cross sections measured as a function of Q^2 and $\langle P_{\mathrm{T}}\rangle_3$ using the k_{T} jet algorithm. The total systematic uncertainty, δ^{sys}, sums all systematic uncertainties in quadrature, including the uncertainty due to the LAr noise of $\delta^{\mathrm{LArNoise}} = 0.9\,\%$ and the total normalisation uncertainty of $\delta^{\mathrm{Norm}} = 2.9\,\%$. The correlations between the data points are listed in table 30. Further details are given in the caption of table 8.

Trijet cross sections in bins of Q^2 and ξ_3 using the k_T jet algorithm

Bin label	σ [pb]	δ^{stat} [%]	δ^{sys} [%]	δ^{Model} [%]	δ^{JES} [%]	δ^{RCES} [%]	$\delta^{E'_e}$ [%]	δ^{θ_e} [%]	$\delta^{\mathrm{ID(e)}}$ [%]	c^{had}	δ^{had} [%]	c^{ew}
1A	$3.15 \cdot 10^{0}$	11.4	18.7	+18.1	$^{-0.2}_{+0.2}$	$^{+4.1}_{-4.2}$	$^{+0.5}_{-1.0}$	$^{-0.4}_{+0.3}$	$^{+0.5}_{-0.5}$	0.81	6.5	1.00
1B	$3.12 \cdot 10^{0}$	10.6	3.8	+2.2	$^{+1.2}_{-1.6}$	$^{+1.5}_{-1.3}$	$^{-0.2}_{+0.3}$	$^{-0.2}_{+0.1}$	$^{+0.4}_{-0.4}$	0.81	5.3	1.00
1C	$1.24 \cdot 10^{0}$	13.2	7.7	−5.8	$^{+4.6}_{-4.3}$	$^{+0.4}_{-0.6}$	$^{+0.5}_{-0.6}$	$^{-0.4}_{+0.3}$	$^{+0.4}_{-0.4}$	0.81	3.7	1.00
2A	$1.87 \cdot 10^{0}$	16.5	12.2	+11.3	$^{+0.5}_{-0.2}$	$^{+3.7}_{-3.7}$	$^{+0.8}_{-0.8}$	$^{-0.4}_{+0.3}$	$^{+0.5}_{-0.5}$	0.80	5.7	1.00
2B	$2.80 \cdot 10^{0}$	10.7	21.7	−21.4	$^{+1.2}_{-1.9}$	$^{+1.6}_{-1.8}$	$^{+0.5}_{-0.6}$	$^{-0.4}_{+0.3}$	$^{+0.5}_{-0.5}$	0.81	4.9	1.00
2C	$9.74 \cdot 10^{-1}$	15.0	15.6	+15.0	$^{+3.9}_{-3.0}$	$^{+0.6}_{-0.4}$	$^{+0.7}_{-0.2}$	$^{-0.3}_{+0.4}$	$^{+0.4}_{-0.4}$	0.80	3.5	1.00
3A	$1.88 \cdot 10^{0}$	14.7	16.0	+15.4	$^{-0.1}_{-0.1}$	$^{+3.4}_{-3.5}$	$^{+1.0}_{-0.6}$	$^{+0.1}_{+0.1}$	$^{+0.4}_{-0.4}$	0.80	5.1	1.00
3B	$3.19 \cdot 10^{0}$	9.3	9.4	+8.8	$^{+0.6}_{-0.8}$	$^{+2.1}_{-2.0}$	$^{+0.0}_{-0.2}$	$^{-0.3}_{+0.3}$	$^{+0.4}_{-0.4}$	0.81	4.5	1.00
3C	$1.48 \cdot 10^{0}$	12.0	13.0	−12.2	$^{+3.9}_{-2.9}$	$^{+0.9}_{-0.8}$	$^{+0.8}_{-0.3}$	$^{+0.1}_{+0.2}$	$^{+0.4}_{-0.4}$	0.80	3.0	1.00
4A	$1.55 \cdot 10^{0}$	16.0	10.7	+10.0	$^{-1.0}_{+1.1}$	$^{+2.3}_{-2.7}$	$^{+0.8}_{-1.5}$	$^{-0.4}_{+0.2}$	$^{+0.1}_{-0.1}$	0.80	5.1	1.00
4B	$2.99 \cdot 10^{0}$	10.1	10.9	+10.4	$^{+0.4}_{-0.4}$	$^{+2.1}_{-2.0}$	$^{+0.4}_{-0.1}$	$^{+0.1}_{-0.0}$	$^{+0.4}_{-0.4}$	0.81	4.5	1.00
4C	$1.98 \cdot 10^{0}$	9.2	5.3	−3.6	$^{+3.1}_{-3.1}$	$^{+0.6}_{-0.5}$	$^{+0.1}_{-0.3}$	$^{-0.2}_{+0.0}$	$^{+0.3}_{-0.3}$	0.81	3.1	1.00
5B	$2.86 \cdot 10^{0}$	9.4	6.3	+5.5	$^{-0.0}_{+0.0}$	$^{+1.4}_{-1.3}$	$^{+0.1}_{+0.1}$	$^{-0.6}_{+0.6}$	$^{+1.4}_{-1.4}$	0.80	2.9	1.03
5C	$3.26 \cdot 10^{0}$	7.6	13.1	+12.8	$^{+1.3}_{-1.5}$	$^{+1.2}_{-1.2}$	$^{+0.2}_{-0.2}$	$^{-0.1}_{+0.1}$	$^{+1.2}_{-1.2}$	0.80	2.8	1.04
6C	$3.63 \cdot 10^{-1}$	17.4	35.5	+35.3	$^{+1.0}_{-0.6}$	$^{+1.2}_{-1.1}$	$^{+1.6}_{-1.0}$	$^{+0.3}_{+0.3}$	$^{+2.2}_{-2.2}$	0.79	1.1	1.11

Table 12: Double-differential trijet cross sections measured as a function of Q^2 and ξ_3 using the k_T jet algorithm. The total systematic uncertainty, δ^{sys}, sums all systematic uncertainties in quadrature, including the uncertainty due to the LAr noise of $\delta^{\mathrm{LArNoise}} = 0.9\,\%$ and the total normalisation uncertainty of $\delta^{\mathrm{Norm}} = 2.9\,\%$. The correlations between the data points are listed in table 35. Further details are given in the captions of the table8.

Inclusive jet cross sections in bins of Q^2 and $P_T^{\rm jet}$ using the anti$-k_T$ jet algorithm

Bin label	σ [pb]	$\delta^{\rm stat}$ [%]	$\delta^{\rm sys}$ [%]	$\delta^{\rm Model}$ [%]	$\delta^{\rm JES}$ [%]	$\delta^{\rm RCES}$ [%]	$\delta^{E_e'}$ [%]	δ^{θ_e} [%]	$\delta^{\rm ID(e)}$ [%]	$c^{\rm had}$	$c^{\rm ew}$
1α	$6.99\cdot10^{1}$	2.3	2.9	+0.8	$^{+1.0}_{-1.1}$	$^{+1.1}_{-1.1}$	$^{-0.5}_{+0.3}$	$^{-0.4}_{+0.3}$	$^{+0.5}_{-0.5}$	0.93	1.00
1β	$3.11\cdot10^{1}$	3.4	4.6	+3.0	$^{+2.5}_{-2.6}$	$^{+0.6}_{-0.5}$	$^{-0.5}_{+0.6}$	$^{-0.3}_{+0.2}$	$^{+0.5}_{-0.5}$	0.94	1.00
1γ	$7.28\cdot10^{0}$	6.3	6.2	+4.5	$^{+3.8}_{-3.4}$	$^{+0.3}_{-0.3}$	$^{-0.3}_{+0.7}$	$^{-0.1}_{+0.1}$	$^{+0.5}_{-0.5}$	0.93	1.00
1δ	$8.68\cdot10^{-1}$	16.2	6.9	+4.4	$^{+4.9}_{-4.9}$	$^{-0.0}_{-0.2}$	$^{-0.2}_{-0.4}$	$^{-0.2}_{+0.0}$	$^{+0.5}_{-0.5}$	0.93	1.00
2α	$5.57\cdot10^{1}$	2.5	2.8	+0.5	$^{+0.9}_{-0.9}$	$^{+1.1}_{-1.1}$	$^{-0.5}_{+0.7}$	$^{-0.3}_{+0.4}$	$^{+0.5}_{-0.5}$	0.93	1.00
2β	$2.62\cdot10^{1}$	3.6	4.4	+2.7	$^{+2.5}_{-2.6}$	$^{+0.4}_{-0.4}$	$^{-0.5}_{+0.5}$	$^{-0.3}_{+0.3}$	$^{+0.5}_{-0.5}$	0.95	1.00
2γ	$6.67\cdot10^{0}$	6.4	6.9	+5.6	$^{+3.4}_{-3.3}$	$^{+0.0}_{-0.4}$	$^{-0.8}_{+0.4}$	$^{-0.5}_{+0.3}$	$^{+0.5}_{-0.5}$	0.94	1.00
2δ	$8.85\cdot10^{-1}$	14.2	8.2	+6.0	$^{+5.2}_{-5.1}$	$^{+0.1}_{+0.1}$	$^{-0.2}_{+0.3}$	$^{-0.3}_{+0.2}$	$^{+0.5}_{-0.5}$	0.93	1.00
3α	$5.31\cdot10^{1}$	2.6	2.8	+0.9	$^{+0.8}_{-0.8}$	$^{+1.0}_{-1.1}$	$^{-0.8}_{+0.7}$	$^{-0.3}_{+0.2}$	$^{+0.5}_{-0.5}$	0.94	1.00
3β	$2.73\cdot10^{1}$	3.5	4.4	+2.8	$^{+2.4}_{-2.4}$	$^{+0.4}_{-0.4}$	$^{-0.7}_{+0.8}$	$^{-0.2}_{+0.2}$	$^{+0.4}_{-0.4}$	0.95	1.00
3γ	$7.53\cdot10^{0}$	5.7	5.1	+2.8	$^{+3.5}_{-3.7}$	$^{+0.2}_{-0.1}$	$^{-0.7}_{+0.6}$	$^{-0.1}_{+0.1}$	$^{+0.4}_{-0.4}$	0.95	1.00
3δ	$9.13\cdot10^{-1}$	14.7	8.4	+5.7	$^{+5.3}_{-6.1}$	$^{+0.1}_{+0.0}$	$^{+0.3}_{-0.3}$	$^{-0.0}_{+0.1}$	$^{+0.4}_{-0.4}$	0.93	1.00
4α	$4.63\cdot10^{1}$	2.9	3.4	+1.8	$^{+1.2}_{-1.3}$	$^{+0.8}_{-0.9}$	$^{-1.0}_{+1.1}$	$^{-0.2}_{+0.2}$	$^{+0.4}_{-0.4}$	0.94	1.00
4β	$2.71\cdot10^{1}$	3.5	3.2	+1.2	$^{+1.9}_{-1.9}$	$^{+0.4}_{-0.2}$	$^{-0.7}_{+0.6}$	$^{-0.1}_{+0.1}$	$^{+0.4}_{-0.4}$	0.95	1.00
4γ	$7.85\cdot10^{0}$	5.5	5.8	+4.0	$^{+3.6}_{-3.3}$	$^{+0.3}_{-0.2}$	$^{-0.7}_{+0.7}$	$^{-0.0}_{+0.2}$	$^{+0.3}_{-0.3}$	0.96	1.00
4δ	$8.30\cdot10^{-1}$	16.3	9.5	−7.3	$^{+5.9}_{-5.5}$	$^{-0.0}_{+0.2}$	$^{-0.0}_{-0.0}$	$^{+0.1}_{+0.0}$	$^{+0.2}_{-0.2}$	0.93	1.00
5α	$4.25\cdot10^{1}$	3.0	3.4	+2.1	$^{+0.9}_{-1.0}$	$^{+0.5}_{-0.4}$	$^{-0.2}_{+0.4}$	$^{-0.5}_{+0.5}$	$^{+1.1}_{-1.1}$	0.92	1.02
5β	$2.84\cdot10^{1}$	3.4	3.3	+1.3	$^{+1.7}_{-1.6}$	$^{+0.1}_{-0.2}$	$^{-0.5}_{+0.5}$	$^{-0.6}_{+0.6}$	$^{+1.1}_{-1.1}$	0.97	1.02
5γ	$1.07\cdot10^{1}$	4.3	4.4	+2.3	$^{+2.7}_{-2.6}$	$^{+0.1}_{-0.1}$	$^{-0.6}_{+0.6}$	$^{-0.4}_{+0.4}$	$^{+1.1}_{-1.1}$	0.96	1.03
5δ	$1.83\cdot10^{0}$	9.0	6.4	+3.7	$^{+4.6}_{-4.7}$	$^{+0.1}_{-0.1}$	$^{-0.4}_{+0.3}$	$^{-0.3}_{+0.2}$	$^{+1.0}_{-1.0}$	0.95	1.01
6α	$2.54\cdot10^{0}$	12.8	3.4	+1.4	$^{+0.2}_{-0.8}$	$^{+0.5}_{-0.3}$	$^{-0.2}_{-1.1}$	$^{-0.8}_{+0.1}$	$^{+1.9}_{-1.9}$	0.90	1.11
6β	$1.83\cdot10^{0}$	13.6	3.8	−1.4	$^{+1.7}_{-1.6}$	$^{+0.3}_{-0.4}$	$^{+2.4}_{+0.3}$	$^{+0.6}_{+0.3}$	$^{+1.8}_{-1.8}$	0.95	1.11
6γ	$6.12\cdot10^{-1}$	20.9	7.5	−6.6	$^{+2.2}_{-1.9}$	$^{+0.3}_{-0.2}$	$^{+1.0}_{-0.1}$	$^{-0.1}_{+0.5}$	$^{+1.8}_{-1.8}$	0.98	1.11
6δ	$2.72\cdot10^{-1}$	20.5	18.1	−17.6	$^{+2.6}_{-3.0}$	$^{+0.1}_{-0.2}$	$^{+0.4}_{-0.3}$	$^{-0.2}_{+0.2}$	$^{+1.8}_{-1.8}$	0.98	1.11

Table 13: Double-differential inclusive jet cross sections measured as a function of Q^2 and $P_T^{\rm jet}$ using the anti$-k_T$ jet algorithm. The uncertainties $\delta^{\rm had}$ are identical to those in table 8 and are not repeated here. Further details are given in the caption of table 8.

Dijet cross sections in bins of Q^2 and $\langle P_T \rangle_2$ using the anti$-k_T$ jet algorithm

Bin label	σ [pb]	δ^{stat} [%]	δ^{sys} [%]	δ^{Model} [%]	δ^{JES} [%]	δ^{RCES} [%]	$\delta^{E'_e}$ [%]	δ^{θ_e} [%]	$\delta^{\mathrm{ID(e)}}$ [%]	c^{had}	c^{ew}
1α	$2.36 \cdot 10^{1}$	3.2	3.5	+2.4	$^{+0.2}_{-0.4}$	$^{+1.2}_{-1.1}$	$^{-0.5}_{+0.3}$	$^{-0.4}_{+0.3}$	$^{+0.5}_{-0.5}$	0.95	1.00
1β	$1.43 \cdot 10^{1}$	4.5	5.2	+4.1	$^{+2.0}_{-2.2}$	$^{+0.3}_{-0.4}$	$^{-0.3}_{+0.2}$	$^{-0.3}_{+0.3}$	$^{+0.5}_{-0.5}$	0.95	1.00
1γ	$3.19 \cdot 10^{0}$	6.7	6.3	+4.5	$^{+3.8}_{-3.7}$	$^{+0.2}_{-0.2}$	$^{-0.4}_{+0.1}$	$^{-0.2}_{+0.1}$	$^{+0.5}_{-0.5}$	0.94	1.00
1δ	$3.96 \cdot 10^{-1}$	17.1	7.4	−5.1	$^{+5.5}_{-4.2}$	$^{-0.1}_{-0.0}$	$^{-0.4}_{-0.3}$	$^{-0.3}_{+0.0}$	$^{+0.5}_{-0.5}$	0.94	1.00
2α	$1.98 \cdot 10^{1}$	3.3	3.3	+2.1	$^{+0.2}_{-0.2}$	$^{+1.2}_{-1.0}$	$^{-0.4}_{+0.6}$	$^{-0.4}_{+0.5}$	$^{+0.5}_{-0.5}$	0.95	1.00
2β	$1.15 \cdot 10^{1}$	5.1	3.9	+2.4	$^{+1.9}_{-2.1}$	$^{+0.4}_{-0.4}$	$^{-0.7}_{+0.6}$	$^{-0.3}_{+0.2}$	$^{+0.5}_{-0.5}$	0.96	1.00
2γ	$2.82 \cdot 10^{0}$	7.1	7.4	+6.1	$^{+3.6}_{-3.5}$	$^{-0.0}_{-0.3}$	$^{-0.1}_{+0.3}$	$^{-0.3}_{+0.3}$	$^{+0.5}_{-0.5}$	0.95	1.00
2δ	$4.03 \cdot 10^{-1}$	16.3	9.4	+6.8	$^{+6.6}_{-5.5}$	$^{+0.1}_{+0.2}$	$^{+0.5}_{+0.3}$	$^{-0.2}_{+0.4}$	$^{+0.5}_{-0.5}$	0.94	1.00
3α	$1.91 \cdot 10^{1}$	3.3	2.9	+1.4	$^{+0.3}_{-0.3}$	$^{+1.1}_{-1.0}$	$^{-0.6}_{+0.5}$	$^{-0.3}_{+0.3}$	$^{+0.4}_{-0.4}$	0.94	1.00
3β	$1.18 \cdot 10^{1}$	4.9	4.6	+3.3	$^{+2.0}_{-2.3}$	$^{+0.4}_{-0.4}$	$^{-0.6}_{+0.6}$	$^{-0.2}_{+0.2}$	$^{+0.4}_{-0.4}$	0.96	1.00
3γ	$3.68 \cdot 10^{0}$	5.6	4.4	+1.4	$^{+3.5}_{-3.4}$	$^{+0.1}_{-0.1}$	$^{-0.4}_{+0.2}$	$^{-0.2}_{+0.1}$	$^{+0.4}_{-0.4}$	0.95	1.00
3δ	$2.87 \cdot 10^{-1}$	23.3	6.7	−3.2	$^{+5.5}_{-5.5}$	$^{+0.1}_{-0.0}$	$^{-0.2}_{-0.1}$	$^{-0.2}_{+0.1}$	$^{+0.4}_{-0.4}$	0.95	1.00
4α	$1.68 \cdot 10^{1}$	3.6	2.6	+1.1	$^{+0.2}_{-0.3}$	$^{+0.8}_{-0.8}$	$^{-0.3}_{+0.3}$	$^{-0.2}_{+0.2}$	$^{+0.4}_{-0.4}$	0.93	1.00
4β	$1.12 \cdot 10^{1}$	5.0	4.5	+3.4	$^{+1.8}_{-2.1}$	$^{+0.4}_{-0.4}$	$^{-0.5}_{+0.7}$	$^{-0.1}_{+0.1}$	$^{+0.4}_{-0.4}$	0.96	1.00
4γ	$3.71 \cdot 10^{0}$	5.6	5.5	+3.9	$^{+3.3}_{-2.9}$	$^{+0.2}_{-0.1}$	$^{-0.2}_{+0.4}$	$^{-0.1}_{+0.1}$	$^{+0.3}_{-0.3}$	0.96	1.00
4δ	$3.99 \cdot 10^{-1}$	18.2	8.7	−5.9	$^{+6.0}_{-6.0}$	$^{+0.1}_{+0.1}$	$^{-0.2}_{+0.2}$	$^{+0.1}_{-0.1}$	$^{+0.2}_{-0.2}$	0.94	1.00
5α	$1.54 \cdot 10^{1}$	3.8	2.8	+1.0	$^{-0.3}_{+0.3}$	$^{+0.4}_{-0.3}$	$^{+0.5}_{-0.4}$	$^{-0.4}_{+0.4}$	$^{+1.2}_{-1.2}$	0.92	1.02
5β	$1.33 \cdot 10^{1}$	4.3	4.3	+3.2	$^{+1.5}_{-1.6}$	$^{+0.2}_{-0.2}$	$^{-0.3}_{+0.2}$	$^{-0.5}_{+0.4}$	$^{+1.1}_{-1.1}$	0.95	1.02
5γ	$4.71 \cdot 10^{0}$	5.1	5.6	+4.4	$^{+2.5}_{-2.3}$	$^{+0.2}_{-0.2}$	$^{-0.3}_{+0.3}$	$^{-0.3}_{+0.4}$	$^{+1.1}_{-1.1}$	0.97	1.03
5δ	$8.80 \cdot 10^{-1}$	10.5	7.0	+4.7	$^{+4.7}_{-4.4}$	$^{+0.1}_{-0.1}$	$^{-0.0}_{+0.2}$	$^{-0.1}_{+0.2}$	$^{+1.0}_{-1.0}$	0.96	1.01
6α	$8.32 \cdot 10^{-1}$	17.6	4.2	+2.8	$^{+0.5}_{+0.1}$	$^{+0.6}_{-0.4}$	$^{+0.1}_{+0.4}$	$^{-0.5}_{+0.8}$	$^{+2.1}_{-2.1}$	0.91	1.11
6β	$7.02 \cdot 10^{-1}$	19.9	4.4	+3.2	$^{+1.1}_{-0.9}$	$^{+0.4}_{-0.2}$	$^{+0.8}_{+0.1}$	$^{-0.2}_{+0.6}$	$^{+1.9}_{-1.9}$	0.94	1.11
6γ	$4.25 \cdot 10^{-1}$	15.0	4.9	−3.2	$^{+2.1}_{-2.4}$	$^{+0.2}_{-0.1}$	$^{+0.3}_{-0.4}$	$^{-0.6}_{+0.7}$	$^{+1.9}_{-1.9}$	0.96	1.11
6δ	$1.24 \cdot 10^{-1}$	27.0	8.3	−7.3	$^{+2.9}_{-2.7}$	$^{+0.1}_{-0.3}$	$^{+0.4}_{+0.3}$	$^{-0.1}_{+0.3}$	$^{+1.8}_{-1.8}$	0.97	1.11

Table 14: Double-differential dijet cross sections measured as a function of Q^2 and $\langle P_T \rangle_2$ using the anti$-k_T$ jet algorithm. The uncertainties δ^{had} are identical to those in table 9 and are not repeated here. Further details are given in the caption of table 9.

Dijet cross sections in bins of Q^2 and ξ_2 using the anti$-k_{\mathrm{T}}$ jet algorithm

Bin label	σ [pb]	δ^{stat} [%]	δ^{sys} [%]	δ^{Model} [%]	δ^{JES} [%]	δ^{RCES} [%]	$\delta^{E'_e}$ [%]	δ^{θ_e} [%]	$\delta^{\mathrm{ID(e)}}$ [%]	c^{had}	c^{ew}
1a	$2.16 \cdot 10^{1}$	3.0	9.5	+9.0	$^{+1.0}_{-1.1}$	$^{+1.4}_{-1.4}$	$^{+0.1}_{-0.2}$	$^{-0.3}_{+0.3}$	$^{+0.5}_{-0.5}$	0.96	1.00
1b	$1.86 \cdot 10^{1}$	3.1	4.3	+3.2	$^{+1.3}_{-1.5}$	$^{+1.0}_{-1.1}$	$^{+0.3}_{-0.5}$	$^{-0.3}_{+0.2}$	$^{+0.5}_{-0.5}$	0.95	1.00
1c	$6.08 \cdot 10^{0}$	6.5	9.1	−8.5	$^{+2.3}_{-2.1}$	$^{+0.2}_{-0.2}$	$^{+0.2}_{+0.2}$	$^{-0.2}_{+0.2}$	$^{+0.5}_{-0.5}$	0.92	1.00
1d	$1.75 \cdot 10^{0}$	8.9	7.7	+6.5	$^{+3.1}_{-3.5}$	$^{-0.0}_{-0.0}$	$^{-1.4}_{+0.9}$	$^{-0.4}_{+0.2}$	$^{+0.5}_{-0.5}$	0.90	1.00
2a	$1.46 \cdot 10^{1}$	5.3	10.3	+10.0	$^{+0.8}_{-0.7}$	$^{+1.2}_{-1.2}$	$^{-0.1}_{+0.2}$	$^{-0.4}_{+0.5}$	$^{+0.5}_{-0.5}$	0.96	1.00
2b	$1.64 \cdot 10^{1}$	3.3	3.9	+2.6	$^{+1.2}_{-1.3}$	$^{+1.0}_{-1.0}$	$^{+0.7}_{-0.6}$	$^{-0.3}_{+0.3}$	$^{+0.5}_{-0.5}$	0.95	1.00
2c	$5.84 \cdot 10^{0}$	6.0	4.2	+2.6	$^{+2.3}_{-2.2}$	$^{+0.3}_{-0.3}$	$^{+0.1}_{-0.0}$	$^{-0.3}_{+0.4}$	$^{+0.5}_{-0.5}$	0.93	1.00
2d	$1.63 \cdot 10^{0}$	8.8	6.3	+4.9	$^{+3.4}_{-2.8}$	$^{-0.0}_{+0.2}$	$^{-0.7}_{+1.3}$	$^{-0.2}_{+0.4}$	$^{+0.5}_{-0.5}$	0.91	1.00
3a	$1.14 \cdot 10^{1}$	4.0	9.2	+8.9	$^{+0.7}_{-0.8}$	$^{+1.1}_{-1.0}$	$^{-0.2}_{+0.2}$	$^{-0.2}_{+0.2}$	$^{+0.4}_{-0.4}$	0.95	1.00
3b	$1.84 \cdot 10^{1}$	2.8	4.3	+3.3	$^{+1.2}_{-1.2}$	$^{+0.9}_{-0.9}$	$^{+0.4}_{-0.5}$	$^{-0.3}_{+0.3}$	$^{+0.5}_{-0.5}$	0.95	1.00
3c	$7.83 \cdot 10^{0}$	4.6	3.4	−1.6	$^{+1.8}_{-2.0}$	$^{+0.3}_{-0.4}$	$^{+0.3}_{-0.3}$	$^{-0.2}_{+0.2}$	$^{+0.4}_{-0.4}$	0.93	1.00
3d	$1.96 \cdot 10^{0}$	7.8	5.9	−4.3	$^{+3.2}_{-3.3}$	$^{-0.1}_{+0.0}$	$^{-0.8}_{+0.4}$	$^{-0.4}_{+0.1}$	$^{+0.4}_{-0.4}$	0.92	1.00
4a	$5.21 \cdot 10^{0}$	7.5	4.4	+3.7	$^{+0.7}_{-0.6}$	$^{+0.8}_{-0.9}$	$^{+0.5}_{-0.4}$	$^{-0.1}_{+0.2}$	$^{+0.2}_{-0.2}$	0.94	1.00
4b	$1.81 \cdot 10^{1}$	3.0	4.1	+3.1	$^{+1.1}_{-1.0}$	$^{+0.8}_{-0.8}$	$^{+0.3}_{-0.3}$	$^{-0.1}_{+0.1}$	$^{+0.4}_{-0.4}$	0.95	1.00
4c	$1.16 \cdot 10^{1}$	3.5	7.0	+6.4	$^{+1.3}_{-1.4}$	$^{+0.5}_{-0.6}$	$^{+0.6}_{-0.9}$	$^{-0.1}_{+0.1}$	$^{+0.4}_{-0.4}$	0.94	1.00
4d	$2.41 \cdot 10^{0}$	7.4	14.9	+14.4	$^{+3.2}_{-3.2}$	$^{+0.1}_{-0.1}$	$^{-0.3}_{+0.4}$	$^{+0.0}_{+0.1}$	$^{+0.4}_{-0.4}$	0.93	1.00
5b	$9.13 \cdot 10^{0}$	3.4	4.1	+3.1	$^{+0.7}_{-0.8}$	$^{+0.5}_{-0.5}$	$^{+0.0}_{-0.0}$	$^{-0.5}_{+0.4}$	$^{+1.1}_{-1.1}$	0.94	1.01
5c	$1.73 \cdot 10^{1}$	2.7	8.7	+8.2	$^{+0.8}_{-0.9}$	$^{+0.5}_{-0.6}$	$^{+0.5}_{-0.4}$	$^{-0.3}_{+0.3}$	$^{+1.1}_{-1.1}$	0.94	1.02
5d	$1.12 \cdot 10^{1}$	2.9	10.5	+10.1	$^{+1.3}_{-1.3}$	$^{+0.3}_{-0.3}$	$^{-0.0}_{-0.2}$	$^{-0.4}_{+0.3}$	$^{+1.1}_{-1.1}$	0.93	1.03
6d	$1.87 \cdot 10^{0}$	7.1	8.4	+7.8	$^{+0.5}_{-0.8}$	$^{+0.3}_{-0.3}$	$^{+0.8}_{-1.0}$	$^{-0.4}_{+0.2}$	$^{+1.9}_{-1.9}$	0.93	1.11

Table 15: Double-differential dijet cross sections measured as a function of Q^2 and ξ_2 using the anti$-k_{\mathrm{T}}$ jet algorithm. The uncertainties δ^{had} are identical to those in table 10 and are not repeated here. Further details are given in the caption of table 10.

Trijet cross sections in bins of Q^2 and $\langle P_T \rangle_3$ using the anti$-k_T$ jet algorithm

Bin label	σ [pb]	δ^{stat} [%]	δ^{sys} [%]	δ^{Model} [%]	δ^{JES} [%]	δ^{RCES} [%]	$\delta^{E'_e}$ [%]	δ^{θ_e} [%]	$\delta^{\text{ID(e)}}$ [%]	c^{had}	c^{ew}
1α	$4.21 \cdot 10^{0}$	8.9	7.1	+5.6	$^{-0.8}_{+0.6}$	$^{+3.4}_{-3.8}$	$^{-0.2}_{+0.2}$	$^{-0.4}_{+0.3}$	$^{+0.4}_{-0.4}$	0.75	1.00
1β	$2.57 \cdot 10^{0}$	8.2	6.0	+4.4	$^{+3.2}_{-3.2}$	$^{+1.2}_{-1.0}$	$^{+0.4}_{-0.1}$	$^{-0.4}_{+0.3}$	$^{+0.5}_{-0.5}$	0.78	1.00
1γ	$3.10 \cdot 10^{-1}$	24.0	19.2	+18.4	$^{+4.8}_{-4.7}$	$^{+0.2}_{-0.9}$	$^{-1.2}_{+0.3}$	$^{+0.1}_{-0.3}$	$^{+0.5}_{-0.5}$	0.81	1.00
2α	$3.12 \cdot 10^{0}$	10.0	6.1	+4.3	$^{-0.5}_{+1.3}$	$^{+3.6}_{-3.5}$	$^{-0.2}_{+0.6}$	$^{-0.3}_{+0.4}$	$^{+0.5}_{-0.5}$	0.74	1.00
2β	$1.77 \cdot 10^{0}$	9.7	6.2	+4.8	$^{+2.5}_{-3.3}$	$^{+1.2}_{-1.5}$	$^{-0.4}_{-0.4}$	$^{-0.3}_{+0.1}$	$^{+0.5}_{-0.5}$	0.78	1.00
2γ	$4.11 \cdot 10^{-1}$	17.6	9.4	+7.8	$^{+5.3}_{-3.4}$	$^{+0.8}_{-0.4}$	$^{+1.6}_{+0.0}$	$^{-0.7}_{+0.8}$	$^{+0.5}_{-0.5}$	0.81	1.00
3α	$3.39 \cdot 10^{0}$	9.2	5.1	+3.0	$^{-0.7}_{+1.0}$	$^{+3.3}_{-3.3}$	$^{-0.4}_{+1.1}$	$^{-0.0}_{+0.2}$	$^{+0.4}_{-0.4}$	0.73	1.00
3β	$2.11 \cdot 10^{0}$	8.7	9.0	+8.2	$^{+2.4}_{-2.9}$	$^{+1.4}_{-1.4}$	$^{-0.4}_{+0.2}$	$^{-0.1}_{+0.3}$	$^{+0.4}_{-0.4}$	0.78	1.00
3γ	$5.36 \cdot 10^{-1}$	14.8	6.7	+2.3	$^{+5.9}_{-5.6}$	$^{+0.4}_{-0.7}$	$^{-1.4}_{+0.3}$	$^{+0.1}_{-0.6}$	$^{+0.4}_{-0.4}$	0.80	1.00
4α	$2.56 \cdot 10^{0}$	11.0	3.8	−0.8	$^{-1.0}_{+0.7}$	$^{+2.6}_{-2.8}$	$^{-0.3}_{-0.1}$	$^{-0.3}_{+0.2}$	$^{+0.3}_{-0.3}$	0.73	1.00
4β	$2.49 \cdot 10^{0}$	7.4	10.0	+9.3	$^{+2.7}_{-2.4}$	$^{+1.7}_{-1.5}$	$^{-0.6}_{+0.9}$	$^{+0.0}_{-0.0}$	$^{+0.3}_{-0.3}$	0.78	1.00
4γ	$6.53 \cdot 10^{-1}$	14.0	12.0	+10.1	$^{+5.8}_{-5.9}$	$^{+0.6}_{-0.9}$	$^{-0.2}_{+0.6}$	$^{-0.1}_{+0.4}$	$^{+0.1}_{-0.1}$	0.80	1.00
5α	$2.62 \cdot 10^{0}$	10.2	3.9	−1.2	$^{-1.3}_{+1.2}$	$^{+1.8}_{-2.1}$	$^{+1.1}_{-0.7}$	$^{-0.3}_{+0.3}$	$^{+1.4}_{-1.4}$	0.71	1.03
5β	$2.58 \cdot 10^{0}$	7.4	8.8	+8.2	$^{+1.6}_{-1.6}$	$^{+1.2}_{-1.0}$	$^{-0.1}_{+0.2}$	$^{-0.3}_{+0.4}$	$^{+1.3}_{-1.3}$	0.77	1.03
5γ	$5.64 \cdot 10^{-1}$	18.6	23.2	+22.6	$^{+4.5}_{-4.5}$	$^{+0.7}_{-0.9}$	$^{-1.1}_{+0.9}$	$^{-0.1}_{+0.1}$	$^{+1.1}_{-1.1}$	0.79	1.03
6β	$1.30 \cdot 10^{-1}$	33.1	11.4	+10.8	$^{+1.2}_{-1.6}$	$^{+1.4}_{-0.5}$	$^{+0.9}_{-0.5}$	$^{-0.5}_{+0.5}$	$^{+2.2}_{-2.2}$	0.74	1.12

Table 16: Double-differential trijet cross sections measured as a function of Q^2 and $\langle P_T \rangle_3$ using the anti$-k_T$ jet algorithm. The uncertainties δ^{had} are identical to those in table 11 and are not repeated here. Further details are given in the caption of table 11.

Trijet cross sections in bins of Q^2 and ξ_3 using the anti$-k_T$ jet algorithm

Bin label	σ [pb]	δ^{stat} [%]	δ^{sys} [%]	δ^{Model} [%]	δ^{JES} [%]	δ^{RCES} [%]	$\delta^{E'_e}$ [%]	δ^{θ_e} [%]	$\delta^{\mathrm{ID(e)}}$ [%]	c^{had}	c^{ew}
1A	$2.71 \cdot 10^{0}$	11.5	18.3	+17.7	$^{-0.2}_{+0.2}$	$^{+4.0}_{-3.9}$	$^{+0.5}_{-0.9}$	$^{-0.4}_{+0.3}$	$^{+0.5}_{-0.5}$	0.76	1.00
1B	$3.04 \cdot 10^{0}$	9.0	14.0	+13.7	$^{+1.2}_{-1.4}$	$^{+1.6}_{-1.6}$	$^{-0.2}_{+0.3}$	$^{-0.3}_{+0.2}$	$^{+0.4}_{-0.4}$	0.76	1.00
1C	$1.00 \cdot 10^{0}$	13.5	16.2	−15.4	$^{+4.2}_{-4.5}$	$^{+0.5}_{-0.8}$	$^{+0.5}_{-0.6}$	$^{-0.1}_{+0.4}$	$^{+0.4}_{-0.4}$	0.74	1.00
2A	$1.68 \cdot 10^{0}$	16.6	17.8	+17.2	$^{+0.6}_{-0.2}$	$^{+4.0}_{-3.5}$	$^{+1.1}_{-1.0}$	$^{-0.4}_{+0.4}$	$^{+0.5}_{-0.5}$	0.75	1.00
2B	$2.56 \cdot 10^{0}$	9.7	12.5	+12.1	$^{+0.9}_{-1.0}$	$^{+1.6}_{-1.6}$	$^{+0.1}_{-0.1}$	$^{-0.3}_{+0.3}$	$^{+0.5}_{-0.5}$	0.76	1.00
2C	$8.13 \cdot 10^{-1}$	14.7	46.8	−46.6	$^{+4.4}_{-4.2}$	$^{+0.7}_{-0.7}$	$^{+1.0}_{-1.3}$	$^{-0.5}_{+0.3}$	$^{+0.4}_{-0.4}$	0.74	1.00
3A	$1.47 \cdot 10^{0}$	16.1	19.5	+19.0	$^{-0.2}_{+0.1}$	$^{+3.7}_{-3.2}$	$^{+1.4}_{-0.7}$	$^{+0.0}_{+0.0}$	$^{+0.4}_{-0.4}$	0.75	1.00
3B	$3.07 \cdot 10^{0}$	8.4	18.2	+17.9	$^{+1.2}_{-0.6}$	$^{+2.0}_{-2.2}$	$^{+0.2}_{-0.1}$	$^{-0.2}_{+0.3}$	$^{+0.4}_{-0.4}$	0.76	1.00
3C	$1.14 \cdot 10^{0}$	11.7	11.0	−10.1	$^{+3.3}_{-4.1}$	$^{+0.6}_{-0.5}$	$^{+0.2}_{-0.4}$	$^{-0.1}_{+0.0}$	$^{+0.4}_{-0.4}$	0.74	1.00
4A	$1.28 \cdot 10^{0}$	15.9	17.1	+16.7	$^{-0.5}_{-0.3}$	$^{+2.3}_{-2.4}$	$^{+1.0}_{-1.8}$	$^{-0.3}_{+0.1}$	$^{+0.2}_{-0.2}$	0.73	1.00
4B	$2.68 \cdot 10^{0}$	9.4	20.0	−19.7	$^{+0.5}_{-0.1}$	$^{+2.0}_{-2.0}$	$^{+0.6}_{-0.5}$	$^{+0.1}_{+0.1}$	$^{+0.4}_{-0.4}$	0.76	1.00
4C	$1.66 \cdot 10^{0}$	9.1	17.1	−16.6	$^{+3.1}_{-3.4}$	$^{+0.7}_{-0.8}$	$^{+0.5}_{-0.5}$	$^{-0.1}_{-0.0}$	$^{+0.3}_{-0.3}$	0.75	1.00
5B	$2.52 \cdot 10^{0}$	9.1	9.2	+8.7	$^{-0.0}_{+0.2}$	$^{+1.3}_{-1.4}$	$^{+0.4}_{-0.2}$	$^{-0.5}_{+0.6}$	$^{+1.4}_{-1.4}$	0.75	1.02
5C	$2.88 \cdot 10^{0}$	7.1	51.6	−51.6	$^{+1.3}_{-1.4}$	$^{+1.2}_{-1.2}$	$^{+0.4}_{-0.2}$	$^{-0.1}_{+0.1}$	$^{+1.2}_{-1.2}$	0.75	1.03
6C	$3.04 \cdot 10^{-1}$	17.8	92.8	−92.7	$^{+0.6}_{-0.4}$	$^{+1.2}_{-0.9}$	$^{+1.1}_{-1.0}$	$^{+0.0}_{+0.1}$	$^{+2.3}_{-2.3}$	0.73	1.11

Table 17: Double-differential normalised trijet cross sections measured as a function of Q^2 and ξ_3 using the anti$-k_T$ jet algorithm. The uncertainties δ^{had} are identical to those in table 12 and are not repeated here. Further details are given in the caption of table 12.

Normalised inclusive jet cross sections in bins of Q^2 and $P_{\mathrm{T}}^{\mathrm{jet}}$ using the k_{T} jet algorithm

Bin label	$\sigma/\sigma_{\mathrm{NC}}$	δ^{stat} [%]	δ^{sys} [%]	δ^{Model} [%]	δ^{JES} [%]	δ^{RCES} [%]	$\delta^{E'_e}$ [%]	δ^{θ_e} [%]	c^{had}	δ^{had} [%]
1α	$1.63 \cdot 10^{-1}$	2.7	1.1	−0.6	$^{+0.6}_{-0.8}$	$^{+0.3}_{-0.3}$	$^{-0.4}_{+0.3}$	$^{+0.1}_{-0.1}$	0.93	2.2
1β	$7.16 \cdot 10^{-2}$	4.1	3.0	+2.0	$^{+2.0}_{-2.2}$	$^{-0.1}_{+0.2}$	$^{-0.7}_{+0.5}$	$^{+0.2}_{-0.3}$	0.97	1.7
1γ	$1.87 \cdot 10^{-2}$	6.4	4.2	+2.9	$^{+3.0}_{-3.0}$	$^{-0.3}_{+0.6}$	$^{-0.4}_{+0.5}$	$^{+0.3}_{-0.4}$	0.96	1.1
1δ	$2.10 \cdot 10^{-3}$	15.3	11.9	+10.9	$^{+4.5}_{-4.9}$	$^{-0.5}_{+0.6}$	$^{-0.1}_{-0.5}$	$^{+0.2}_{-0.5}$	0.95	0.7
2α	$1.73 \cdot 10^{-1}$	2.9	1.7	−1.2	$^{+0.5}_{-0.6}$	$^{+0.6}_{-0.4}$	$^{-0.6}_{+0.9}$	$^{+0.1}_{-0.1}$	0.93	2.1
2β	$8.44 \cdot 10^{-2}$	4.1	3.3	+2.4	$^{+2.0}_{-2.0}$	$^{-0.2}_{+0.2}$	$^{-0.7}_{+0.6}$	$^{+0.2}_{-0.2}$	0.97	1.7
2γ	$2.21 \cdot 10^{-2}$	6.6	5.2	+4.1	$^{+3.3}_{-3.0}$	$^{-0.3}_{+0.4}$	$^{-0.6}_{+0.5}$	$^{+0.1}_{-0.2}$	0.97	1.3
2δ	$2.70 \cdot 10^{-3}$	15.2	6.3	+3.9	$^{+5.3}_{-4.4}$	$^{-0.7}_{+0.5}$	$^{-0.0}_{+0.1}$	$^{+0.2}_{-0.2}$	0.96	1.2
3α	$1.90 \cdot 10^{-1}$	3.0	1.4	+0.6	$^{+0.4}_{-0.5}$	$^{+0.6}_{-0.6}$	$^{-1.0}_{+0.7}$	$^{+0.1}_{-0.1}$	0.93	1.5
3β	$1.01 \cdot 10^{-1}$	4.0	3.0	+2.2	$^{+1.9}_{-1.8}$	$^{+0.1}_{-0.1}$	$^{-0.7}_{+0.9}$	$^{+0.2}_{-0.1}$	0.97	1.1
3γ	$2.54 \cdot 10^{-2}$	6.8	3.6	+1.4	$^{+3.0}_{-3.2}$	$^{-0.2}_{+0.2}$	$^{-1.0}_{+0.6}$	$^{+0.3}_{-0.7}$	0.97	0.9
3δ	$3.20 \cdot 10^{-3}$	15.1	6.3	−3.7	$^{+4.9}_{-5.2}$	$^{-0.4}_{+0.1}$	$^{+0.8}_{-0.3}$	$^{+0.3}_{+0.0}$	0.95	0.5
4α	$2.23 \cdot 10^{-1}$	3.2	1.6	+0.5	$^{+0.7}_{-0.8}$	$^{+0.5}_{-0.5}$	$^{-1.1}_{+1.2}$	$^{+0.0}_{-0.0}$	0.93	1.2
4β	$1.23 \cdot 10^{-1}$	4.1	1.7	+0.3	$^{+1.4}_{-1.4}$	$^{+0.2}_{-0.2}$	$^{-0.6}_{+0.7}$	$^{+0.1}_{-0.1}$	0.97	1.0
4γ	$3.63 \cdot 10^{-2}$	6.1	4.1	+2.5	$^{+3.3}_{-3.0}$	$^{-0.0}_{-0.2}$	$^{-0.8}_{+0.8}$	$^{+0.1}_{-0.1}$	0.97	0.5
4δ	$3.90 \cdot 10^{-3}$	16.5	11.2	−9.9	$^{+5.1}_{-4.9}$	$^{-0.3}_{+0.1}$	$^{-0.0}_{-0.2}$	$^{+0.3}_{-0.4}$	0.96	0.4
5α	$2.41 \cdot 10^{-1}$	3.4	1.2	+0.5	$^{+0.5}_{-0.6}$	$^{+0.4}_{-0.4}$	$^{-0.6}_{+0.6}$	$^{-0.0}_{+0.0}$	0.92	0.9
5β	$1.59 \cdot 10^{-1}$	3.9	1.7	−0.9	$^{+1.1}_{-1.0}$	$^{+0.1}_{-0.1}$	$^{-0.6}_{+0.8}$	$^{-0.2}_{+0.1}$	0.97	0.5
5γ	$5.96 \cdot 10^{-2}$	4.8	2.6	+1.0	$^{+2.2}_{-2.3}$	$^{+0.1}_{-0.1}$	$^{-0.7}_{+0.7}$	$^{+0.1}_{-0.1}$	0.97	0.4
5δ	$1.14 \cdot 10^{-2}$	8.5	4.3	+0.9	$^{+4.3}_{-4.0}$	$^{+0.0}_{+0.0}$	$^{-0.5}_{+0.5}$	$^{+0.3}_{-0.3}$	0.96	0.3
6α	$3.04 \cdot 10^{-1}$	14.5	5.9	−5.8	$^{+0.2}_{-0.3}$	$^{+0.3}_{-0.5}$	$^{-1.1}_{-1.0}$	$^{-0.0}_{+0.3}$	0.91	0.6
6β	$2.04 \cdot 10^{-1}$	16.3	2.9	−2.5	$^{+1.0}_{-0.6}$	$^{+0.1}_{+0.0}$	$^{-0.3}_{+1.8}$	$^{-0.1}_{+0.5}$	0.96	0.6
6γ	$7.84 \cdot 10^{-2}$	21.5	15.7	−15.6	$^{+1.7}_{-1.4}$	$^{+0.2}_{-0.3}$	$^{-0.7}_{+0.6}$	$^{-0.2}_{+0.3}$	0.99	1.1
6δ	$3.61 \cdot 10^{-2}$	19.5	22.4	−22.3	$^{+2.4}_{-2.3}$	$^{+0.0}_{+0.0}$	$^{-0.2}_{-0.4}$	$^{+0.3}_{-0.2}$	0.98	0.8

Table 18: Double-differential normalised inclusive jet cross sections measured as a function of Q^2 and $P_{\mathrm{T}}^{\mathrm{jet}}$ using the k_{T} jet algorithm. The total systematic uncertainty, δ^{sys}, sums all systematic uncertainties in quadrature, including the uncertainty due to the LAr noise of $\delta^{\mathrm{LArNoise}} = 0.5\,\%$. Further details are given in the caption of table 8.

Normalised dijet cross sections in bins of Q^2 and $\langle P_{\mathrm{T}} \rangle_2$ using the k_{T} jet algorithm

Bin label	$\sigma/\sigma_{\mathrm{NC}}$	δ^{stat} [%]	δ^{sys} [%]	δ^{Model} [%]	δ^{JES} [%]	δ^{RCES} [%]	$\delta^{E'_e}$ [%]	δ^{θ_e} [%]	c^{had}	δ^{had} [%]
1α	$5.42 \cdot 10^{-2}$	3.6	1.8	+1.5	$^{-0.2}_{+0.1}$	$^{+0.6}_{-0.5}$	$^{-0.5}_{+0.3}$	$^{+0.1}_{-0.2}$	0.94	2.0
1β	$3.13 \cdot 10^{-2}$	5.8	3.1	+2.6	$^{+1.4}_{-1.5}$	$^{-0.4}_{+0.4}$	$^{-0.1}_{+0.3}$	$^{+0.2}_{-0.1}$	0.97	1.4
1γ	$8.30 \cdot 10^{-3}$	6.6	5.0	+3.3	$^{+3.7}_{-3.5}$	$^{-0.4}_{+0.7}$	$^{-0.4}_{+0.2}$	$^{+0.3}_{-0.4}$	0.96	1.0
1δ	$1.00 \cdot 10^{-3}$	16.4	8.7	+7.2	$^{+5.0}_{-4.5}$	$^{-0.6}_{+0.8}$	$^{-0.6}_{-0.4}$	$^{+0.3}_{-0.6}$	0.96	1.2
2α	$5.71 \cdot 10^{-2}$	4.0	1.8	+1.4	$^{-0.3}_{+0.4}$	$^{+0.8}_{-0.6}$	$^{-0.4}_{+0.6}$	$^{+0.1}_{-0.0}$	0.94	1.7
2β	$3.92 \cdot 10^{-2}$	5.5	2.6	+1.6	$^{+1.6}_{-2.0}$	$^{-0.2}_{+0.2}$	$^{-0.7}_{+0.7}$	$^{+0.2}_{-0.1}$	0.98	1.6
2γ	$9.30 \cdot 10^{-3}$	7.4	4.4	+3.0	$^{+3.3}_{-3.0}$	$^{-0.5}_{+0.4}$	$^{-0.2}_{+0.1}$	$^{+0.2}_{-0.3}$	0.97	1.0
2δ	$1.20 \cdot 10^{-3}$	18.1	12.5	+11.5	$^{+5.8}_{-3.9}$	$^{-0.8}_{+0.5}$	$^{-0.1}_{+0.1}$	$^{+0.1}_{-0.3}$	0.95	1.9
3α	$6.66 \cdot 10^{-2}$	3.9	1.4	+0.6	$^{-0.5}_{+0.5}$	$^{+0.8}_{-0.7}$	$^{-0.5}_{+0.6}$	$^{+0.1}_{-0.1}$	0.93	1.2
3β	$4.11 \cdot 10^{-2}$	6.1	3.4	+2.8	$^{+1.7}_{-1.7}$	$^{-0.0}_{+0.1}$	$^{-0.6}_{+0.5}$	$^{+0.1}_{-0.1}$	0.98	0.9
3γ	$1.38 \cdot 10^{-2}$	5.9	3.1	+0.5	$^{+2.9}_{-3.1}$	$^{-0.3}_{+0.3}$	$^{-0.4}_{+0.1}$	$^{+0.2}_{-0.4}$	0.97	0.8
3δ	$1.30 \cdot 10^{-3}$	20.5	9.5	−8.0	$^{+4.4}_{-5.9}$	$^{-0.4}_{+0.1}$	$^{-0.2}_{-0.6}$	$^{+0.1}_{-0.5}$	0.96	0.4
4α	$7.61 \cdot 10^{-2}$	4.1	1.3	−0.7	$^{-0.4}_{+0.6}$	$^{+0.7}_{-0.6}$	$^{-0.2}_{+0.3}$	$^{+0.1}_{-0.0}$	0.92	1.1
4β	$4.95 \cdot 10^{-2}$	6.3	3.0	+2.5	$^{+1.3}_{-1.6}$	$^{+0.1}_{-0.2}$	$^{-0.5}_{+0.5}$	$^{+0.1}_{-0.1}$	0.97	0.9
4γ	$1.67 \cdot 10^{-2}$	6.2	3.1	+1.3	$^{+2.7}_{-2.7}$	$^{-0.1}_{+0.2}$	$^{-0.3}_{+0.3}$	$^{+0.1}_{-0.1}$	0.98	0.5
4δ	$1.70 \cdot 10^{-3}$	20.4	6.6	−4.2	$^{+4.9}_{-5.2}$	$^{-0.2}_{+0.2}$	$^{-0.3}_{+0.3}$	$^{+0.2}_{-0.3}$	0.96	0.3
5α	$8.27 \cdot 10^{-2}$	4.4	1.8	−1.2	$^{-0.9}_{+1.0}$	$^{+0.5}_{-0.5}$	$^{+0.6}_{-0.5}$	$^{+0.1}_{-0.1}$	0.92	0.6
5β	$7.37 \cdot 10^{-2}$	5.1	1.6	+1.0	$^{+1.0}_{-1.0}$	$^{+0.1}_{-0.1}$	$^{-0.5}_{+0.4}$	$^{+0.0}_{+0.0}$	0.96	0.3
5γ	$2.66 \cdot 10^{-2}$	5.4	3.9	+3.3	$^{+2.0}_{-2.0}$	$^{+0.1}_{-0.0}$	$^{-0.4}_{+0.5}$	$^{+0.1}_{-0.1}$	0.98	0.4
5δ	$5.30 \cdot 10^{-3}$	10.3	4.3	+0.9	$^{+4.2}_{-4.0}$	$^{-0.0}_{+0.2}$	$^{-0.5}_{+0.2}$	$^{+0.3}_{-0.4}$	0.96	0.7
6α	$8.53 \cdot 10^{-2}$	22.9	5.1	−4.9	$^{-0.9}_{+1.3}$	$^{+0.1}_{-0.5}$	$^{+0.5}_{-0.9}$	$^{+0.2}_{+0.4}$	0.89	0.2
6β	$9.88 \cdot 10^{-2}$	20.0	7.2	+6.8	$^{+2.2}_{-0.1}$	$^{+0.2}_{-0.1}$	$^{-0.7}_{+3.0}$	$^{-0.1}_{+1.5}$	0.95	0.5
6γ	$4.08 \cdot 10^{-2}$	19.2	7.0	−6.8	$^{+0.8}_{-2.1}$	$^{+0.2}_{-0.4}$	$^{-0.5}_{-0.6}$	$^{-0.9}_{-0.0}$	0.97	0.8
6δ	$1.72 \cdot 10^{-2}$	26.7	9.8	−9.6	$^{+2.5}_{-1.2}$	$^{-0.0}_{+0.2}$	$^{+1.2}_{+0.2}$	$^{+1.3}_{-0.6}$	0.98	1.0

Table 19: Double-differential normalised dijet cross sections measured as a function of Q^2 and $\langle P_{\mathrm{T}} \rangle_2$ using the k_{T} jet algorithm. The total systematic uncertainty, δ^{sys}, sums all systematic uncertainties in quadrature, including the uncertainty due to the LAr noise of $\delta^{\mathrm{LArNoise}} = 0.6\,\%$. Further details are given in the caption of table 9.

Normalised dijet cross sections in bins of Q^2 and ξ_2 using the k_T jet algorithm

Bin label	σ/σ_{NC}	δ^{stat} [%]	δ^{sys} [%]	δ^{Model} [%]	δ^{JES} [%]	δ^{RCES} [%]	$\delta^{E'_e}$ [%]	δ^{θ_e} [%]	c^{had}	δ^{had} [%]
1a	$4.72 \cdot 10^{-2}$	4.2	6.7	+6.5	$^{+0.6}_{-0.7}$	$^{+1.0}_{-1.0}$	$^{+0.2}_{-0.4}$	$^{+0.1}_{-0.2}$	0.94	2.1
1b	$4.23 \cdot 10^{-2}$	3.4	3.1	+2.7	$^{+0.9}_{-1.0}$	$^{+0.6}_{-0.6}$	$^{+0.2}_{-0.2}$	$^{+0.3}_{-0.3}$	0.94	1.7
1c	$1.39 \cdot 10^{-2}$	7.0	2.7	+1.7	$^{+2.1}_{-1.8}$	$^{-0.2}_{+0.3}$	$^{+0.2}_{-0.1}$	$^{+0.1}_{-0.2}$	0.94	1.3
1d	$4.60 \cdot 10^{-3}$	8.8	6.9	+6.0	$^{+3.1}_{-2.7}$	$^{-0.6}_{+0.5}$	$^{-1.7}_{+1.4}$	$^{+0.3}_{-0.3}$	0.92	0.7
2a	$4.59 \cdot 10^{-2}$	4.9	3.7	+3.5	$^{+0.3}_{-0.4}$	$^{+0.9}_{-0.9}$	$^{+0.0}_{+0.1}$	$^{+0.2}_{-0.1}$	0.94	1.8
2b	$4.99 \cdot 10^{-2}$	3.5	2.5	+2.0	$^{+0.6}_{-0.8}$	$^{+0.7}_{-0.7}$	$^{+0.6}_{-0.7}$	$^{+0.1}_{-0.1}$	0.94	1.7
2c	$1.95 \cdot 10^{-2}$	6.3	2.4	−1.0	$^{+2.0}_{-2.1}$	$^{-0.2}_{+0.2}$	$^{+0.3}_{-0.2}$	$^{+0.2}_{-0.2}$	0.94	1.1
2d	$5.40 \cdot 10^{-3}$	9.4	5.9	+5.2	$^{+2.7}_{-2.3}$	$^{-0.6}_{+0.6}$	$^{-1.1}_{+1.1}$	$^{+0.1}_{+0.0}$	0.93	0.6
3a	$4.10 \cdot 10^{-2}$	4.1	4.3	+4.2	$^{+0.3}_{-0.3}$	$^{+0.9}_{-0.9}$	$^{-0.2}_{+0.1}$	$^{+0.1}_{-0.1}$	0.93	1.4
3b	$6.40 \cdot 10^{-2}$	3.0	2.5	+2.1	$^{+0.5}_{-0.6}$	$^{+0.7}_{-0.7}$	$^{+0.5}_{-0.6}$	$^{+0.1}_{-0.1}$	0.94	1.2
3c	$3.02 \cdot 10^{-2}$	4.6	2.1	−1.2	$^{+1.5}_{-1.6}$	$^{+0.1}_{-0.1}$	$^{+0.3}_{-0.3}$	$^{+0.2}_{-0.1}$	0.94	0.9
3d	$7.20 \cdot 10^{-3}$	8.3	4.0	+2.7	$^{+3.0}_{-2.9}$	$^{-0.4}_{+0.3}$	$^{-0.6}_{+0.3}$	$^{-0.1}_{-0.2}$	0.94	0.4
4a	$2.34 \cdot 10^{-2}$	7.7	7.3	+7.2	$^{-0.1}_{-0.3}$	$^{+0.7}_{-0.8}$	$^{+0.4}_{-0.4}$	$^{-0.0}_{-0.0}$	0.92	1.4
4b	$8.14 \cdot 10^{-2}$	3.2	3.8	+3.6	$^{+0.3}_{-0.5}$	$^{+0.6}_{-0.7}$	$^{+0.1}_{-0.2}$	$^{+0.1}_{-0.1}$	0.93	1.2
4c	$5.11 \cdot 10^{-2}$	3.7	2.0	−1.4	$^{+1.0}_{-1.0}$	$^{+0.4}_{-0.4}$	$^{+0.7}_{-0.8}$	$^{+0.1}_{-0.1}$	0.94	0.8
4d	$1.08 \cdot 10^{-2}$	8.2	5.4	+4.7	$^{+2.8}_{-2.7}$	$^{-0.1}_{+0.1}$	$^{-0.0}_{+0.4}$	$^{+0.2}_{-0.1}$	0.95	0.5
5b	$4.94 \cdot 10^{-2}$	3.6	2.1	+1.9	$^{+0.3}_{-0.5}$	$^{+0.5}_{-0.6}$	$^{-0.1}_{+0.1}$	$^{+0.0}_{-0.1}$	0.92	0.5
5c	$9.52 \cdot 10^{-2}$	2.9	1.1	+0.4	$^{+0.5}_{-0.5}$	$^{+0.6}_{-0.6}$	$^{+0.4}_{-0.3}$	$^{+0.1}_{-0.1}$	0.93	0.5
5d	$6.25 \cdot 10^{-2}$	2.9	1.9	+1.4	$^{+1.0}_{-0.9}$	$^{+0.3}_{-0.3}$	$^{-0.2}_{-0.0}$	$^{+0.1}_{-0.1}$	0.94	0.4
6d	$2.17 \cdot 10^{-1}$	6.7	2.3	+2.2	$^{+0.2}_{-0.3}$	$^{+0.3}_{-0.4}$	$^{-0.1}_{-0.2}$	$^{-0.0}_{+0.1}$	0.93	0.8

Table 20: Double-differential normalised inclusive dijet cross sections measured as a function of Q^2 and ξ_2 using the k_T jet algorithm. The total systematic uncertainty, δ^{sys}, sums all systematic uncertainties in quadrature, including the uncertainty due to the LAr noise of $\delta^{LArNoise} = 0.6$ %. Further details are given in the caption of table 10.

Normalised trijet cross sections in bins of Q^2 and $\langle P_T \rangle_3$ using the k_T jet algorithm

Bin label	σ/σ_{NC}	δ^{stat} [%]	δ^{sys} [%]	δ^{Model} [%]	δ^{JES} [%]	δ^{RCES} [%]	$\delta^{E'_e}$ [%]	δ^{θ_e} [%]	c^{had}	δ^{had} [%]
1α	$1.12 \cdot 10^{-2}$	8.9	3.8	+2.1	$^{-1.3}_{+1.6}$	$^{+2.8}_{-2.6}$	$^{-0.2}_{+0.3}$	$^{+0.3}_{-0.1}$	0.79	5.3
1β	$6.10 \cdot 10^{-3}$	8.6	3.1	+1.1	$^{+2.6}_{-2.9}$	$^{+0.3}_{-0.4}$	$^{+0.2}_{+0.1}$	$^{+0.0}_{-0.2}$	0.85	4.3
1γ	$1.00 \cdot 10^{-3}$	18.0	7.3	+5.8	$^{+4.1}_{-4.4}$	$^{-0.3}_{+0.6}$	$^{-0.9}_{+0.0}$	$^{+0.8}_{-0.6}$	0.89	3.6
2α	$1.03 \cdot 10^{-2}$	11.1	4.6	−2.9	$^{-1.9}_{+1.5}$	$^{+2.7}_{-3.3}$	$^{-0.2}_{+0.3}$	$^{+0.0}_{-0.1}$	0.78	5.0
2β	$6.50 \cdot 10^{-3}$	9.2	4.5	+3.5	$^{+2.5}_{-2.6}$	$^{+0.8}_{-0.8}$	$^{-0.3}_{+0.1}$	$^{+0.3}_{-0.3}$	0.84	4.4
2γ	$1.40 \cdot 10^{-3}$	17.5	4.9	−2.2	$^{+4.4}_{-4.1}$	$^{+0.2}_{-0.0}$	$^{+1.1}_{-0.3}$	$^{-0.2}_{+0.0}$	0.89	2.7
3α	$1.26 \cdot 10^{-2}$	10.5	4.7	−2.9	$^{-1.6}_{+1.6}$	$^{+3.2}_{-3.2}$	$^{-0.2}_{+0.5}$	$^{+0.1}_{-0.2}$	0.78	4.6
3β	$9.60 \cdot 10^{-3}$	8.0	5.5	+4.8	$^{+2.0}_{-2.3}$	$^{+0.9}_{-1.1}$	$^{-0.7}_{+0.5}$	$^{+0.4}_{-0.2}$	0.85	3.7
3γ	$1.80 \cdot 10^{-3}$	16.8	7.0	−4.5	$^{+5.4}_{-5.0}$	$^{+0.3}_{-0.2}$	$^{-1.0}_{+0.1}$	$^{+0.4}_{-1.0}$	0.87	2.3
4α	$1.40 \cdot 10^{-2}$	11.1	8.2	−7.5	$^{-1.5}_{+1.4}$	$^{+3.1}_{-2.8}$	$^{-0.4}_{+0.2}$	$^{+0.1}_{-0.2}$	0.77	4.1
4β	$1.29 \cdot 10^{-2}$	7.4	5.8	+5.3	$^{+1.8}_{-1.8}$	$^{+1.0}_{-1.1}$	$^{-0.8}_{+0.8}$	$^{+0.2}_{-0.1}$	0.85	3.6
4γ	$3.10 \cdot 10^{-3}$	13.8	6.2	+2.8	$^{+5.4}_{-5.4}$	$^{+0.6}_{-0.2}$	$^{-0.2}_{+0.4}$	$^{+0.3}_{-0.1}$	0.87	2.3
5α	$1.80 \cdot 10^{-2}$	9.8	7.5	−6.8	$^{-2.1}_{+2.1}$	$^{+1.9}_{-2.0}$	$^{+1.2}_{-1.0}$	$^{+0.2}_{-0.1}$	0.77	3.5
5β	$1.62 \cdot 10^{-2}$	7.4	4.0	+3.6	$^{+1.0}_{-1.1}$	$^{+0.9}_{-0.8}$	$^{-0.4}_{+0.6}$	$^{+0.0}_{-0.1}$	0.83	2.9
5γ	$3.70 \cdot 10^{-3}$	14.5	12.6	+11.7	$^{+4.3}_{-4.1}$	$^{+0.4}_{-0.6}$	$^{-1.1}_{+0.7}$	$^{+0.5}_{-0.4}$	0.86	2.2
6β	$1.41 \cdot 10^{-2}$	37.8	2.4	+1.9	$^{-0.5}_{+0.5}$	$^{+1.1}_{-0.9}$	$^{+0.9}_{+0.1}$	$^{+0.1}_{+0.5}$	0.82	0.8

Table 21: Double-differential normalised trijet cross sections measured as a function of Q^2 and $\langle P_T \rangle_3$ using the k_T jet algorithm. The total systematic uncertainty, δ^{sys}, sums all systematic uncertainties in quadrature, including the uncertainty due to the LAr noise of $\delta^{LArNoise} = 0.9\,\%$. Further details are given in the caption of table 11.

Normalised trijet cross sections in bins of Q^2 and ξ_3 using the k_T jet algorithm

Bin label	σ/σ_{NC}	δ^{stat} [%]	δ^{sys} [%]	δ^{Model} [%]	δ^{JES} [%]	δ^{RCES} [%]	$\delta^{E'_e}$ [%]	δ^{θ_e} [%]	c^{had}	δ^{had} [%]
1A	$7.30 \cdot 10^{-3}$	11.4	17.9	+17.4	$^{-0.6}_{+0.6}$	$^{+3.7}_{-3.8}$	$^{+0.5}_{-0.9}$	$^{+0.1}_{-0.2}$	0.81	6.5
1B	$7.20 \cdot 10^{-3}$	10.6	2.3	+1.5	$^{+0.8}_{-1.2}$	$^{+1.1}_{-0.9}$	$^{-0.2}_{+0.4}$	$^{+0.3}_{-0.4}$	0.81	5.3
1C	$2.90 \cdot 10^{-3}$	13.2	7.7	−6.4	$^{+4.2}_{-3.9}$	$^{+0.1}_{-0.2}$	$^{+0.5}_{-0.6}$	$^{+0.1}_{-0.2}$	0.81	3.7
2A	$5.90 \cdot 10^{-3}$	16.5	11.3	+10.7	$^{+0.0}_{+0.3}$	$^{+3.4}_{-3.4}$	$^{+0.7}_{-0.8}$	$^{+0.1}_{-0.2}$	0.80	5.7
2B	$8.80 \cdot 10^{-3}$	10.6	22.0	−21.9	$^{+0.7}_{-1.5}$	$^{+1.3}_{-1.4}$	$^{+0.5}_{-0.6}$	$^{+0.1}_{-0.1}$	0.81	4.9
2C	$3.10 \cdot 10^{-3}$	15.0	14.9	+14.5	$^{+3.5}_{-2.6}$	$^{+0.3}_{-0.1}$	$^{+0.7}_{-0.3}$	$^{+0.1}_{-0.1}$	0.80	3.5
3A	$6.80 \cdot 10^{-3}$	14.6	15.2	+14.7	$^{-0.5}_{+0.3}$	$^{+3.2}_{-3.3}$	$^{+1.0}_{-0.6}$	$^{+0.4}_{-0.3}$	0.80	5.1
3B	$1.16 \cdot 10^{-2}$	9.3	8.4	+8.1	$^{+0.1}_{-0.3}$	$^{+1.9}_{-1.8}$	$^{+0.0}_{-0.2}$	$^{+0.0}_{-0.1}$	0.81	4.5
3C	$5.40 \cdot 10^{-3}$	12.0	13.4	−13.0	$^{+3.4}_{-2.5}$	$^{+0.7}_{-0.6}$	$^{+0.8}_{-0.3}$	$^{+0.4}_{-0.1}$	0.80	3.0
4A	$7.10 \cdot 10^{-3}$	16.0	9.7	+9.2	$^{-1.4}_{+1.6}$	$^{+2.2}_{-2.6}$	$^{+0.8}_{-1.5}$	$^{-0.2}_{-0.1}$	0.80	5.1
4B	$1.36 \cdot 10^{-2}$	10.1	9.7	+9.4	$^{-0.0}_{+0.1}$	$^{+2.0}_{-1.9}$	$^{+0.3}_{-0.0}$	$^{+0.3}_{-0.2}$	0.81	4.5
4C	$9.10 \cdot 10^{-3}$	9.2	5.0	−4.1	$^{+2.7}_{-2.6}$	$^{+0.5}_{-0.4}$	$^{+0.1}_{-0.3}$	$^{+0.0}_{-0.2}$	0.81	3.1
5B	$1.59 \cdot 10^{-2}$	9.4	4.4	+4.1	$^{-0.4}_{+0.4}$	$^{+1.4}_{-1.3}$	$^{-0.0}_{+0.2}$	$^{-0.1}_{+0.2}$	0.80	2.9
5C	$1.81 \cdot 10^{-2}$	7.6	11.5	+11.3	$^{+0.9}_{-1.1}$	$^{+1.2}_{-1.2}$	$^{+0.1}_{-0.1}$	$^{+0.4}_{-0.3}$	0.80	2.8
6C	$4.23 \cdot 10^{-2}$	17.1	32.6	+32.5	$^{+0.6}_{-0.3}$	$^{+1.3}_{-1.2}$	$^{+1.0}_{-0.4}$	$^{+0.5}_{+0.0}$	0.79	1.1

Table 22: Double-differential normalised trijet cross sections measured as a function of Q^2 and ξ_3 using the k_T jet algorithm. The total systematic uncertainty, δ^{sys}, sums all systematic uncertainties in quadrature, including the uncertainty due to the LAr noise of $\delta^{LArNoise} = 0.9\,\%$. Further details are given in the caption of table 12.

Normalised inclusive jet cross sections in bins of Q^2 and $P_{\mathrm{T}}^{\mathrm{jet}}$ using the anti$-k_{\mathrm{T}}$ jet algorithm

Bin label	$\sigma/\sigma_{\mathrm{NC}}$	δ^{stat} [%]	δ^{sys} [%]	δ^{Model} [%]	δ^{JES} [%]	δ^{RCES} [%]	$\delta^{E'_{e}}$ [%]	$\delta^{\theta_{e}}$ [%]	c^{had}
1α	$1.61 \cdot 10^{-1}$	2.3	1.2	−0.6	$^{+0.7}_{-0.7}$	$^{+0.4}_{-0.4}$	$^{-0.5}_{+0.4}$	$^{+0.1}_{-0.2}$	0.93
1β	$7.17 \cdot 10^{-2}$	3.4	3.3	+2.3	$^{+2.1}_{-2.3}$	$^{-0.1}_{+0.2}$	$^{-0.5}_{+0.7}$	$^{+0.2}_{-0.3}$	0.94
1γ	$1.68 \cdot 10^{-2}$	6.3	4.9	+3.6	$^{+3.4}_{-3.0}$	$^{-0.3}_{+0.4}$	$^{-0.3}_{+0.8}$	$^{+0.4}_{-0.4}$	0.93
1δ	$2.00 \cdot 10^{-3}$	16.2	6.4	−4.4	$^{+4.5}_{-4.5}$	$^{-0.7}_{+0.5}$	$^{-0.3}_{-0.3}$	$^{+0.3}_{-0.5}$	0.93
2α	$1.75 \cdot 10^{-1}$	2.5	1.3	−0.8	$^{+0.5}_{-0.5}$	$^{+0.6}_{-0.5}$	$^{-0.6}_{+0.7}$	$^{+0.2}_{-0.1}$	0.93
2β	$8.24 \cdot 10^{-2}$	3.6	3.1	+2.1	$^{+2.1}_{-2.2}$	$^{-0.1}_{+0.2}$	$^{-0.6}_{+0.5}$	$^{+0.1}_{-0.2}$	0.95
2γ	$2.10 \cdot 10^{-2}$	6.4	5.6	+4.6	$^{+3.0}_{-2.9}$	$^{-0.5}_{+0.2}$	$^{-0.8}_{+0.4}$	$^{-0.0}_{-0.2}$	0.94
2δ	$2.80 \cdot 10^{-3}$	14.1	7.0	+5.0	$^{+4.8}_{-4.7}$	$^{-0.4}_{+0.7}$	$^{-0.2}_{+0.3}$	$^{+0.2}_{-0.3}$	0.93
3α	$1.93 \cdot 10^{-1}$	2.5	1.2	−0.1	$^{+0.4}_{-0.3}$	$^{+0.7}_{-0.7}$	$^{-0.8}_{+0.7}$	$^{+0.0}_{-0.1}$	0.94
3β	$9.90 \cdot 10^{-2}$	3.4	2.8	+1.8	$^{+1.9}_{-1.9}$	$^{+0.0}_{-0.0}$	$^{-0.8}_{+0.8}$	$^{+0.2}_{-0.2}$	0.95
3γ	$2.73 \cdot 10^{-2}$	5.7	3.8	+1.9	$^{+3.1}_{-3.2}$	$^{-0.2}_{+0.2}$	$^{-0.7}_{+0.7}$	$^{+0.3}_{-0.3}$	0.95
3δ	$3.30 \cdot 10^{-3}$	14.7	7.5	+5.3	$^{+4.9}_{-5.6}$	$^{-0.3}_{+0.4}$	$^{+0.3}_{-0.3}$	$^{+0.4}_{-0.2}$	0.93
4α	$2.11 \cdot 10^{-1}$	2.8	1.6	+0.7	$^{+0.6}_{-0.7}$	$^{+0.6}_{-0.6}$	$^{-1.0}_{+1.1}$	$^{+0.0}_{-0.0}$	0.94
4β	$1.23 \cdot 10^{-1}$	3.5	1.6	+0.3	$^{+1.3}_{-1.3}$	$^{+0.2}_{-0.0}$	$^{-0.7}_{+0.6}$	$^{+0.1}_{-0.1}$	0.95
4γ	$3.58 \cdot 10^{-2}$	5.5	4.2	+2.9	$^{+3.0}_{-2.8}$	$^{+0.1}_{-0.0}$	$^{-0.6}_{+0.7}$	$^{+0.2}_{-0.1}$	0.96
4δ	$3.80 \cdot 10^{-3}$	16.3	9.6	−8.2	$^{+5.3}_{-4.9}$	$^{-0.3}_{+0.4}$	$^{-0.0}_{-0.0}$	$^{+0.3}_{-0.2}$	0.93
5α	$2.36 \cdot 10^{-1}$	3.0	1.0	+0.4	$^{+0.5}_{-0.5}$	$^{+0.4}_{-0.3}$	$^{-0.3}_{+0.5}$	$^{-0.0}_{+0.0}$	0.92
5β	$1.58 \cdot 10^{-1}$	3.4	1.6	−0.6	$^{+1.2}_{-1.1}$	$^{+0.1}_{-0.1}$	$^{-0.7}_{+0.6}$	$^{-0.1}_{+0.1}$	0.97
5γ	$5.96 \cdot 10^{-2}$	4.3	2.5	+0.8	$^{+2.3}_{-2.2}$	$^{+0.1}_{-0.1}$	$^{-0.8}_{+0.8}$	$^{+0.1}_{-0.1}$	0.96
5δ	$1.02 \cdot 10^{-2}$	9.0	4.6	+1.9	$^{+4.1}_{-4.1}$	$^{-0.0}_{-0.1}$	$^{-0.6}_{+0.4}$	$^{+0.2}_{-0.3}$	0.95
6α	$2.96 \cdot 10^{-1}$	12.6	2.2	−2.0	$^{-0.3}_{-0.2}$	$^{+0.5}_{-0.3}$	$^{-0.8}_{-0.5}$	$^{-0.5}_{-0.2}$	0.90
6β	$2.13 \cdot 10^{-1}$	13.3	4.4	−3.9	$^{+1.1}_{-1.1}$	$^{+0.2}_{-0.4}$	$^{+1.8}_{+0.8}$	$^{+0.9}_{-0.0}$	0.95
6γ	$7.13 \cdot 10^{-2}$	20.7	8.5	−8.4	$^{+1.6}_{-1.3}$	$^{+0.3}_{-0.2}$	$^{+0.4}_{+0.5}$	$^{+0.2}_{+0.2}$	0.98
6δ	$3.18 \cdot 10^{-2}$	20.3	20.0	−19.9	$^{+2.1}_{-2.5}$	$^{+0.1}_{-0.2}$	$^{-0.2}_{+0.3}$	$^{+0.1}_{-0.1}$	0.98

Table 23: Double-differential normalised inclusive jet cross sections measured as a function of Q^2 and $P_{\mathrm{T}}^{\mathrm{jet}}$ using the anti$-k_{\mathrm{T}}$ jet algorithm. The uncertainties δ^{had} are identical to those in table 18 and are not repeated here. Further details are given in the caption of table 18.

Normalised dijet cross sections in bins of Q^2 and $\langle P_{\mathrm{T}}\rangle_2$ using the anti$-k_{\mathrm{T}}$ jet algorithm

Bin label	$\sigma/\sigma_{\mathrm{NC}}$	δ^{stat} [%]	δ^{sys} [%]	δ^{Model} [%]	δ^{JES} [%]	δ^{RCES} [%]	$\delta^{E'_{e}}$ [%]	$\delta^{\theta_{e}}$ [%]	c^{had}
1α	$5.45\cdot10^{-2}$	3.1	2.0	+1.8	$^{-0.1}_{-0.1}$	$^{+0.6}_{-0.4}$	$^{-0.5}_{+0.4}$	$^{+0.1}_{-0.2}$	0.95
1β	$3.31\cdot10^{-2}$	4.5	3.7	+3.2	$^{+1.7}_{-1.8}$	$^{-0.3}_{+0.3}$	$^{-0.3}_{+0.3}$	$^{+0.2}_{-0.1}$	0.95
1γ	$7.40\cdot10^{-3}$	6.7	5.2	+3.8	$^{+3.5}_{-3.3}$	$^{-0.4}_{+0.5}$	$^{-0.4}_{+0.2}$	$^{+0.3}_{-0.4}$	0.94
1δ	$9.00\cdot10^{-4}$	17.1	7.5	−5.9	$^{+5.2}_{-3.9}$	$^{-0.8}_{+0.7}$	$^{-0.4}_{-0.2}$	$^{+0.2}_{-0.5}$	0.94
2α	$6.23\cdot10^{-2}$	3.3	1.8	+1.5	$^{-0.2}_{+0.2}$	$^{+0.6}_{-0.5}$	$^{-0.5}_{+0.6}$	$^{+0.1}_{+0.0}$	0.95
2β	$3.60\cdot10^{-2}$	5.1	2.6	+1.9	$^{+1.5}_{-1.7}$	$^{-0.1}_{+0.2}$	$^{-0.8}_{+0.6}$	$^{+0.2}_{-0.3}$	0.96
2γ	$8.90\cdot10^{-3}$	7.1	6.1	+5.2	$^{+3.2}_{-3.1}$	$^{-0.6}_{+0.3}$	$^{-0.2}_{+0.3}$	$^{+0.2}_{-0.2}$	0.95
2δ	$1.30\cdot10^{-3}$	16.3	8.2	+5.8	$^{+6.2}_{-5.1}$	$^{-0.4}_{+0.8}$	$^{+0.5}_{+0.3}$	$^{+0.3}_{-0.1}$	0.94
3α	$6.94\cdot10^{-2}$	3.3	1.4	+0.9	$^{-0.2}_{+0.1}$	$^{+0.7}_{-0.7}$	$^{-0.6}_{+0.6}$	$^{+0.1}_{-0.1}$	0.94
3β	$4.29\cdot10^{-2}$	4.9	3.0	+2.4	$^{+1.6}_{-1.8}$	$^{+0.1}_{-0.1}$	$^{-0.6}_{+0.6}$	$^{+0.1}_{-0.1}$	0.96
3γ	$1.33\cdot10^{-2}$	5.6	3.2	+0.9	$^{+3.0}_{-3.0}$	$^{-0.2}_{+0.2}$	$^{-0.4}_{+0.3}$	$^{+0.2}_{-0.3}$	0.95
3δ	$1.00\cdot10^{-3}$	23.3	6.2	−3.6	$^{+5.1}_{-5.0}$	$^{-0.3}_{+0.4}$	$^{-0.2}_{-0.1}$	$^{+0.1}_{-0.3}$	0.95
4α	$7.69\cdot10^{-2}$	3.5	1.0	+0.4	$^{-0.4}_{+0.3}$	$^{+0.6}_{-0.5}$	$^{-0.3}_{+0.3}$	$^{+0.0}_{+0.0}$	0.93
4β	$5.11\cdot10^{-2}$	5.0	2.8	+2.3	$^{+1.2}_{-1.5}$	$^{+0.2}_{-0.2}$	$^{-0.5}_{+0.7}$	$^{+0.1}_{-0.1}$	0.96
4γ	$1.69\cdot10^{-2}$	5.5	3.8	+2.8	$^{+2.7}_{-2.3}$	$^{-0.1}_{+0.1}$	$^{-0.2}_{+0.4}$	$^{+0.1}_{-0.1}$	0.96
4δ	$1.80\cdot10^{-3}$	18.2	8.7	−6.8	$^{+5.4}_{-5.4}$	$^{-0.1}_{+0.3}$	$^{-0.1}_{+0.2}$	$^{+0.3}_{-0.3}$	0.94
5α	$8.54\cdot10^{-2}$	3.8	1.4	−0.8	$^{-0.8}_{+0.8}$	$^{+0.3}_{-0.3}$	$^{+0.4}_{-0.2}$	$^{+0.1}_{-0.0}$	0.92
5β	$7.38\cdot10^{-2}$	4.3	1.9	+1.4	$^{+1.0}_{-1.1}$	$^{+0.2}_{-0.2}$	$^{-0.4}_{+0.3}$	$^{-0.0}_{-0.1}$	0.95
5γ	$2.62\cdot10^{-2}$	5.0	3.4	+2.7	$^{+2.0}_{-1.8}$	$^{+0.2}_{-0.1}$	$^{-0.5}_{+0.5}$	$^{+0.2}_{-0.1}$	0.97
5δ	$4.90\cdot10^{-3}$	10.5	5.1	+2.9	$^{+4.3}_{-3.9}$	$^{+0.0}_{+0.0}$	$^{-0.2}_{+0.4}$	$^{+0.4}_{-0.3}$	0.96
6α	$9.70\cdot10^{-2}$	17.4	1.2	+0.4	$^{-0.1}_{+0.6}$	$^{+0.6}_{-0.4}$	$^{-0.5}_{+1.0}$	$^{-0.2}_{+0.5}$	0.91
6β	$8.19\cdot10^{-2}$	19.7	1.7	+1.5	$^{+0.5}_{-0.4}$	$^{+0.4}_{-0.2}$	$^{+0.2}_{+0.6}$	$^{+0.1}_{+0.3}$	0.94
6γ	$4.96\cdot10^{-2}$	14.8	5.3	−5.0	$^{+1.5}_{-1.9}$	$^{+0.2}_{-0.1}$	$^{-0.3}_{+0.2}$	$^{-0.3}_{+0.4}$	0.96
6δ	$1.45\cdot10^{-2}$	26.9	10.1	−9.8	$^{+2.3}_{-2.2}$	$^{+0.1}_{-0.3}$	$^{-0.2}_{+0.9}$	$^{+0.2}_{-0.0}$	0.97

Table 24: Double-differential normalised dijet cross sections measured as a function of Q^2 and $\langle P_{\mathrm{T}}\rangle_2$ using the anti$-k_{\mathrm{T}}$ jet algorithm. The uncertainties δ^{had} are identical to those in table 19 and are not repeated here. Further details are given in the caption of table 19.

Normalised dijet cross sections in bins of Q^2 and ξ_2 using the anti$-k_T$ jet algorithm

Bin label	σ/σ_{NC}	δ^{stat} [%]	δ^{sys} [%]	δ^{Model} [%]	δ^{JES} [%]	δ^{RCES} [%]	$\delta^{E'_e}$ [%]	δ^{θ_e} [%]	c^{had}
1a	$5.00 \cdot 10^{-2}$	3.0	8.5	+8.4	$^{+0.7}_{-0.7}$	$^{+1.1}_{-1.0}$	$^{+0.1}_{-0.1}$	$^{+0.2}_{-0.2}$	0.96
1b	$4.30 \cdot 10^{-2}$	3.1	3.0	+2.6	$^{+0.9}_{-1.1}$	$^{+0.7}_{-0.7}$	$^{+0.3}_{-0.4}$	$^{+0.2}_{-0.2}$	0.95
1c	$1.41 \cdot 10^{-2}$	6.5	9.2	−9.0	$^{+1.9}_{-1.7}$	$^{-0.2}_{+0.2}$	$^{+0.1}_{+0.3}$	$^{+0.3}_{-0.3}$	0.92
1d	$4.10 \cdot 10^{-3}$	8.9	6.7	+5.9	$^{+2.7}_{-3.1}$	$^{-0.4}_{+0.4}$	$^{-1.4}_{+0.9}$	$^{+0.1}_{-0.3}$	0.90
2a	$4.61 \cdot 10^{-2}$	5.2	9.1	+9.0	$^{+0.3}_{-0.2}$	$^{+0.9}_{-0.9}$	$^{-0.1}_{+0.2}$	$^{+0.1}_{-0.0}$	0.96
2b	$5.17 \cdot 10^{-2}$	3.3	2.5	+2.0	$^{+0.7}_{-0.9}$	$^{+0.7}_{-0.7}$	$^{+0.6}_{-0.6}$	$^{+0.1}_{-0.1}$	0.95
2c	$1.84 \cdot 10^{-2}$	6.0	2.6	+1.7	$^{+1.8}_{-1.8}$	$^{-0.0}_{+0.0}$	$^{+0.1}_{-0.0}$	$^{+0.2}_{-0.1}$	0.93
2d	$5.20 \cdot 10^{-3}$	8.8	5.2	+4.3	$^{+2.9}_{-2.3}$	$^{-0.3}_{+0.6}$	$^{-0.8}_{+1.3}$	$^{+0.3}_{-0.1}$	0.91
3a	$4.14 \cdot 10^{-2}$	4.0	8.0	+8.0	$^{+0.3}_{-0.3}$	$^{+0.9}_{-0.8}$	$^{-0.2}_{+0.2}$	$^{+0.2}_{-0.2}$	0.95
3b	$6.69 \cdot 10^{-2}$	2.8	2.9	+2.6	$^{+0.7}_{-0.7}$	$^{+0.7}_{-0.7}$	$^{+0.4}_{-0.5}$	$^{+0.0}_{-0.1}$	0.95
3c	$2.84 \cdot 10^{-2}$	4.6	2.9	−2.5	$^{+1.4}_{-1.5}$	$^{+0.1}_{-0.2}$	$^{+0.3}_{-0.3}$	$^{+0.2}_{-0.2}$	0.93
3d	$7.10 \cdot 10^{-3}$	7.8	5.7	−4.9	$^{+2.8}_{-2.8}$	$^{-0.3}_{+0.2}$	$^{-0.8}_{+0.4}$	$^{-0.1}_{-0.3}$	0.92
4a	$2.38 \cdot 10^{-2}$	7.5	3.3	+3.1	$^{+0.2}_{-0.2}$	$^{+0.7}_{-0.8}$	$^{+0.5}_{-0.3}$	$^{+0.1}_{-0.0}$	0.94
4b	$8.26 \cdot 10^{-2}$	3.0	2.4	+2.2	$^{+0.6}_{-0.6}$	$^{+0.7}_{-0.7}$	$^{+0.3}_{-0.3}$	$^{+0.1}_{-0.1}$	0.95
4c	$5.28 \cdot 10^{-2}$	3.4	6.0	+5.8	$^{+0.9}_{-0.9}$	$^{+0.4}_{-0.5}$	$^{+0.6}_{-0.9}$	$^{+0.1}_{-0.1}$	0.94
4d	$1.10 \cdot 10^{-2}$	7.4	13.9	+13.6	$^{+2.8}_{-2.8}$	$^{-0.0}_{+0.0}$	$^{-0.4}_{+0.4}$	$^{+0.2}_{-0.1}$	0.93
5b	$5.07 \cdot 10^{-2}$	3.3	1.7	+1.4	$^{+0.4}_{-0.4}$	$^{+0.5}_{-0.5}$	$^{-0.1}_{+0.1}$	$^{-0.0}_{-0.1}$	0.94
5c	$9.60 \cdot 10^{-2}$	2.7	6.8	+6.7	$^{+0.5}_{-0.6}$	$^{+0.5}_{-0.6}$	$^{+0.3}_{-0.3}$	$^{+0.2}_{-0.2}$	0.94
5d	$6.24 \cdot 10^{-2}$	2.8	8.5	+8.4	$^{+0.9}_{-1.0}$	$^{+0.3}_{-0.3}$	$^{-0.1}_{-0.1}$	$^{+0.1}_{-0.1}$	0.93
6d	$2.17 \cdot 10^{-1}$	6.7	4.9	+4.8	$^{+0.2}_{-0.5}$	$^{+0.4}_{-0.3}$	$^{+0.2}_{-0.4}$	$^{-0.1}_{-0.1}$	0.93

Table 25: Double-differential normalised inclusive dijet cross sections measured as a function of Q^2 and ξ_2 using the anti$-k_T$ jet algorithm. The uncertainties δ^{had} are identical to those in table 20 and are not repeated here. Further details are given in the caption of table 20.

Normalised trijet cross sections in bins of Q^2 and $\langle P_{\mathrm{T}} \rangle_3$ using the anti$-k_{\mathrm{T}}$ jet algorithm

Bin label	$\sigma/\sigma_{\mathrm{NC}}$	δ^{stat} [%]	δ^{sys} [%]	δ^{Model} [%]	δ^{JES} [%]	δ^{RCES} [%]	$\delta^{E'_e}$ [%]	δ^{θ_e} [%]	c^{had}
1α	$9.70 \cdot 10^{-3}$	8.9	5.8	+4.8	$^{-1.1}_{+1.0}$	$^{+2.7}_{-3.1}$	$^{-0.2}_{+0.3}$	$^{+0.1}_{-0.2}$	0.75
1β	$5.90 \cdot 10^{-3}$	8.1	4.8	+3.8	$^{+2.8}_{-2.8}$	$^{+0.6}_{-0.3}$	$^{+0.4}_{-0.1}$	$^{+0.1}_{-0.1}$	0.78
1γ	$7.00 \cdot 10^{-4}$	24.0	18.0	+17.5	$^{+4.4}_{-4.3}$	$^{-0.4}_{-0.2}$	$^{-1.2}_{+0.3}$	$^{+0.6}_{-0.8}$	0.81
2α	$9.80 \cdot 10^{-3}$	10.0	4.8	+3.3	$^{-1.0}_{+1.7}$	$^{+3.1}_{-2.9}$	$^{-0.2}_{+0.6}$	$^{+0.1}_{-0.1}$	0.74
2β	$5.60 \cdot 10^{-3}$	9.7	5.1	+4.2	$^{+2.0}_{-2.9}$	$^{+0.7}_{-0.9}$	$^{-0.5}_{-0.4}$	$^{+0.2}_{-0.4}$	0.78
2γ	$1.30 \cdot 10^{-3}$	17.6	8.0	+6.9	$^{+4.9}_{-3.0}$	$^{+0.2}_{+0.2}$	$^{+1.5}_{+0.0}$	$^{-0.2}_{+0.3}$	0.81
3α	$1.23 \cdot 10^{-2}$	9.2	4.0	+2.0	$^{-1.2}_{+1.5}$	$^{+2.9}_{-2.9}$	$^{-0.4}_{+1.1}$	$^{+0.3}_{-0.2}$	0.73
3β	$7.60 \cdot 10^{-3}$	8.6	7.8	+7.4	$^{+2.0}_{-2.4}$	$^{+1.0}_{-1.0}$	$^{-0.5}_{+0.2}$	$^{+0.3}_{-0.1}$	0.78
3γ	$1.90 \cdot 10^{-3}$	14.8	5.7	+1.6	$^{+5.4}_{-5.1}$	$^{+0.1}_{-0.4}$	$^{-1.4}_{+0.4}$	$^{+0.4}_{-0.9}$	0.80
4α	$1.17 \cdot 10^{-2}$	11.0	3.6	−1.9	$^{-1.5}_{+1.3}$	$^{+2.4}_{-2.6}$	$^{-0.3}_{-0.1}$	$^{-0.1}_{-0.0}$	0.73
4β	$1.13 \cdot 10^{-2}$	7.4	8.6	+8.2	$^{+2.2}_{-1.8}$	$^{+1.5}_{-1.3}$	$^{-0.6}_{+0.9}$	$^{+0.2}_{-0.2}$	0.78
4γ	$3.00 \cdot 10^{-3}$	14.0	10.5	+9.0	$^{+5.2}_{-5.3}$	$^{+0.4}_{-0.6}$	$^{-0.2}_{+0.6}$	$^{+0.1}_{+0.2}$	0.80
5α	$1.46 \cdot 10^{-2}$	10.2	3.4	−2.0	$^{-1.8}_{+1.8}$	$^{+1.7}_{-2.0}$	$^{+0.9}_{-0.6}$	$^{+0.2}_{-0.2}$	0.71
5β	$1.44 \cdot 10^{-2}$	7.4	6.7	+6.4	$^{+1.1}_{-1.1}$	$^{+1.1}_{-0.9}$	$^{-0.2}_{+0.4}$	$^{+0.2}_{-0.1}$	0.77
5γ	$3.10 \cdot 10^{-3}$	18.6	21.3	+20.8	$^{+4.1}_{-3.9}$	$^{+0.6}_{-0.8}$	$^{-1.3}_{+1.0}$	$^{+0.3}_{-0.3}$	0.79
6β	$1.52 \cdot 10^{-2}$	33.0	9.1	+9.0	$^{+0.6}_{-1.1}$	$^{+1.4}_{-0.5}$	$^{+0.3}_{+0.1}$	$^{-0.2}_{+0.2}$	0.74

Table 26: Double-differential normalised trijet cross sections measured as a function of Q^2 and $\langle P_{\mathrm{T}} \rangle_3$ using the anti$-k_{\mathrm{T}}$ jet algorithm. Further details are given in the caption of table 21. The uncertainties δ^{had} are identical to those in table 21 and are not repeated here. Further details are given in the caption of table 21.

Normalised trijet cross sections in bins of Q^2 and ξ_3 using the anti$-k_\mathrm{T}$ jet algorithm

Bin label	$\sigma/\sigma_\mathrm{NC}$	δ^stat [%]	δ^sys [%]	δ^Model [%]	δ^JES [%]	δ^RCES [%]	$\delta^{E'_e}$ [%]	δ^{θ_e} [%]	c^had
1A	$6.30 \cdot 10^{-3}$	11.5	17.5	+17.1	$^{-0.5}_{+0.6}$	$^{+3.7}_{-3.5}$	$^{+0.5}_{-0.8}$	$^{+0.1}_{-0.2}$	0.76
1B	$7.00 \cdot 10^{-3}$	9.0	13.2	+13.1	$^{+0.8}_{-0.9}$	$^{+1.2}_{-1.2}$	$^{-0.2}_{+0.4}$	$^{+0.2}_{-0.2}$	0.76
1C	$2.30 \cdot 10^{-3}$	13.5	16.4	−15.9	$^{+3.8}_{-4.1}$	$^{+0.1}_{-0.4}$	$^{+0.5}_{-0.5}$	$^{+0.4}_{-0.1}$	0.74
2A	$5.30 \cdot 10^{-3}$	16.6	16.7	+16.3	$^{+0.1}_{+0.2}$	$^{+3.7}_{-3.2}$	$^{+1.1}_{-1.0}$	$^{+0.1}_{-0.0}$	0.75
2B	$8.10 \cdot 10^{-3}$	9.7	11.3	+11.2	$^{+0.4}_{-0.6}$	$^{+1.3}_{-1.3}$	$^{+0.1}_{-0.2}$	$^{+0.1}_{-0.2}$	0.76
2C	$2.60 \cdot 10^{-3}$	14.7	47.6	−47.4	$^{+4.0}_{-3.7}$	$^{+0.4}_{-0.4}$	$^{+1.0}_{-1.3}$	$^{-0.0}_{-0.2}$	0.74
3A	$5.30 \cdot 10^{-3}$	16.1	18.4	+18.1	$^{-0.7}_{+0.6}$	$^{+3.5}_{-3.0}$	$^{+1.4}_{-0.7}$	$^{+0.4}_{-0.3}$	0.75
3B	$1.12 \cdot 10^{-2}$	8.4	17.2	+17.0	$^{+0.7}_{-0.2}$	$^{+1.9}_{-2.0}$	$^{+0.2}_{-0.1}$	$^{+0.2}_{-0.0}$	0.76
3C	$4.20 \cdot 10^{-3}$	11.7	11.3	−10.8	$^{+2.9}_{-3.6}$	$^{+0.4}_{-0.3}$	$^{+0.2}_{-0.4}$	$^{+0.3}_{-0.4}$	0.74
4A	$5.80 \cdot 10^{-3}$	15.9	16.3	+16.1	$^{-0.9}_{+0.2}$	$^{+2.2}_{-2.3}$	$^{+1.0}_{-1.8}$	$^{-0.1}_{-0.1}$	0.73
4B	$1.22 \cdot 10^{-2}$	9.4	20.0	−19.9	$^{+0.0}_{+0.4}$	$^{+2.0}_{-1.9}$	$^{+0.5}_{-0.5}$	$^{+0.3}_{-0.1}$	0.76
4C	$7.60 \cdot 10^{-3}$	9.1	17.3	−17.0	$^{+2.7}_{-3.0}$	$^{+0.6}_{-0.7}$	$^{+0.4}_{-0.4}$	$^{+0.1}_{-0.2}$	0.75
5B	$1.40 \cdot 10^{-2}$	9.1	7.7	+7.5	$^{-0.3}_{+0.6}$	$^{+1.3}_{-1.4}$	$^{+0.3}_{-0.1}$	$^{+0.0}_{+0.1}$	0.75
5C	$1.60 \cdot 10^{-2}$	7.0	52.8	−52.8	$^{+1.0}_{-1.0}$	$^{+1.2}_{-1.2}$	$^{+0.2}_{-0.1}$	$^{+0.3}_{-0.3}$	0.75
6C	$3.52 \cdot 10^{-2}$	17.5	94.7	−94.6	$^{+0.3}_{-0.1}$	$^{+1.3}_{-1.0}$	$^{+0.6}_{-0.4}$	$^{+0.3}_{-0.2}$	0.73

Table 27: Double-differential normalised trijet cross sections measured as a function of Q^2 and ξ_3 using the anti$-k_\mathrm{T}$ jet algorithm. The uncertainties δ^had are identical to those in table 22 and are not repeated here. Further details are given in the caption of table 22.

Inclusive jet as function of Q^2 and P_T^{jet}

	1α	1β	1γ	1δ	2α	2β	2γ	2δ	3α	3β	3γ	3δ	4α	4β	4γ	4δ	5α	5β	5γ	5δ	6α	6β	6γ	6δ
1α	100	-20	-11	-2	-14	2	1		1															
1β		100	2	-1	4	-13				2														
1γ			100	6	1		-13	-1			2								1					
1δ				100				-14				2								1				1
2α					100	-21	-10	-2	-11	2	1		-1				-1							
2β						100	2	-1	3	-10								-1						
2γ							100	7	1	1	-12								-1					
2δ								100				-11								-1				
3α									100	-23	-12	-2	-8	1	1		-1							
3β										100		-2	2	-8										
3γ											100	5	1	1	-8				-1					
3δ												100				-8								
4α													100	-22	-11	-2	-4	1						
4β														100	-1	-2	1	-4						
4γ															100	5		1	-4					
4δ																100				-5				
5α																	100	-24	-12	-2	-1			
5β																		100	1	-2		-1		
5γ																			100	3			-1	
5δ																				100				-2
6α																					100	-21	-15	-3
6β																						100	-1	
6γ																							100	-2
6δ																								100

(Row axis label: **Inclusive jet as function of Q^2 and P_T^{jet}**)

Table 28: Correlation coefficients between data points of the inclusive jet measurement as a function of Q^2 and P_T^{jet}. Since the matrix is symmetric only the upper triangle is given. The bin labels are defined in table 7. All values are multiplied by a factor of 100.

	1α	1β	1γ	1δ	2α	2β	2γ	2δ	3α	3β	3γ	3δ	4α	4β	4γ	4δ	5α	5β	5γ	5δ	6α	6β	6γ	6δ
Dijet as function of $Q^2$and $\langle P_{\mathrm{T}}\rangle_2$	**Dijet as function of $Q^2$and $\langle P_{\mathrm{T}}\rangle_2$**																							
1α	100	-44	11	3	-3	6	-2		11	-1			9				8				2			
1β		100	-36	-9	7	-13	5	1	-1	2	-1			1				1						
1γ			100	6	-1	4	-14			-1	2				1				1				1	
1δ				100		1		-14				2								1				1
2α					100	-44	10	2	-4	6	-1		4	1			4	1			1			
2β						100	-34	-8	7	-11	4	1	1	-1			2	-1						
2γ							100	2	-1	4	-12								-1				-1	
2δ								100		1	1	-11							1	-2		1	1	
3α									100	-47	11	3	-3	5	-1		4	1			1			
3β										100	-34	-10	5	-8	3	1	1							
3γ											100	2	-1	3	-8				-1	1			-1	
3δ												100		1		-9				-1				
4α													100	-45	11	3	-1	3			1			
4β														100	-36	-11	3	-4	2	1				
4γ															100	4		2	-5					
4δ																100			1	-6			1	1
5α																	100	-46	10	2	1	1		
5β																		100	-35	-8	1	-1		
5γ																			100	-3		1	-1	-1
5δ																				100			1	2
6α																					100	-41	7	2
6β																						100	-36	-9
6γ																							100	-13
6δ																								100

Table 29: Correlation coefficients between data points of the dijet measurement as a function of Q^2 and $\langle P_{\mathrm{T}}\rangle_2$. Since the matrix is symmetric only the upper triangle is given. The bin labels are defined in table 7. All values are multiplied by a factor of 100.

Trijet as function of Q^2 and $\langle P_T \rangle_3$ (columns); **Trijet as function of Q^2 and $\langle P_T \rangle_3$** (rows)

	1α	1β	1γ	2α	2β	2γ	3α	3β	3γ	4α	4β	4γ	5α	5β	5γ	6β
1α	100	-37	9	1	2		14	-4	1	12	-3	1	12	-3	1	-1
1β		100	-26	1	-8	2	-3	7	-2	-3	5	-1	-3	6	-1	2
1γ			100		2	-11	1	-2	5	1	-1	3		-1	3	
2α				100	-35	8	2	1		11	-3	1	10	-2		-1
2β					100	-24	1	-5	2	-3	6	-1	-2	6	-1	2
2γ						100		2	-8		-1	3		-1	3	
3α							100	-37	10	3	1		10	-3	1	-1
3β								100	-29		-2	1	-2	7	-1	2
3γ									100		1	-5		-1	3	
4α										100	-35	9	5	-1		-1
4β											100	-27	-1	3		2
4γ												100			1	
5α													100	-35	9	
5β														100	-28	2
5γ															100	
6β																100

Table 30: Correlation coefficients between data points of the trijet measurement as a function of Q^2 and $\langle P_T \rangle_3$. Since the matrix is symmetric only the upper triangle is given. The bin labels are defined in table 7. All values are multiplied by a factor of 100.

Dijet as function of Q^2 and $\langle P_T \rangle_2$ (columns); **Inclusive jet as function of Q^2 and P_T^{jet}** (rows)

	1α	1β	1γ	1δ	2α	2β	2γ	2δ	3α	3β	3γ	3δ	4α	4β	4γ	4δ	5α	5β	5γ	5δ	6α	6β	6γ	6δ
1α	35	1	-2		-5				1															
1β	-6	25	-1	-1	1	-3				1														
1γ	-1	-3	48	1			-6				1													
1δ		1	-6	71				-10				1												
2α	-5				34		-1		-4				-1				-1							
2β	1	-4			-7	27	-1		1	-3								-1						
2γ			-7		-1	-3	49	-2		1	-6								-1					
2δ			1	-11		-1	-1	69			1	-7								-1				
3α	1				-5	1			35	1	-1		-3											
3β		1			1	-3			-6	25		-2		-2				-1						
3γ			1			1	-7		-1	-5	51	-1			-5				-1				-1	
3δ				2				-8		-1	-3	66				-6				-1				
4α					-1	1			-3	1			35		-1		-2							
4β									1	-2			-6	25	-1	-1		-2						
4γ											-4		-1	-2	48	-3			-3					
4δ								-1				-6	1	-1	-1	70			1	-4				1
5α	1				-1								-2				32	1	-1					
5β						-1					1			-2	1		-7	24	-1					
5γ			1				-1				-1				-3	1	-1	-4	50	-2			-1	
5δ				1				-1			1	-1				-4			-8	73				-2
6α																					30	2	-2	-1
6β																					-8	21		-2
6γ																			-1		-3	-3	44	-7
6δ																				-1		-2	-2	66

Table 31: Correlation coefficients between data points of the inclusive jet measurement as a function of Q^2 and P_T^{jet} and of the dijet measurement as a function of Q^2 and $\langle P_T \rangle_2$. The bin labels are defined in table 7. All values are multiplied by a factor of 100.

Inclusive jet as function of Q^2 and $P_{\mathrm{T}}^{\mathrm{jet}}$ / Trijet as function of Q^2 and $\langle P_{\mathrm{T}}\rangle_3$	1α	1β	1γ	2α	2β	2γ	3α	3β	3γ	4α	4β	4γ	5α	5β	5γ	6β
1α	11	2	1	-2						-1			-1			
1β	10	12	1	-3	-2		-1			-1			-2			
1γ	-6	18	12	1	-4	-2		-1			-1			-2		
1δ	2	-4	18		2	-6		1	-2		1	-2			-2	
2α	-2			10	1	1	-2						-1			
2β	-3	-2		10	13	-1	-1	-1					-1			
2γ	1	-3	-2	-6	16	16	1	-3	-2		-1			-1		
2δ		1	-5	2	-7	22		1	-2			-1			-3	
3α				-2			12	1	2	-1						
3β	-2			-2	-2		7	12		-1	-1		-1			
3γ		-1		1	-3	-2	-7	15	12	1	-3	-1		-1		
3δ			-1		1	-3	2	-7	23		1	-3			-2	
4α	-1						-1			8	3	2	-1			
4β	-1			-1			-1	-1		8	11	1	-1	-1		
4γ		-1			-1		1	-2	-1	-6	16	15		-2	-1	
4δ			-1					1	-3	2	-7	23			-4	
5α	-1									-1			9	3		
5β	-1			-1			-1			-1	-1		8	10	2	
5γ		-1	-1		-1			-1		1	-2	-1	-5	14	13	-1
5δ			-1			-1			-1		1	-3	2	-6	13	
6α																3
6β	-1															7
6γ																14
6δ															-1	-8

Table 32: Correlation coefficients between data points of the inclusive jet measurement as a function of Q^2 and $P_{\mathrm{T}}^{\mathrm{jet}}$ and of the trijet measurement as a function of Q^2 and $\langle P_{\mathrm{T}}\rangle_3$. The bin labels are defined in table 7. All values are multiplied by a factor of 100.

	Trijet as function of Q^2 and $\langle P_T \rangle_3$															
Dijet as function of Q^2 and $\langle P_T \rangle_2$	1α	1β	1γ	2α	2β	2γ	3α	3β	3γ	4α	4β	4γ	5α	5β	5γ	6β
1α	13	-7	2	-2	1											
1β	5	16	-5	-2	-3	1	-1			-1			-1			
1γ	-4	12	21	1	-3	-3	1	-1		1	-1		1	-2		
1δ	2	-5	15		1	-4			-2			-2			-2	
2α	-2	1		13	-7	2	-1	1								
2β	-2	-2	1	5	17	-5	-1	-2	1							
2γ	1	-3	-3	-3	8	22	1	-2	-3		-1			-1		
2δ		1	-3	1	-4	13		1	-2			-1			-3	
3α				-1			14	-7	3	-1	1					
3β	-1			-1	-2	1	3	17	-7	-1	-1	1				
3γ	1	-1		1	-2	-3	-4	12	23	1	-2	-2		-1		
3δ					1	-2	3	-8	20		1	-2			-1	
4α							-1			12	-6	3				
4β	-1						-1	-1	1	4	17	-7		-1		
4γ		-1	-1		-1		1	-2	-2	-4	9	29	1	-1	-1	
4δ			-1					1	-2	2	-7	18			-4	
5α													13	-6	2	
5β	-1										-1		4	16	-5	
5γ	1	-1	-1	1	-1		1	-1		1	-2	-1	-4	11	18	
5δ			-1								1	-2	2	-5	11	
6α																-10
6β																22
6γ		-1						-1						-1	-1	4
6δ															-1	-5

Table 33: Correlation coefficients between data points of the dijet measurement as a function of Q^2 and $\langle P_T \rangle_2$ and of the trijet measurement as a function of Q^2 and $\langle P_T \rangle_3$. The bin labels are defined in table 7. All values are multiplied by a factor of 100.

	Dijet as function of Q^2 and ξ_2																			
	1a	1b	1c	1d	2a	2b	2c	2d	3a	3b	3c	3d	4a	4b	4c	4d	5b	5c	5d	6d
1a	100	-35	2	-23	-14	1		3	3				3				-1			
1b		100	-39	14	5	-10	4	-1		4	-1		1	3		1	3	-1	2	
1c			100	-25		5	-10	3		-1	3	-1		1	2	-1		2	-1	
1d				100	3	-1	3	-14			-1	2				1			1	
2a					100	-22	13	-22	2		-1	1	1		-1		-1			-1
2b						100	-38	8	5	-7	3	-1	1	3	-1		4	-1	1	
2c							100	-26	-2	4	-7	3			1	-1		2	-1	
2d								100	-3	-1	3	-10				1			1	1
3a									100	-33	15	-7	-6	2	-2		-2			
3b										100	-34	9	2	-3	1		6	-1	1	1
3c											100	-27	-1	3	-3	1		4	-1	-1
3d												100		-1	2	-5			1	
4a													100	-13	12	-17	3	-2	1	
4b														100	-29	-9	4		-1	
4c															100	-20	3	6	-2	-1
4d																100	-2	1		
5b																	100	-16	21	
5c																		100	-24	-3
5d																			100	14
6d																				100

(Row label: Dijet as function of Q^2 and ξ_2)

Table 34: Correlation coefficients between data points of the dijet measurement as a function of Q^2 and ξ_2. Since the matrix is symmetric only the upper triangle is given. The bin labels are defined in table 7. All values are multiplied by a factor of 100.

	Trijet as function of Q^2 and ξ_3														
	1A	1B	1C	2A	2B	2C	3A	3B	3C	4A	4B	4C	5B	5C	6C
1A	100	-35	12	-5	2	-1	11	-3		6	-2	1	-3	2	1
1B		100	-43	3	-8	1	-2	6	-1	-1	6	-1	8	-5	-2
1C			100		4	-8	1	-1	2		-1	3	-2	6	3
2A				100	-33	9	-4	1	1	5	-2	1	-2	1	
2B					100	-43	3	-7	3	-1	6	-1	6	-3	-2
2C						100	-2	5	-6		-1	3	-2	6	3
3A							100	-37	8	-4	1	-1	-2		
3B								100	-36	2			8	-2	-2
3C									100	-1	2	-2		5	3
4A										100	-39	11			1
4B											100	-36	6	-3	-2
4C												100	-1	5	4
5B													100	-33	-4
5C														100	10
6C															100

(Row label: Trijet as function of Q^2 and ξ_3)

Table 35: Correlation coefficients between data points of the trijet measurement as a function of Q^2 and ξ_2. Since the matrix is symmetric only the upper triangle is given. The bin labels are defined in table 7. All values are multiplied by a factor of 100.

Inclusive jet as function of Q^2 and P_T^{jet}	Dijet as function of Q^2 and ξ_2																			
	1a	1b	1c	1d	2a	2b	2c	2d	3a	3b	3c	3d	4a	4b	4c	4d	5b	5c	5d	6d
1α	28	7	6		-3	-2	-1		1				1							
1β	4	21	9	3		-2	-1	-1	1	1										
1γ		4	13	24		-1	-2	-3			1	1								
1δ	6		-3	28	-1			-4				1								
2α	-3	-1	-1		26	10	7		-3	-1	-1									
2β		-3	-1		2	19	12	2	-2	-2	-2									
2γ	-1		-2	-3	2	4	12	26	1	-1	-2	-4								
2δ	-2			-4	5	1	-2	31	1			-3								
3α	1	1			-2	-1	-1		31	14	9		-1	-1	-1					
3β		1			-1	-2	-2		6	22	12	1		-2	-1					
3γ			1	1			-2	-3	-1	3	15	30			-1	-3				
3δ			-1	1	-1			-3		2	-4	31				-1				
4α						1			-2	-1	-1		21	20	11	-1	-1	-1	-1	
4β										-1	-1		-2	16	14	6	-1	-1	-1	
4γ											-1	-2	1	2	16	27			-1	
4δ												-2	2	2	-2	24				
5α										1			-1	-1			27	19	15	
5β			1											-1	-1		11	20	21	
5γ								-1								-1		10	24	-1
5δ															1	-1	2	-2	18	
6α																		-1	4	34
6β																				27
6γ																				16
6δ																			-1	8

Table 36: Correlation coefficients between data points of the inclusive jet measurement as a function of Q^2 and P_T^{jet} and of the dijet measurement as a function of Q^2 and ξ_2. The bin labels are defined in table 7. All values are multiplied by a factor of 100.

Inclusive jet as function of Q^2 and P_T^{jet}	Trijet as function of Q^2 and ξ_3														
	1A	1B	1C	2A	2B	2C	3A	3B	3C	4A	4B	4C	5B	5C	6C
1α	17	6	1	-3	-1		-1	1							
1β	8	15	8	-2	-3	-1		-1			-1		-1		
1γ		7	21		-2	-3					-1	-1	-1	-1	
1δ	1	-1	11			-2								-1	-1
2α	-3	-1		14	6	2	-2	-1							
2β	-2	-3	-1	8	14	5	-1	-2			-1		-1		
2γ		-1	-4	-1	8	20		-1	-2					-1	-1
2δ			-2	1	1	13			-1						
3α				-1	-1		17	8	3	-1	-1				
3β	-1			-1	-2	-1	5	16	5	-1	-2	-1		-1	
3γ					-1	-3	-1	6	16			-2		-1	-1
3δ						-1			11			-1			
4α							-1	-1		14	9	4	-1		
4β		-1						-2		4	15	7	-1	-1	
4γ									-2	-2	6	25		-2	
4δ									-1	2	1	8		-1	
5α											-1		11	9	-1
5β			-1			-1			-1		-1	-1	13	12	-1
5γ			-1						-1			-1	3	19	-1
5δ												-1	-1	7	
6α														-1	24
6β			-1			-1			-1			-1		-2	18
6γ															21
6δ														-1	11

Table 37: Correlation coefficients between data points of the inclusive jet measurement as a function of Q^2 and P_T^{jet} and the data points of the trijet measurement as a function of Q^2 and ξ_3. The bin labels are defined in table 7. All values are multiplied by a factor of 100.

Dijet as function of Q^2 and ξ_2	Trijet as function of Q^2 and ξ_3														
	1A	1B	1C	2A	2B	2C	3A	3B	3C	4A	4B	4C	5B	5C	6C
1a	16	-2		-3		-1	-2			-1					
1b		16	-2		-3	1									
1c	-1	5	9	1	-2	-2	1	-1		1	-2		-2		
1d	4	-5	17	-1	1	-3			-1			-1	1	-2	-1
2a	-4			12	-2	1	-2								
2b		-3	1	1	15	-4		-2					-1	1	
2c	1	-2	-2		4	11	1	-2	-1		-1		-1		
2d	-1	1	-3	3	-2	15	-1	1	-2					-1	-1
3a	-2			-2	1		23	-7	3	-3					
3b					-2	1	2	19	-4		-2				
3c		-1			-1	-2	-1	5	11		-1	-1	-1		
3d						-2	3	-2	13		1	-2		-1	-1
4a	-2						-2	1		17	-7	2		-1	
4b		-1					-1	-2		5	15	-3	-1		
4c	1	-1			-1			-2	-1	-3	9	12	-2		
4d		1	-1				-1	1	-1	4	-3	16	1	-2	-1
5b	-1	-1						-1			-1		9	1	-1
5c	1	-1		1	-1	-1		-1			-2	-1	15	6	-1
5d	-1	1	-1			-1		1	-1			-2	3	16	-2
6d			-1			-1			-1			-1	1	-3	29

Table 38: Correlation coefficients between data points of the dijet measurement as a function of Q^2 and ξ_2 and of the trijet measurement as a function of Q^2 and ξ_3. The bin labels are defined in table 7. All values are multiplied by a factor of 100.

$\alpha_s(M_Z)$ using different PDF sets

Measurement	$\alpha_s^{\text{MSTW2008}}$	α_s^{CT10}	$\alpha_s^{\text{NNPDF2.3}}$	$\alpha_s^{\text{HERAPDF1.5}}$	α_s^{ABM11}
	All PDF sets used were determined with $\alpha_s(M_Z) = 0.1180$				
σ_{jet}	0.1174	0.1180	0.1167	0.1158	0.1136
σ_{dijet}	0.1137	0.1142	0.1127	0.1120	0.1101
σ_{trijet}	0.1178	0.1178	0.1169	0.1174	0.1176
$\frac{\sigma_{\text{jet}}}{\sigma_{\text{NC}}}$	0.1176	0.1185	0.1170	0.1183	0.1186
$\frac{\sigma_{\text{dijet}}}{\sigma_{\text{NC}}}$	0.1135	0.1143	0.1127	0.1143	0.1150
$\frac{\sigma_{\text{trijet}}}{\sigma_{\text{NC}}}$	0.1182	0.1185	0.1175	0.1191	0.1204
$[\sigma_{\text{jet}}, \sigma_{\text{dijet}}, \sigma_{\text{trijet}}]$	0.1185	0.1187	0.1178	0.1180	0.1176
$\left[\frac{\sigma_{\text{jet}}}{\sigma_{\text{NC}}}, \frac{\sigma_{\text{dijet}}}{\sigma_{\text{NC}}}, \frac{\sigma_{\text{trijet}}}{\sigma_{\text{NC}}}\right]$	0.1165	0.1172	0.1158	0.1172	0.1177

Table 39: Values for $\alpha_s(M_Z)$ obtained from fits to absolute and normalized cross sections using different PDF sets.

Summary of values of $\alpha_s(M_Z)$ and uncertainties

Measurement	$\alpha_s(M_Z)\vert_{k_T}$	$\alpha_s(M_Z)\vert_{\text{anti}-k_T}$	PDF and theoretical uncertainties						
			Individual contributions						Total
σ_{jet}	0.1174 $(22)_{\text{exp}}$	0.1175 $(22)_{\text{exp}}$	$(7)_{\text{PDF}}$	$(7)_{\text{PDFset}}$	$(5)_{\text{PDF}(\alpha_s)}$	$(10)_{\text{had}}$	$(48)_{\mu_r}$	$(6)_{\mu_f}$	$(50)_{\text{pdf,theo}}$
σ_{dijet}	0.1137 $(23)_{\text{exp}}$	0.1152 $(23)_{\text{exp}}$	$(7)_{\text{PDF}}$	$(7)_{\text{PDFset}}$	$(5)_{\text{PDF}(\alpha_s)}$	$(7)_{\text{had}}$	$(37)_{\mu_r}$	$(6)_{\mu_f}$	$(40)_{\text{pdf,theo}}$
σ_{trijet}	0.1178 $(17)_{\text{exp}}$	0.1174 $(18)_{\text{exp}}$	$(3)_{\text{PDF}}$	$(5)_{\text{PDFset}}$	$(0)_{\text{PDF}(\alpha_s)}$	$(11)_{\text{had}}$	$(34)_{\mu_r}$	$(3)_{\mu_f}$	$(36)_{\text{pdf,theo}}$
$\frac{\sigma_{\text{jet}}}{\sigma_{\text{NC}}}$	0.1176 $(9)_{\text{exp}}$	0.1172 $(8)_{\text{exp}}$	$(6)_{\text{PDF}}$	$(7)_{\text{PDFset}}$	$(4)_{\text{PDF}(\alpha_s)}$	$(8)_{\text{had}}$	$(41)_{\mu_r}$	$(6)_{\mu_f}$	$(44)_{\text{pdf,theo}}$
$\frac{\sigma_{\text{dijet}}}{\sigma_{\text{NC}}}$	0.1135 $(10)_{\text{exp}}$	0.1147 $(9)_{\text{exp}}$	$(5)_{\text{PDF}}$	$(8)_{\text{PDFset}}$	$(3)_{\text{PDF}(\alpha_s)}$	$(6)_{\text{had}}$	$(32)_{\mu_r}$	$(6)_{\mu_f}$	$(35)_{\text{pdf,theo}}$
$\frac{\sigma_{\text{trijet}}}{\sigma_{\text{NC}}}$	0.1182 $(11)_{\text{exp}}$	0.1177 $(12)_{\text{exp}}$	$(3)_{\text{PDF}}$	$(5)_{\text{PDFset}}$	$(0)_{\text{PDF}(\alpha_s)}$	$(11)_{\text{had}}$	$(34)_{\mu_r}$	$(3)_{\mu_f}$	$(36)_{\text{pdf,theo}}$
$[\sigma_{\text{jet}}, \sigma_{\text{dijet}}, \sigma_{\text{trijet}}]$	0.1185 $(16)_{\text{exp}}$	0.1181 $(17)_{\text{exp}}$	$(3)_{\text{PDF}}$	$(4)_{\text{PDFset}}$	$(2)_{\text{PDF}(\alpha_s)}$	$(13)_{\text{had}}$	$(38)_{\mu_r}$	$(3)_{\mu_f}$	$(40)_{\text{pdf,theo}}$
$\left[\frac{\sigma_{\text{jet}}}{\sigma_{\text{NC}}}, \frac{\sigma_{\text{dijet}}}{\sigma_{\text{NC}}}, \frac{\sigma_{\text{trijet}}}{\sigma_{\text{NC}}}\right]$	0.1165 $(8)_{\text{exp}}$	0.1165 $(7)_{\text{exp}}$	$(5)_{\text{PDF}}$	$(7)_{\text{PDFset}}$	$(3)_{\text{PDF}(\alpha_s)}$	$(8)_{\text{had}}$	$(36)_{\mu_r}$	$(5)_{\mu_f}$	$(38)_{\text{pdf,theo}}$

Table 40: Values of $\alpha_s(M_Z)$ obtained from fits to absolute and normalised single jet and multijet cross sections employing the k_T or the anti$-k_T$ jet algorithm. Theoretical uncertainties are quoted for the fits to the k_T jet cross sections.

$\alpha_s(M_Z)$ from data points with comparable μ_r-values

$\langle\mu_r\rangle$ [GeV]	No. of data points	$\alpha_s(M_Z)\vert_{k_T}$	$\alpha_s(M_Z)\vert_{\text{anti}-k_T}$	PDF and theoretical uncertainties Individual contributions	Total
11.9	9	$0.1168\,(10)_{\text{exp}}$	$0.1174\,(10)_{\text{exp}}$	$(6)_{\text{PDF}}$ $(10)_{\text{PDFset}}$ $(5)_{\text{PDF}(\alpha_s)}$ $(10)_{\text{had}}$ $(43)_{\mu_r}$ $(6)_{\mu_f}$	$(47)_{\text{pdf,theo}}$
14.1	6	$0.1155\,(16)_{\text{exp}}$	$0.1159\,(14)_{\text{exp}}$	$(6)_{\text{PDF}}$ $(11)_{\text{PDFset}}$ $(3)_{\text{PDF}(\alpha_s)}$ $(9)_{\text{had}}$ $(37)_{\mu_r}$ $(5)_{\mu_f}$	$(40)_{\text{pdf,theo}}$
17.4	18	$0.1174\,(13)_{\text{exp}}$	$0.1163\,(13)_{\text{exp}}$	$(5)_{\text{PDF}}$ $(12)_{\text{PDFset}}$ $(1)_{\text{PDF}(\alpha_s)}$ $(7)_{\text{had}}$ $(34)_{\mu_r}$ $(5)_{\mu_f}$	$(37)_{\text{pdf,theo}}$
25.6	22	$0.1153\,(14)_{\text{exp}}$	$0.1150\,(14)_{\text{exp}}$	$(4)_{\text{PDF}}$ $(11)_{\text{PDFset}}$ $(2)_{\text{PDF}(\alpha_s)}$ $(5)_{\text{had}}$ $(28)_{\mu_r}$ $(5)_{\mu_f}$	$(31)_{\text{pdf,theo}}$
59.6	9	$0.1169\,(66)_{\text{exp}}$	$0.1185\,(60)_{\text{exp}}$	$(10)_{\text{PDF}}$ $(1)_{\text{PDFset}}$ $(1)_{\text{PDF}(\alpha_s)}$ $(4)_{\text{had}}$ $(29)_{\mu_r}$ $(8)_{\mu_f}$	$(32)_{\text{pdf,theo}}$

$\alpha_s(\mu_r)$ from data points with comparable μ_r-values

$\langle\mu_r\rangle$ [GeV]	No. of data points	$\alpha_s(\mu_r)\vert_{k_T}$	$\alpha_s(\mu_r)\vert_{\text{anti}-k_T}$	PDF and theoretical uncertainties at μ_r Individual contributions	Total
11.9	9	$0.1684\,(22)_{\text{exp}}$	$0.1697\,(21)_{\text{exp}}$	$(13)_{\text{PDF}}$ $(21)_{\text{PDFset}}$ $(11)_{\text{PDF}(\alpha_s)}$ $(21)_{\text{had}}$ $(91)_{\mu_r}$ $(13)_{\mu_f}$	$(100)_{\text{pdf,theo}}$
14.1	6	$0.1600\,(31)_{\text{exp}}$	$0.1605\,(28)_{\text{exp}}$	$(12)_{\text{PDF}}$ $(21)_{\text{PDFset}}$ $(6)_{\text{PDF}(\alpha_s)}$ $(18)_{\text{had}}$ $(72)_{\mu_r}$ $(10)_{\mu_f}$	$(79)_{\text{pdf,theo}}$
17.4	18	$0.1567\,(24)_{\text{exp}}$	$0.1546\,(23)_{\text{exp}}$	$(9)_{\text{PDF}}$ $(22)_{\text{PDFset}}$ $(2)_{\text{PDF}(\alpha_s)}$ $(13)_{\text{had}}$ $(61)_{\mu_r}$ $(9)_{\mu_f}$	$(67)_{\text{pdf,theo}}$
25.6	22	$0.1420\,(22)_{\text{exp}}$	$0.1415\,(21)_{\text{exp}}$	$(6)_{\text{PDF}}$ $(17)_{\text{PDFset}}$ $(3)_{\text{PDF}(\alpha_s)}$ $(8)_{\text{had}}$ $(43)_{\mu_r}$ $(8)_{\mu_f}$	$(47)_{\text{pdf,theo}}$
59.6	9	$0.1248\,(76)_{\text{exp}}$	$0.1267\,(68)_{\text{exp}}$	$(10)_{\text{PDF}}$ $(1)_{\text{PDFset}}$ $(1)_{\text{PDF}(\alpha_s)}$ $(5)_{\text{had}}$ $(33)_{\mu_r}$ $(9)_{\mu_f}$	$(37)_{\text{pdf,theo}}$

Table 41: Values of $\alpha_s(M_Z)$ and $\alpha_s(\mu_r)$ from five fits to groups of data points with comparable value of the renormalisation scale from normalised multijet cross sections. The cross section weighted average value of the renormalisation scale is also given. Theoretical uncertainties are quoted for the fits to the normalised k_T jet cross sections.

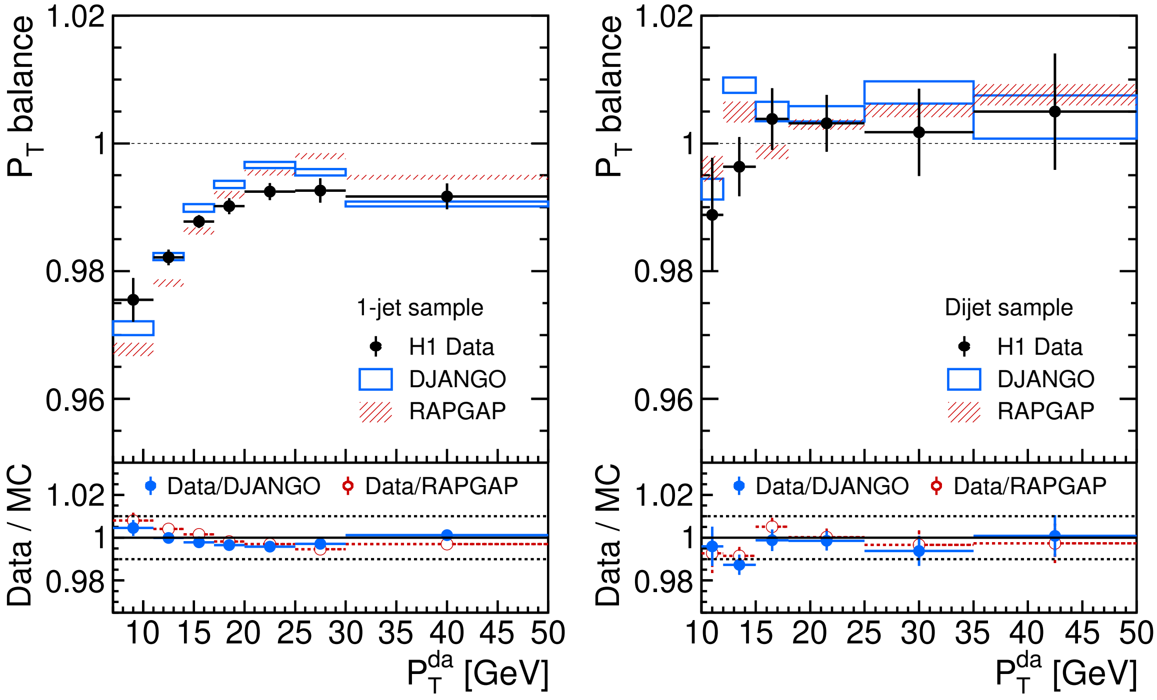

Figure 2: Mean values of the $P_{\mathrm{T,bal}}$-distributions and the double-ratio of data to MC simulations as function of $P_{\mathrm{T}}^{\mathrm{da}}$, as measured in the one-jet calibration sample and in an independent dijet sample. Results for data are compared to RAPGAP and DJANGOH. The open boxes and the shaded areas illustrate the statistical uncertainties of the MC simulations. The dashed lines in the double-ratio figure indicate a ± 1 % deviation.

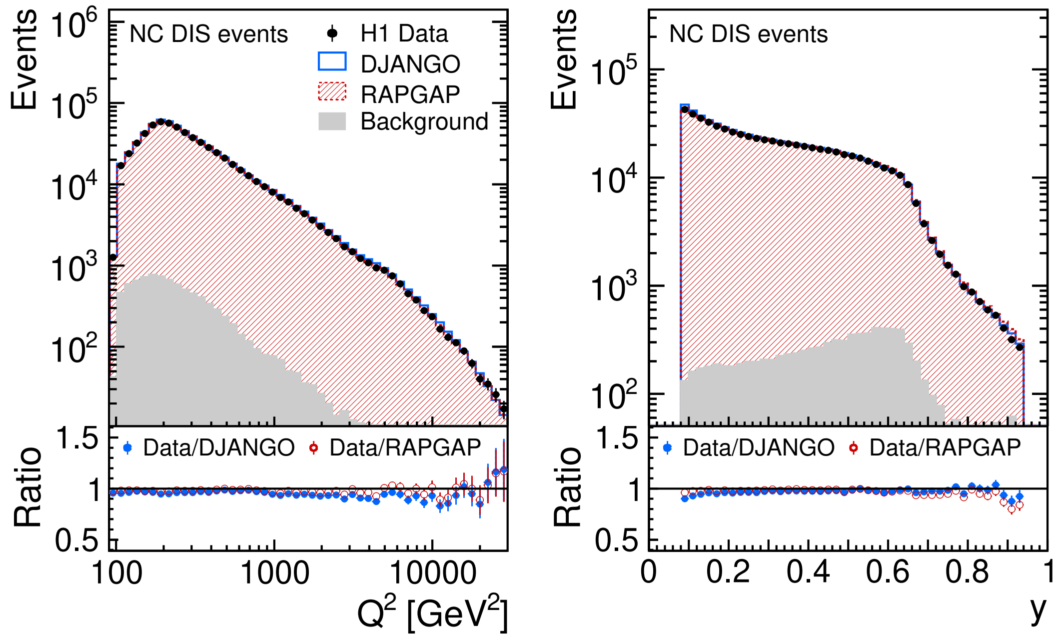

Figure 3: Distributions of Q^2 and y for the selected NC DIS data on detector level in the extended analysis phase space. The data are corrected for the estimated background contributions, shown as gray area. The predictions from DJANGOH and RAPGAP are weighted to achieve good agreement with the data. The ratio of data to prediction is shown at the bottom of each figure.

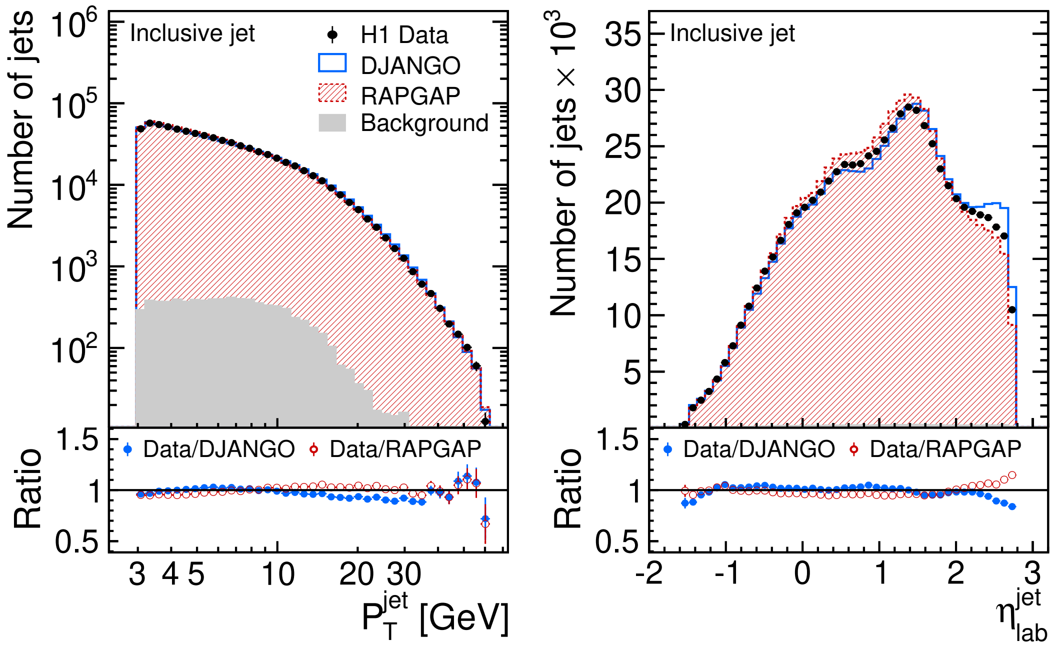

Figure 4: Distributions of $P_{\mathrm{T}}^{\mathrm{jet}}$ and $\eta_{\mathrm{lab}}^{\mathrm{jet}}$ for the selected inclusive jet data on detector level in the extended analysis phase space. The are been corrected for the estimated background contributions, shown as gray area. The predictions from DJANGOH and RAPGAP are weighted to achieve good agreement with the data. The ratio of data to prediction is shown at the bottom of each figure.

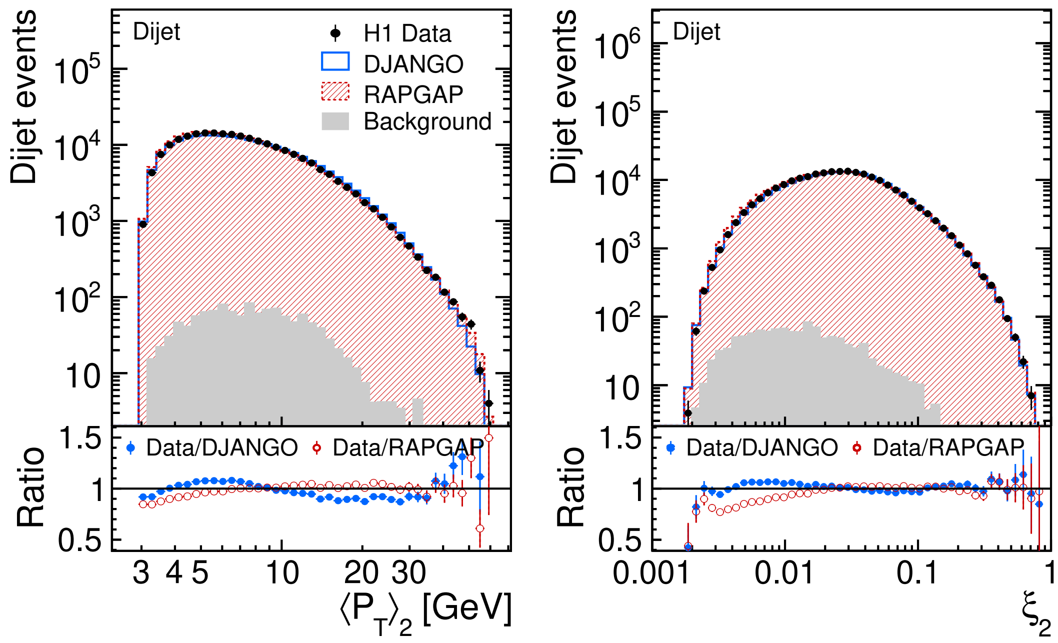

Figure 5: Distributions of $\langle P_{\mathrm{T}}\rangle_2$ and ξ_2 for the selected dijet data on detector level in the extended analysis phase space. The data are corrected for the estimated background contributions, shown as gray area. The predictions from DJANGOH and RAPGAP are weighted to achieve good agreement with the data. The ratio of data to prediction is shown at the bottom of each figure.

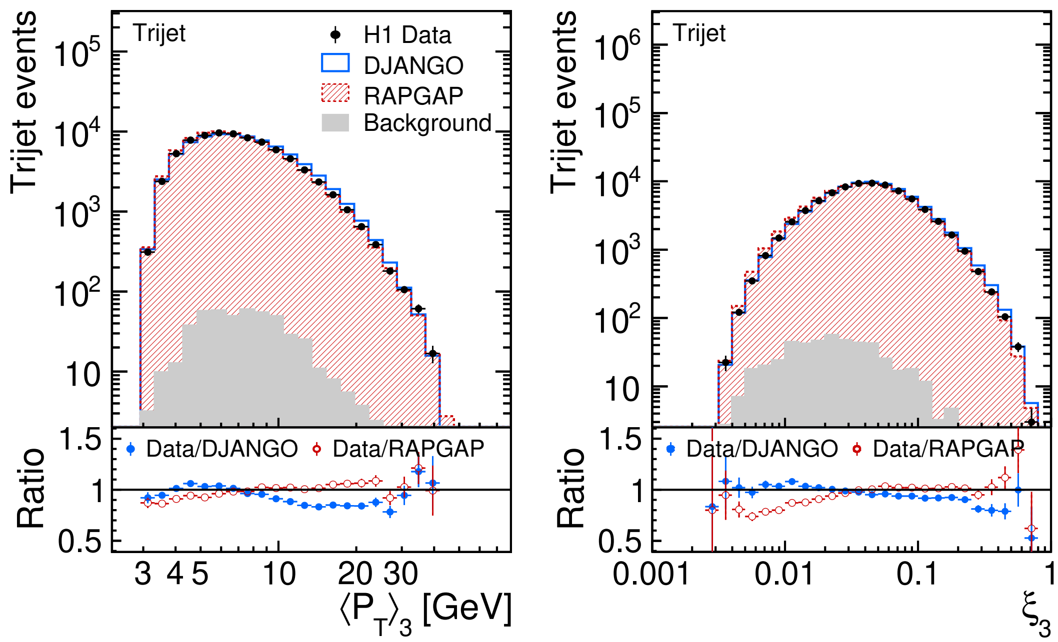

Figure 6: Distributions of $\langle P_{\mathrm{T}}\rangle_3$ and ξ_3 for the selected trijet data on detector level in the extended analysis phase space. The data are corrected for the estimated background contributions, shown as gray area. The predictions from DJANGOH and RAPGAP are weighted to achieve good agreement with the data. The ratio of data to prediction is shown at the bottom of each figure.

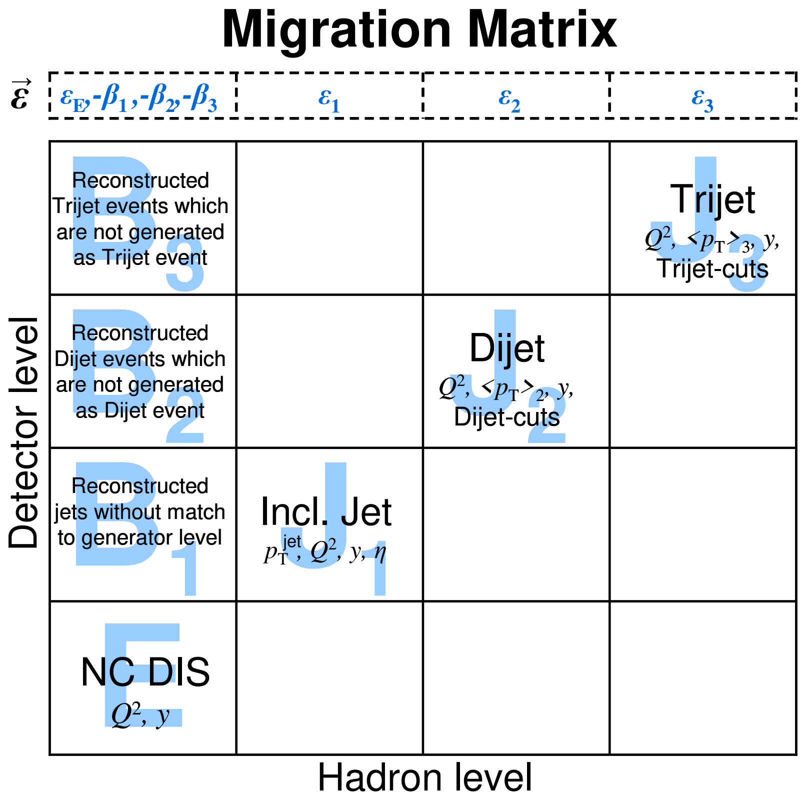

Figure 7: Schematic illustration of the migration matrix for the regularised unfolding, which includes the NC DIS (E), the inclusive jet (J_1), the dijet (J_2) and the trijet (J_3) MC events. The observables utilised for the description of migrations are given in the boxes referring to the respective submatrices. The submatrices which connect the hadron level NC DIS data with the detector level jet data ((B_1),(B_2), and (B_3)) help to control detector-level-only entries. An additional vector, $\vec{\varepsilon}$, is used for efficiency corrections and to preserve the normalisation.

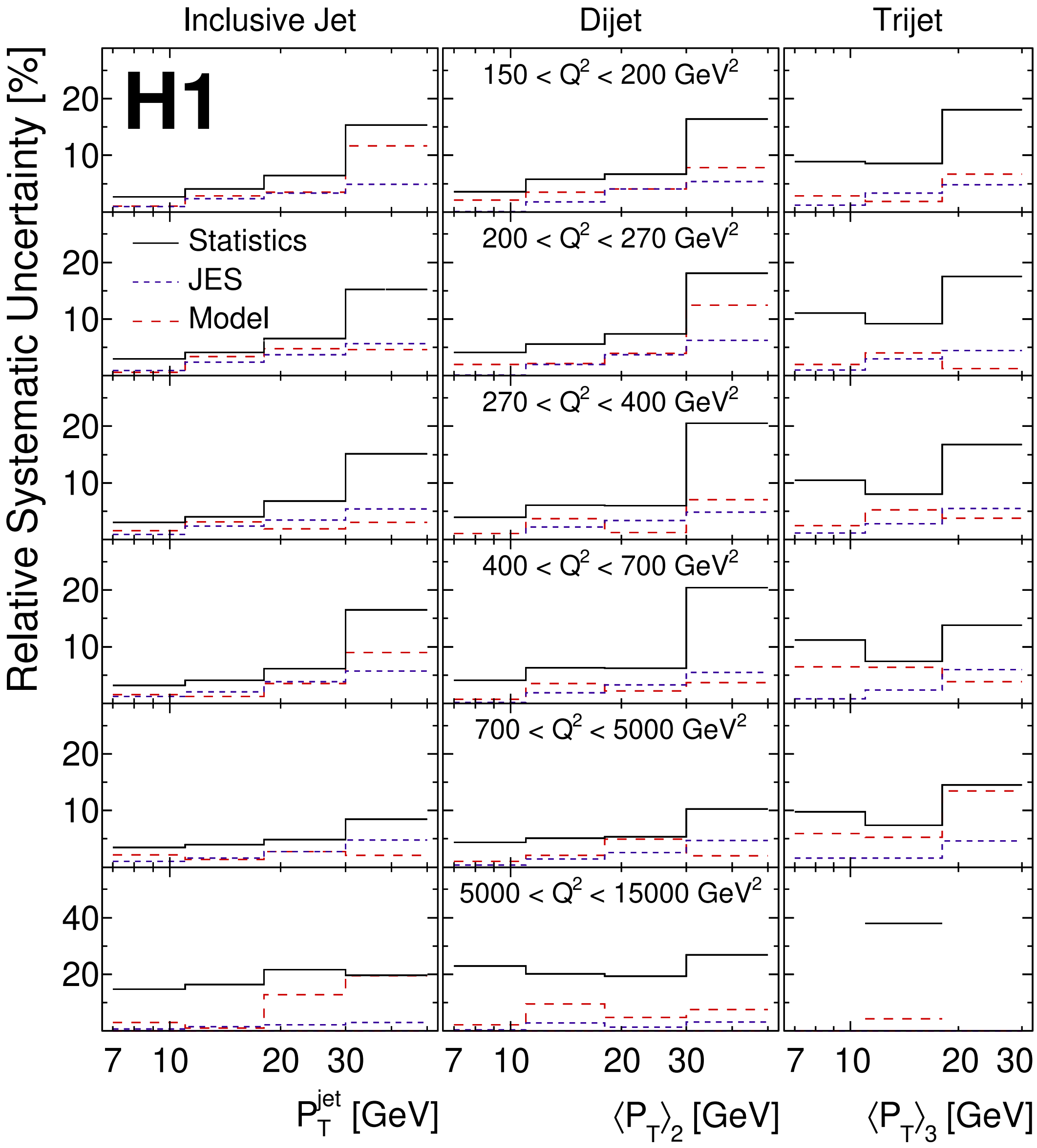

Figure 8: Illustration of the most prominent experimental uncertainties of the cross section measurement. Shown are the statistical uncertainties, the jet energy scale δ^{JES} and the model uncertainty. Adjacent bins typically have negative correlation coefficients for the statistical uncertainty. The uncertainties shown are of comparable size for the corresponding normalised jet cross sections.

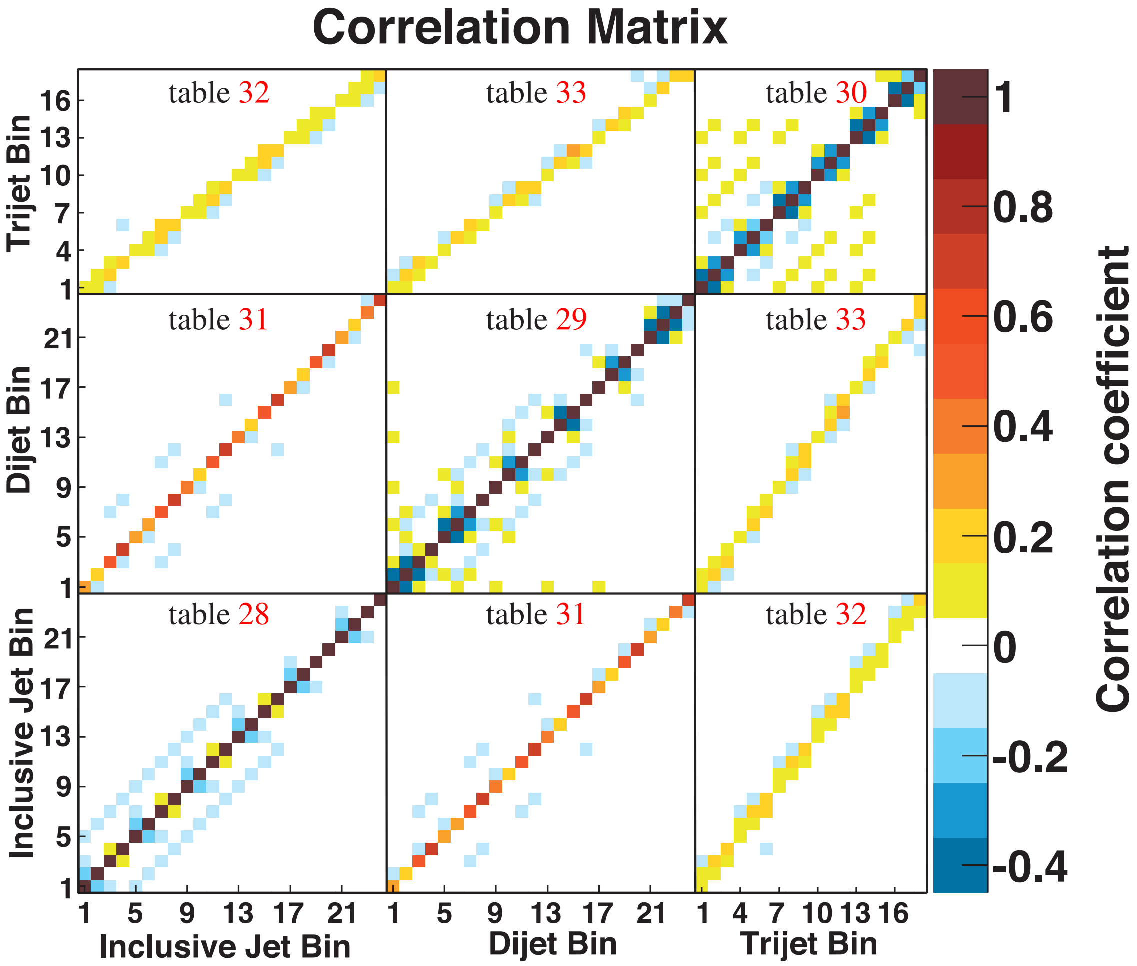

Figure 9: Correlation matrix of the three jet cross section measurements. The bin numbering is given by $b = (q-1)n_{P_{\mathrm{T}}} + p$, where q stands for the bins in Q^2 and p for the bins in P_{T} (see table table 7). For the inclusive jet and dijet measurements $n_{P_{\mathrm{T}}} = 4$, and for the trijet measurement $n_{P_{\mathrm{T}}} = 3$. The numerical values of the correlation coefficients are given in the tables indicated.

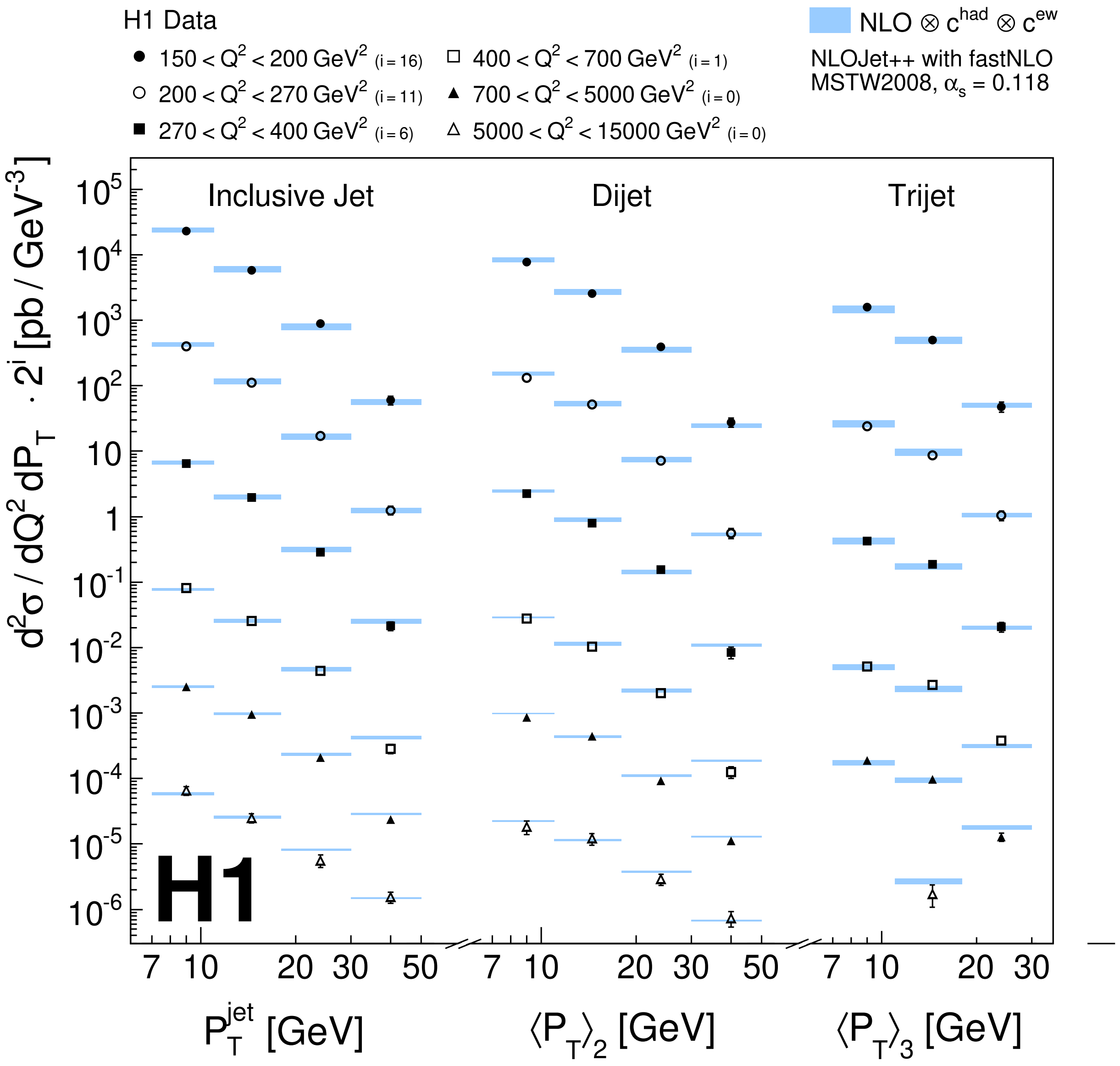

Figure 10: Double-differential cross sections for jet production in DIS as a function of Q^2 and P_{T}. The inner and outer error bars indicate the statistical uncertainties and the statistical and systematic uncertainties added in quadrature. The NLO QCD predictions, corrected for hadronisation and electroweak effects, together with their uncertainties are shown by the shaded band. The cross sections for individual Q^2 bins are multiplied by a factor of 10^i for better readability.

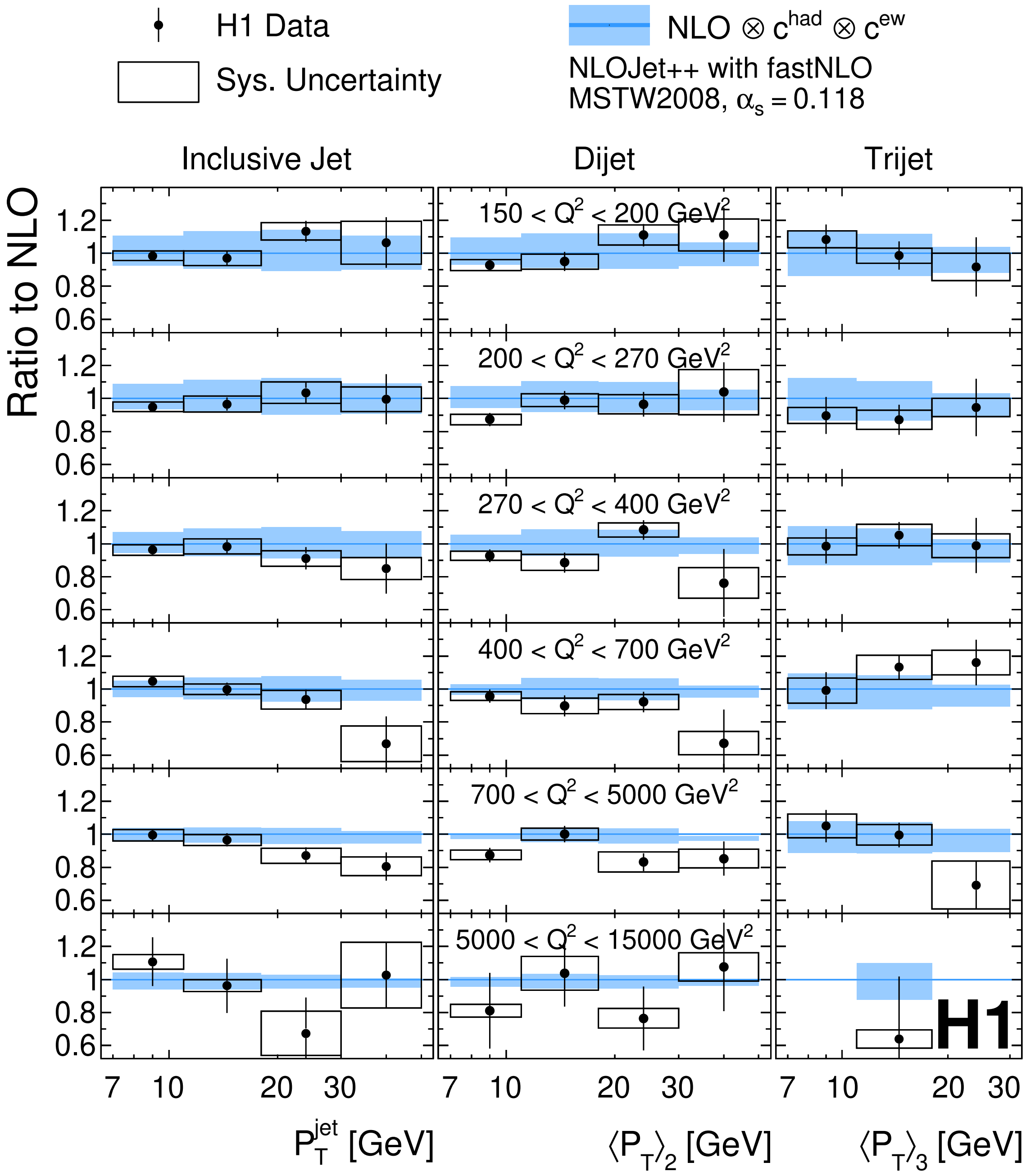

Figure 11: Ratio of jet cross sections to NLO predictions as function of Q^2 and P_{T}. The error bars on the data indicate the statistical uncertainties of the measurements, while the total systematic uncertainties are given by the open boxes. The shaded bands show the theory uncertainty.

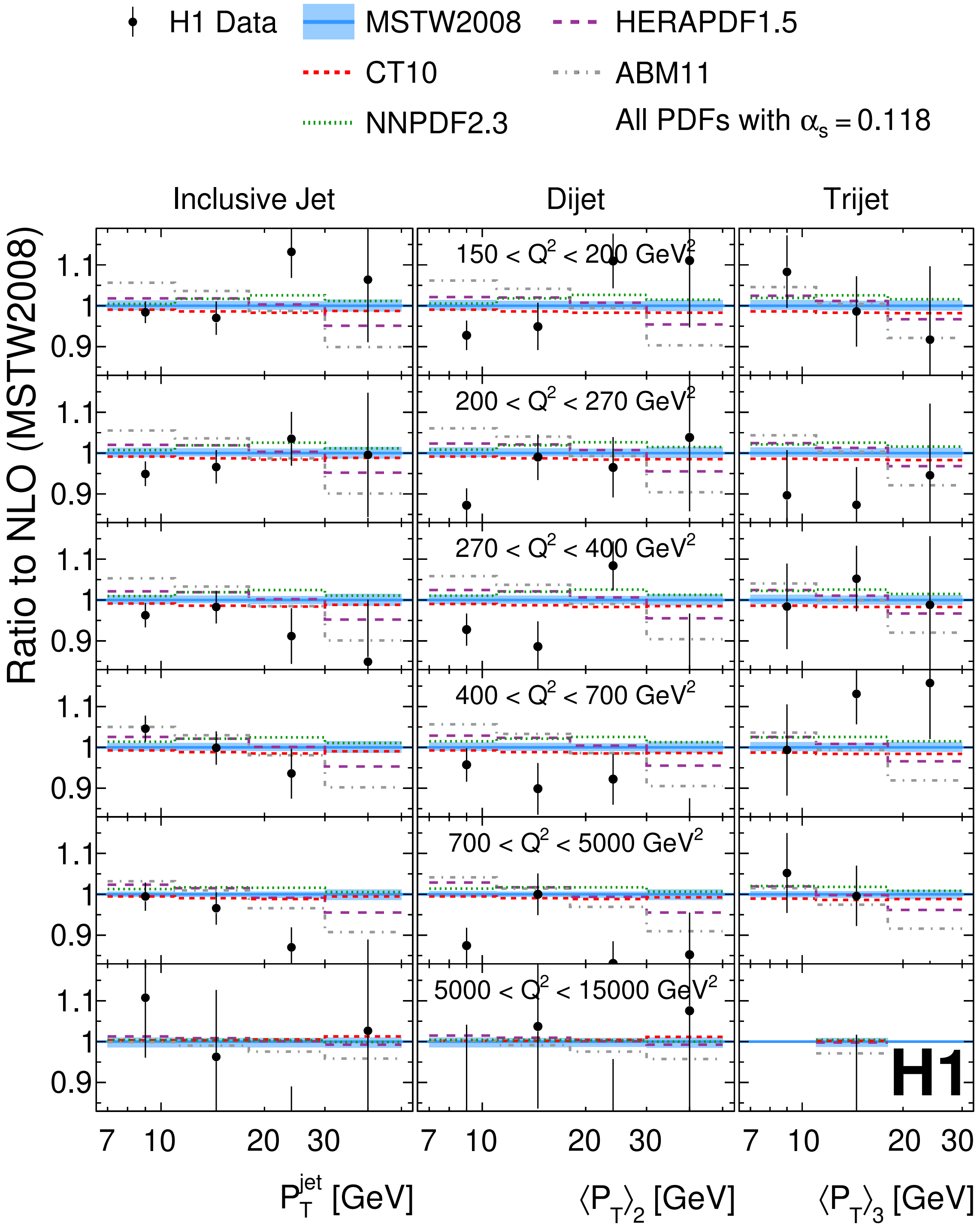

Figure 12: Ratio of NLO predictions with various PDF sets to predictions using the MSTW2008 PDF set as a function of Q^2 and $P_{\rm T}$. For comparison, the data points are displayed together with their statistical uncertainty, which are often outside of the displayed range in this enlarged presentation. All PDF sets used are determined at NLO and with a value of $\alpha_s(M_Z) = 0.118$. The shaded bands show the PDF uncertainties of the NLO calculations obtained from the MSTW2008 eigenvector set at a confidence level of 68 %.

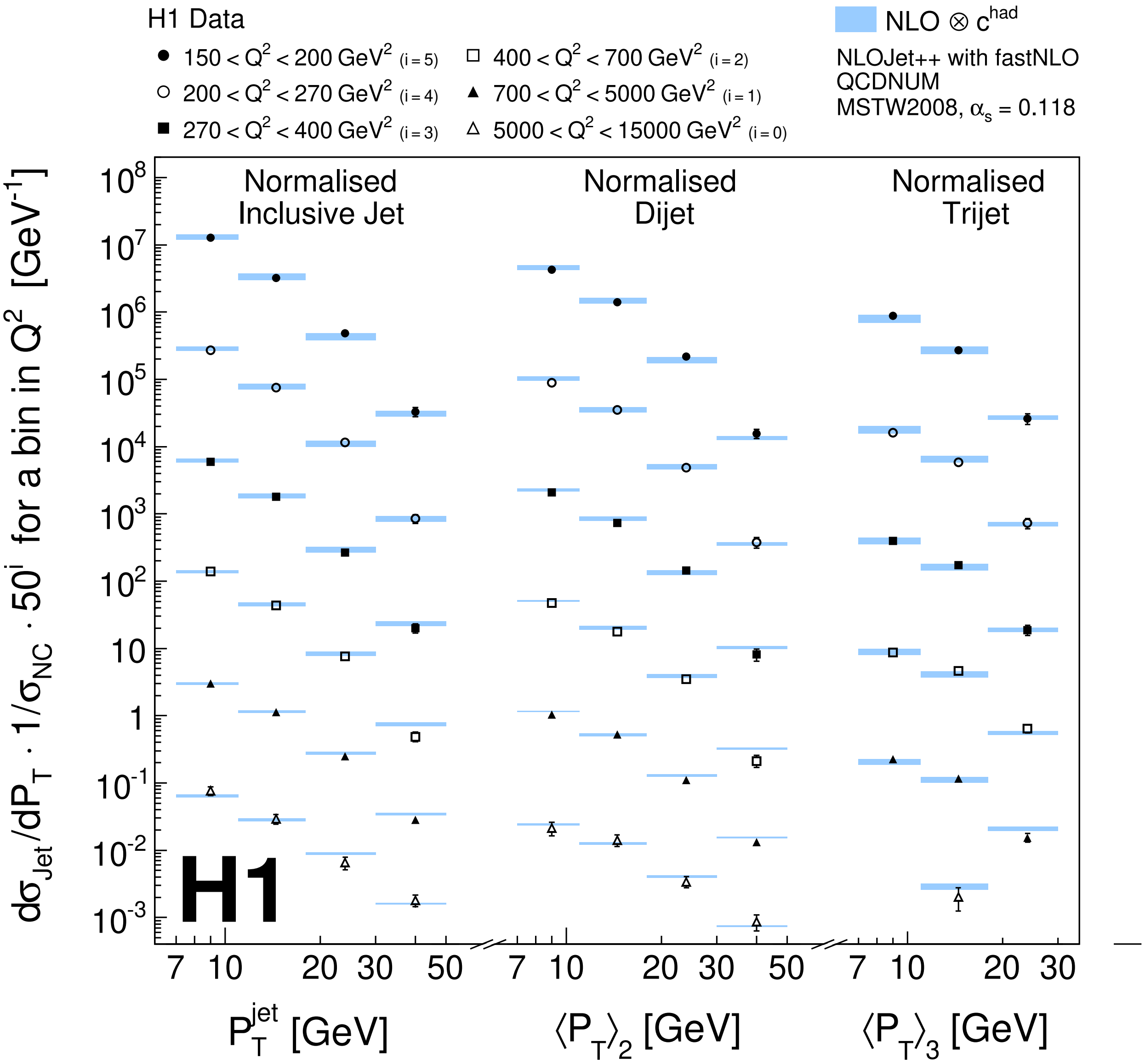

Figure 13: Double-differential normalised cross sections for jet production in DIS as a function of Q^2 and $P_{\rm T}$. The NLO predictions, corrected for hadronisation effects, together with their uncertainties are shown by the shaded bands. Further details can be found in the caption of figure 10.

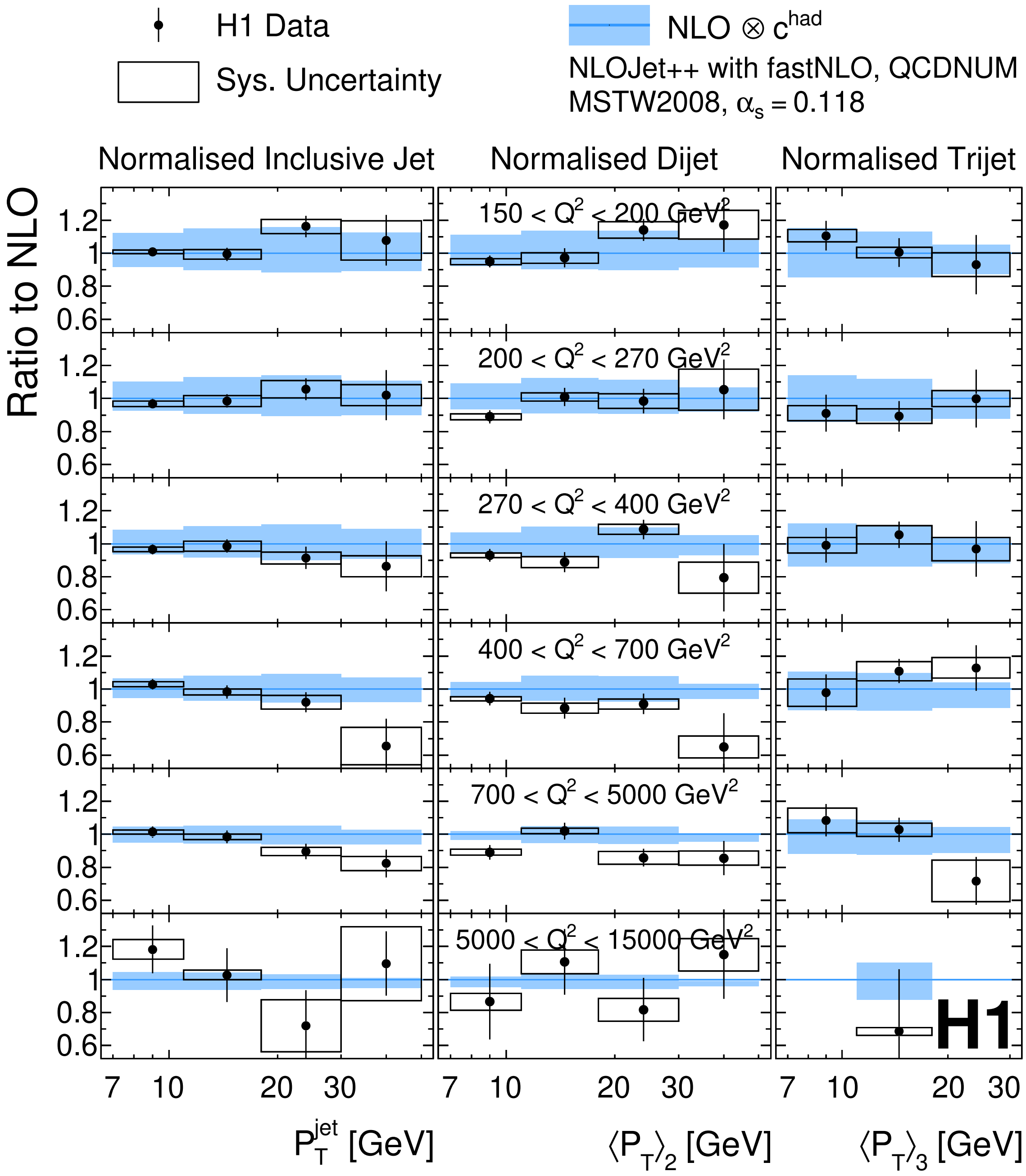

Figure 14: Ratio of normalised jet cross sections to NLO predictions as a function of Q^2 and P_{T}. The error bars on the data indicate the statistical uncertainties of the measurements, while the total systematic uncertainties are given by the open boxes. The shaded bands show the theory uncertainty.

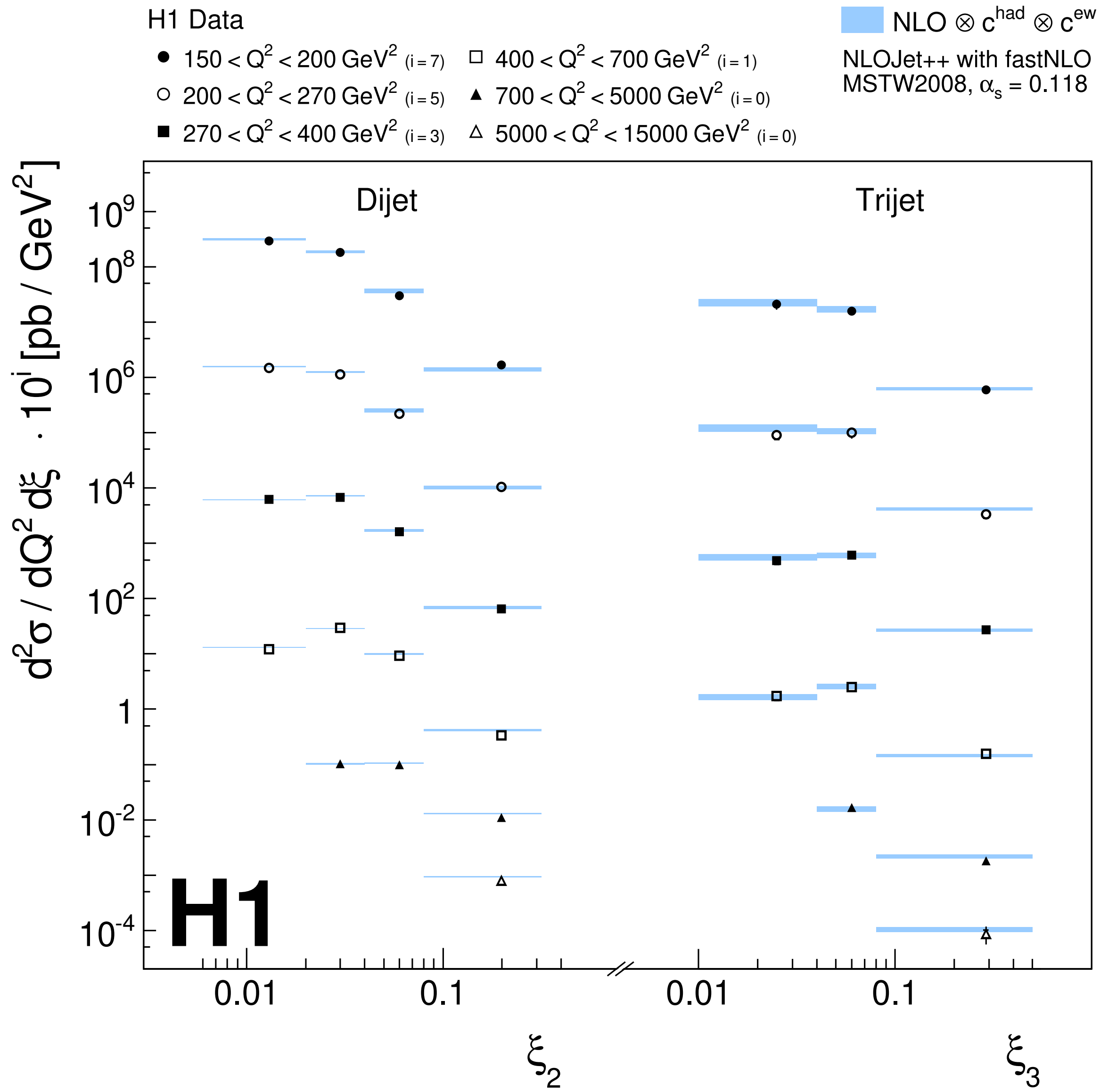

Figure 15: Double-differential cross sections for dijet and trijet production in DIS as a function of Q^2 and ξ. The NLO predictions, corrected for hadronisation and electroweak effects, together with their uncertainties are shown by the shaded bands. Further details can be found in the caption of figure 10.

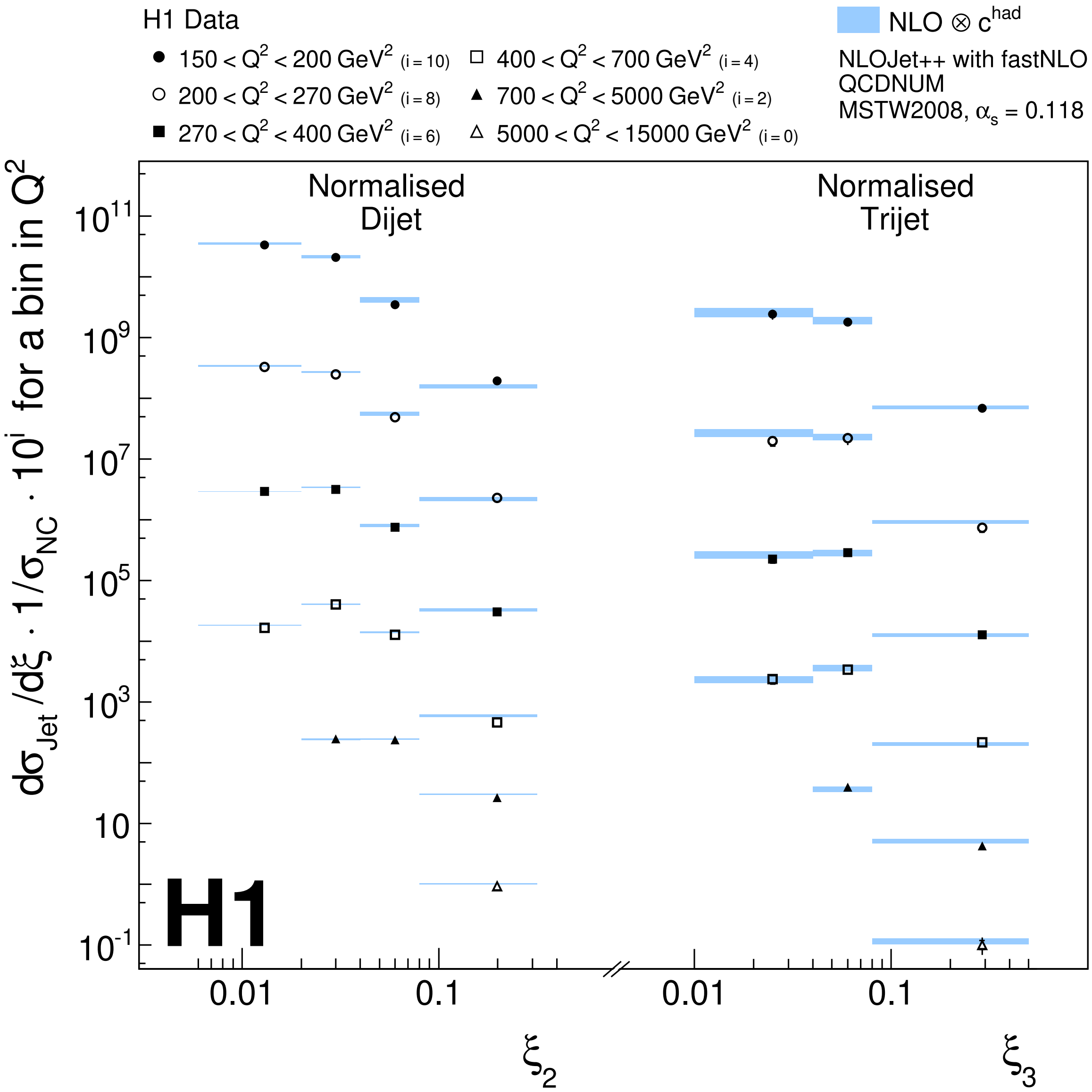

Figure 16: Double-differential normalised cross sections for dijet and trijet production in DIS as a function of Q^2 and ξ. The NLO predictions, corrected for hadronisation effects, together with their uncertainties are shown by the shaded bands. Further details can be found in the caption of figure 10.

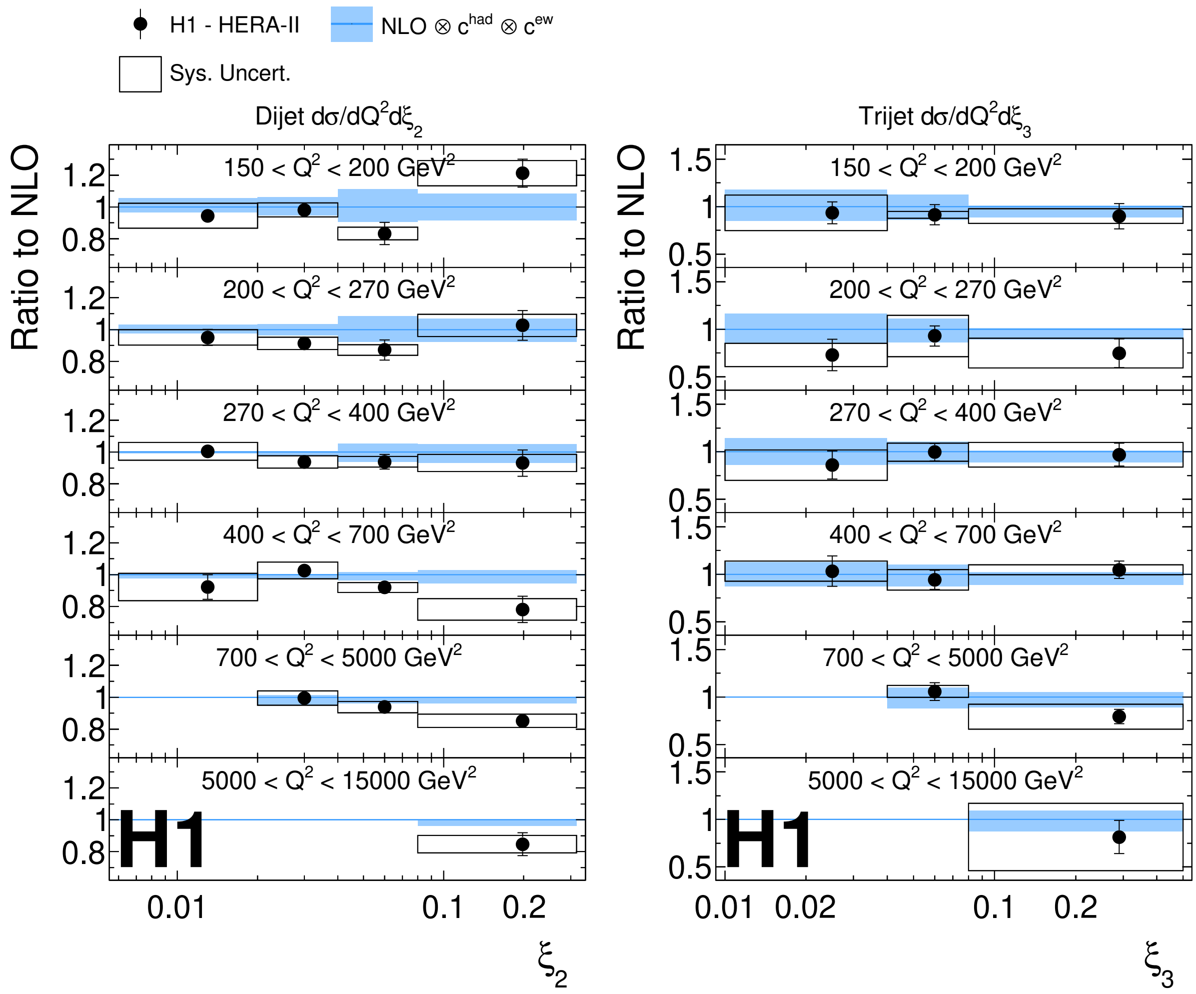

Figure 17: Ratio of the dijet and trijet cross sections to NLO QCD predictions as a function of Q^2 and ξ. The error bars on the data indicate the statistical uncertainties of the measurements while the total experimental systematic uncertainties are given by the open boxes. The shaded bands show the theory uncertainties.

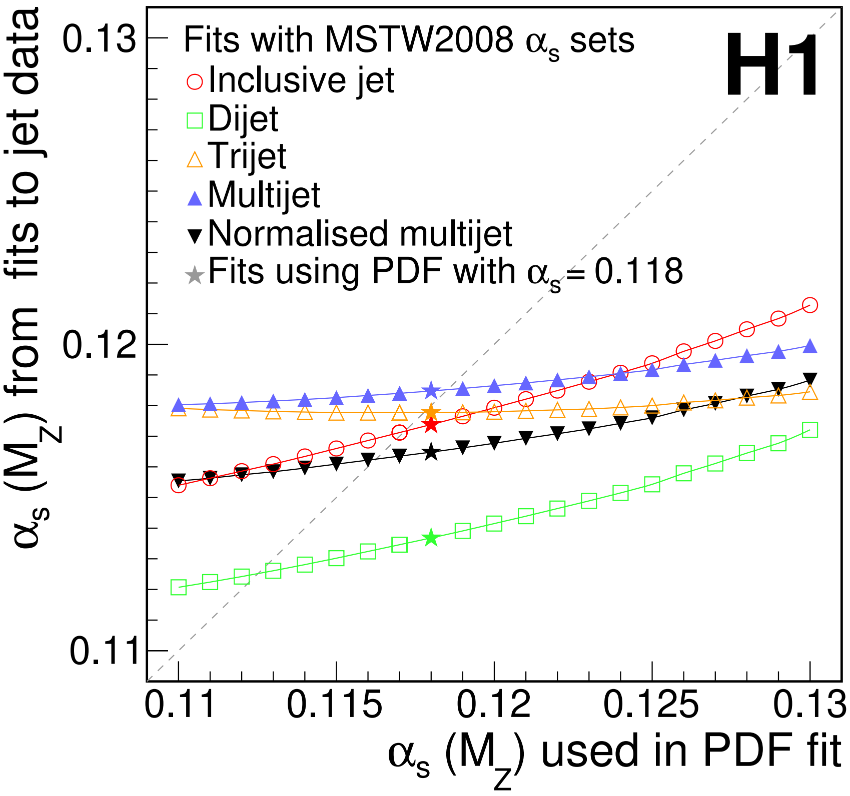

Figure 18: Values of $\alpha_s(M_Z)$ extracted from fits of the NLO QCD predictions to the jet cross section measurements. Shown are the values of $\alpha_s(M_Z)$ obtained with the inclusive jet, dijet and trijet data separately, and for fits either to the multijet or to the normalized multijet measurements. Each point stands for a value of $\alpha_s(M_Z)$ obtained using a PDF set which has been determined assuming a fixed values of $\alpha_s(M_Z)$ as indicated.

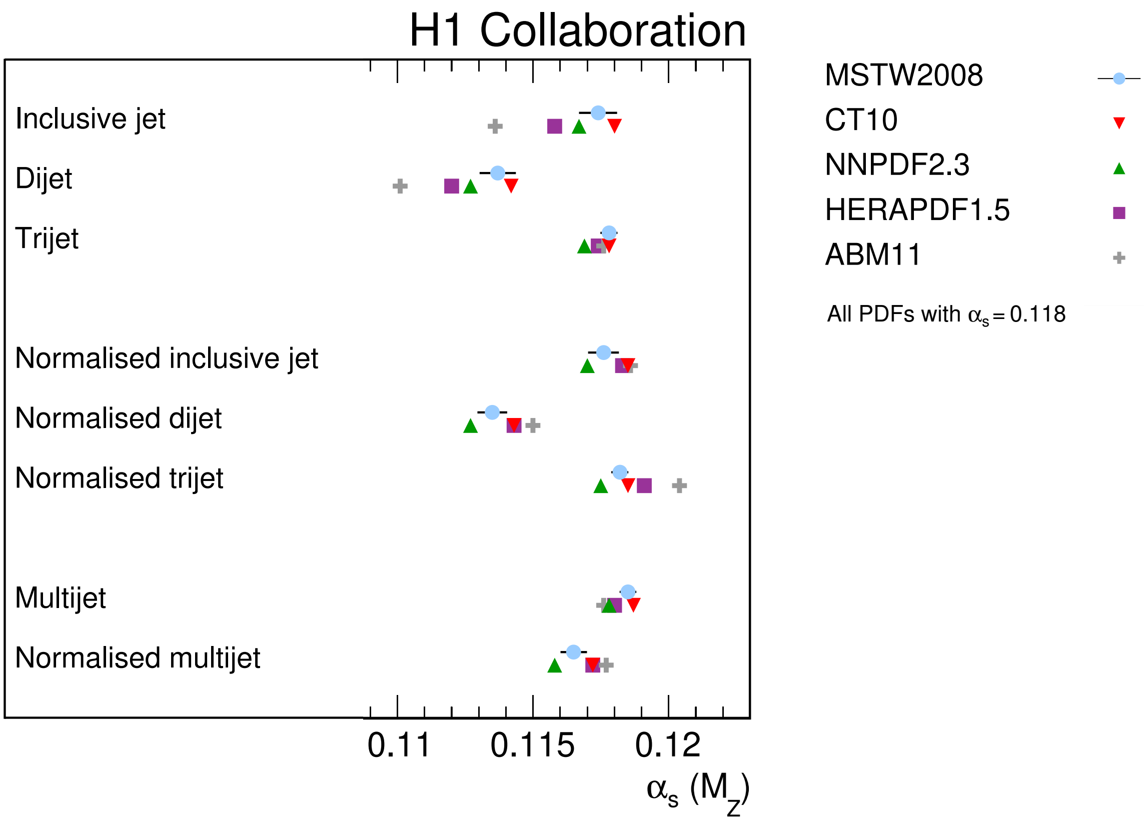

Figure 19: Values of $\alpha_s(M_Z)$ extracted from fits of NLO QCD predictions to the absolute and normalised jet cross sections using different PDF sets: MSTW2008, CT10, NNPDF2.3, HERAPDF1.5 and ABM11. For the MSTW2008 PDF set the PDF uncertainty on $\alpha_s(M_Z)$ as determined from the MSTW2008 eigenvectors is shown as horizontal error bar.

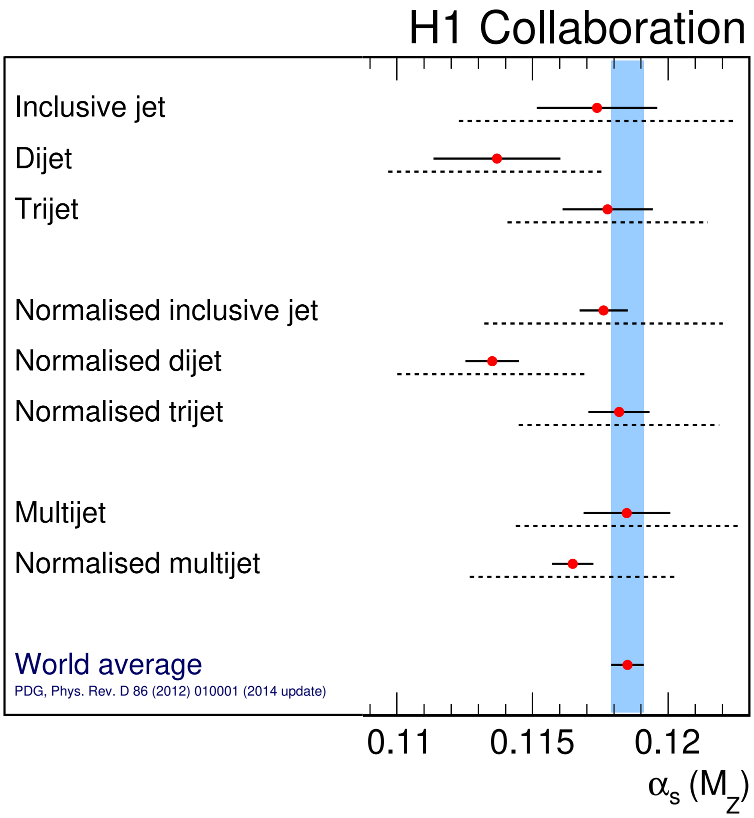

Figure 20: Comparison of α_s-values extracted from different jet cross section measurements, separately and simultaneously, to the world average value of $\alpha_s(M_Z)$. The full line indicates the experimental uncertainty and the dashed line the theoretical uncertainty. The band indicates the uncertainty of the world average value of $\alpha_s(M_Z)$.

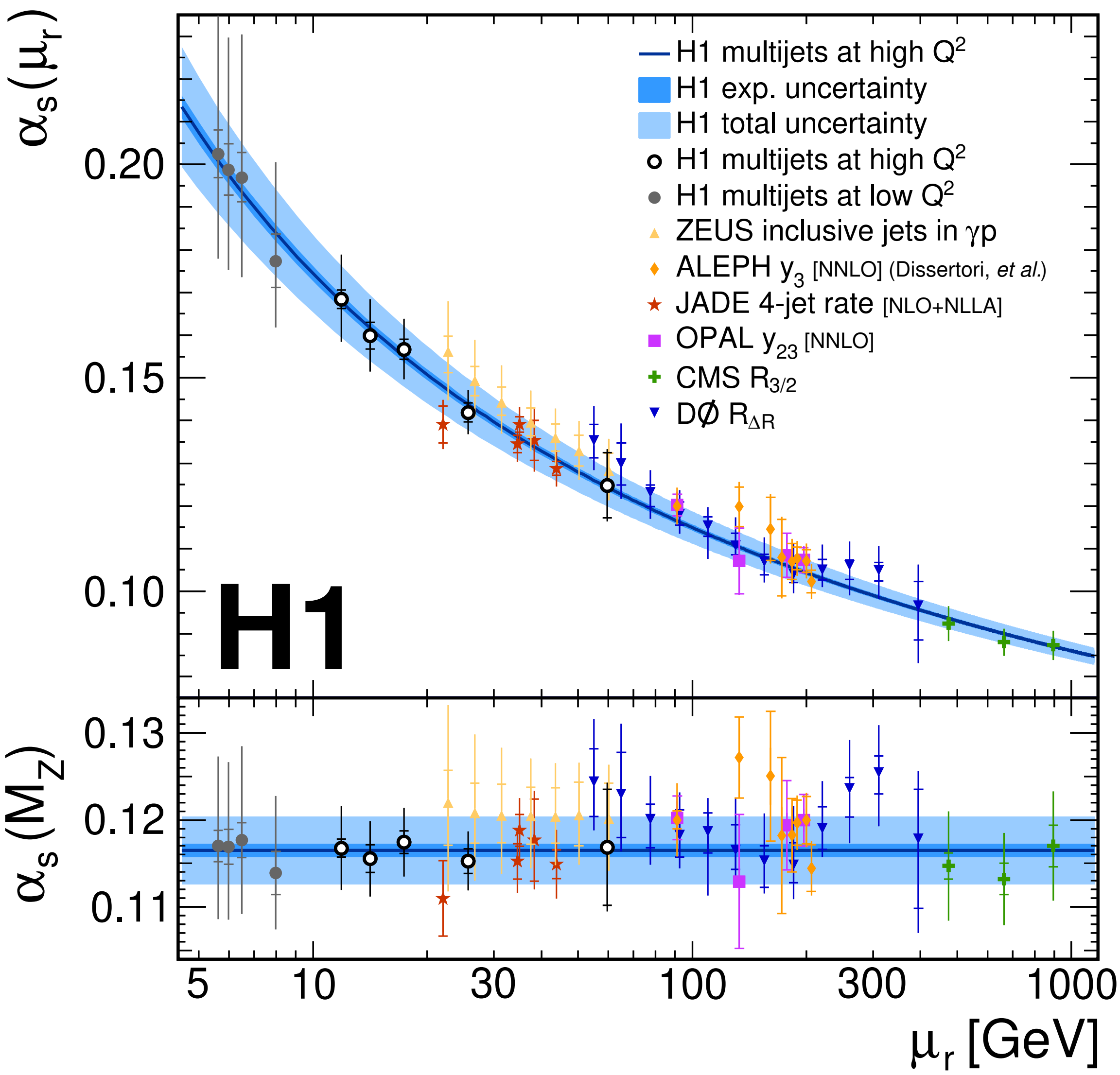

Figure 21: The upper panel shows the values of the strong coupling $\alpha_s(\mu_r)$ as determined from the normalized multijet measurement (open dots) at different scales μ_r. The inner error bars indicate the experimental uncertainty, while the full error bars indicate the total uncertainty, including the experimental and theoretical contributions. The solid line shows the NLO QCD prediction calculated using the renormalisation group equation with $\alpha_s(M_Z) = 0.1165$ as determined from the simultaneous fit to all normalized multijet measurements. The dark shaded band around this line indicates the experimental uncertainty on $\alpha_s(\mu_r)$, while the light shaded band shows the total uncertainty. Also shown are the values of α_s from multijet measurement at low values of Q^2 by H1 (circles), from inclusive jet measurements in photoproduction by the ZEUS experiment (upper triangles), from the 3-jet rate y_3 in a fit of NNLO calculations to ALEPH data taken at LEP (diamonds), from the 4-jet rate measured by the JADE experiment at PETRA (stars), from the jet transition value y_{23} measured by OPAL at LEP (squares), from the ratio of trijet to dijet cross sections $R_{3/2}$ as measured by the CMS experiment at the LHC (crosses), and from jet angular correlations $R_{\Delta R}$ by the D0 experiment at the Tevatron (lower triangles). In the lower panel the equivalent values of $\alpha_s(M_Z)$ for all measurements are shown.